AERODYNAMIC CHARACTERISTICS OF A FIVE BLADED S-SHAPED SAVONIUS ROTOR

MD. NAYEM ASHRAF

DEPARTMENT OF MECHANICAL ENGINEERING

BANGLADESH UNIVERSITY OF ENGINEERING AND TECHNOLOGY

DHAKA-1000, BANGLADESH

March 2016

`

AERODYNAMIC CHARACTERISTICS OF A FIVE BLADED S-SHAPED SAVONIUS ROTOR

The thesis is submitted to the Department of Mechanical Engineering, Bangladesh University of Engineering and Technology (BUET), Dhaka, Bangladesh in partial fulfillment of the requirement for the degree of Master of Science in Mechanical Engineering.

THESIS PREPARED BY

Md. Nayem Ashraf Student No: 0411102047F

SUPERVISED BY

Professor Dr. Md. Quamrul Islam,
Department of Mechanical Engineering,
Bangladesh University of Engineering and Technology (BUET)
Dhaka-1000, Bangladesh

Department of Mechanical Engineering
Bangladesh University of Engineering & Technology
Dhaka-1000, Bangladesh

March 2016

RECOMMENDATION OF THE BOARD OF EXAMINERS

The board of examiners hereby recommends to the Department of Mechanical Engineering, Bangladesh University of Engineering and Technology (BUET), Dhaka the acceptance of the thesis, "**AERODYNAMIC CHARACTERISTICS OF A FIVE BLADED S-SHAPED SAVONIUS ROTOR",** Submitted by Md. Nayem Ashraf, Roll No: 0411102047F Session: April 2011 has been accepted as satisfactory in partial fulfillment of the requirement for the degree of Master of Science in Mechanical Engineering on March 30, 2016.

1. ………………………………..
   Dr. Md. Quamrul Islam — **Chairman**
   Professor
   Department of ME, BUET, Dhaka.
   (Supervisor)

2. …………………………………….
   Head — **Member (Ex-Officio)**
   Department of ME, BUET, Dhaka.

3. …………………………………….
   Dr. Mohammad Ali — **Member**
   Professor
   Department of ME, BUET, Dhaka.

4. …………………………………..
   Dr. Mohammad Mamun — **Member**
   Professor
   Department of ME, BUET, Dhaka.

5. …………………………………..
   Dr. Most. Hosney Ara Begum — **Member (External)**
   Principal Scientific Officer
   BCSIR, Dhanmondi, Dhaka-1205

CERTIFICATE OF RESEARCH

This is to certify that the work presented in this thesis is an outcome of the investigation Carried out by the author under the supervision of Dr. Md. Quamrul Islam, Professor, Department of Mechanical Engineering, Bangladesh University of Engineering and Technology (BUET), Dhaka.

Prepared by

…………………………………

Md. Nayem Ashraf
Student No: 0411102047F

Supervised by

………………………………

Dr. Md. Quamrul Islam,
Professor
Department of Mechanical Engineering
Bangladesh University of Engineering &Technology (BUET)
Dhaka - 1000, Bangladesh.

`

ACKNOWELEDGEMENT

I wish to express my sincere gratitude and indebtedness to Dr. Md. Quamrul Islam for his guidance and supervision throughout the entire period of the experimental investigation. His initiatives, encouragement, patience and invaluable suggestions are gratefully acknowledged without which this work would not have been possible.

Sincere thanks are offered to Mr. Alauddin, Mr Abul Kalam technician of Fluid Mechanics laboratory of Mechanical Engineering department for his co-operation at different stages of the work.

Lastly, I would like to thank my parents for their inspiration to complete this work in proper time. Without their encouragement it would have been really difficult for me to complete this work.

`

ABSTRACT

The S-shaped rotor is a modification of the Savonius rotor with no overlap. Drag and torque coefficients of a five bladed S-shaped Savonius rotor have been investigated by measuring the pressure distribution on the blade surfaces for various rotor angles. The experiments have been carried out at a Reynolds number of 2.1×10^5 in a uniform flow jet produced by an open circuit wind tunnel.

To calculate drag force and torque in non-dimensional form, the data are taken on 12 pressure tapping points on each blade of the five bladed S-shaped Savonius rotor for every 10^0 interval of the angle of rotation. The pressure distributions both on the concave and convex surface of the blade at different angle of rotation are presented graphically. At rotor angle $\alpha = 40^0$, difference of pressure coefficient on convex surface and concave surface is maximum. At rotor angle $\alpha = 310^0$, difference of pressure coefficient on convex surface and concave surface is minimum.

The measurements indicate that drag forces and the torque, vary with rotor angle. The normal drag coefficient increases with the rotor angle, reaches its maximum value at the rotor angle $\alpha = 40^0$, remains approximately constant value at the rotor angle $\alpha = 140^0$ to 210^0 and minimum value at the rotor angle $\alpha = 310^0$. The tangential drag coefficient increases with the rotor angle, reaches its maximum value at the rotor angle $\alpha = 290^0$ and minimum value at the rotor angle $\alpha = 0^0$. The torque coefficient also increases with the rotor angle, reaches its maximum value at the rotor angle $\alpha = 40^0$, remains approximately constant value at the rotor angle $\alpha = 140^0$ to 210^0 and reaches minimum value at the rotor angle $\alpha = 310^0$. The result facilitates predicting the performance of five bladed S-shaped Savonius rotor under dynamic conditions.

`

LIST OF CONTENTS

`

CHAPTER-2

REVIEW OF LITERATURE

CHAPTER-3

EXPERMENTAL SET UP AND PROCEDURE

CHAPTER-4

DERIVATION TECHNIQUE OF NON-DIMECSIONAL PARAMETRES

`

CHAPTER-5

RESULTS AND DISCUSSIONS

CHAPTER-6

CONCLUSIONS AND RECOMMENDATIONS

`

LIST OF FIGURES

Figures **Page**

`

`

`

LIST OF SYMBOLS

C_p Pressure coefficient

C_{pe} Pressure coefficient for concave surface of the blade

C_{px} Pressure coefficient for convex surface of the blade

C_t Drag coefficient in the transverse direction of the chord

C_n Drag coefficient in the normal direction of the chord

Cq Torque coefficient

ri Distance between rotor center and normal of any segment

D Diameter of the rotor

F_n Normal forces acting on a blade

F_t Tangential forces acting on a blade

H Height of the rotor

p Pressure on blade

P_0 Atmospheric pressure

R_e Reynolds number

T Torque on a blade

U_0 Free stream velocity

ΔPi Pressure difference

ΔSi Chord length of any segment

Greek Symbols

A Rotor angle

ϕ_i Angle of pressure tappings

ω Angular speed of the rotor

ν Kinematic viscosity of air

ΔP Difference of pressure between concave and convex surfaces of a blade

CHAPTER-1

INTRODUCTION

CHAPTER 1

INTRODUCTION

1.1 General

Energy has become synonymous with today's civilization. With advancement of modern science rapid development is seen in all aspect of life, so the demand of energy is increasing in geometrical rate. The most conventional energy source like oil, hydro, coal, natural gas etc. are used as fuels all around the world. Among these conventional fuels, only hydro is renewable in nature and others sources are non renewable and causes of air pollution and green house effect. In the consequence, environmental pollution has reached in an alarming level all over the world. As the sources of conventional energy is not only being exhausted very rapidly but also causing serious threats to the existence of mankind, people are rethinking about the use of environment friendly as well as renewable energy resources in large scale. Replacing the conventional fuels with renewable energy sources include wind energy, solar (photovoltaic) systems, solar thermal systems, biomass energy (wood and other plant fuels), geothermal energy, fuel cell, municipal waste etc. The costs of many of these technologies have come down considerably in recent years, particularly wind energy, which is now competitive with conventional power sources in regions with strong winds.

The science of exploitation of wind power is not a new one. For the past few centuries people are extracting energy from the wind in various ways. One means for converting wind energy to a more useful form is through the use of windmills. Recently, due to the fuel crisis, this science is gaining more popularity. Wind energy has become very lucrative now-a-days due to its reliability. Recent regulatory and economic developments in the EU have significantly changed the wind energy perspective for the next 15 years. In light of uncertain governance towards achieving EU climate and energy binding targets, The European Wind Energy Association (EWEA) updated the European wind energy industry's vision to 2030. EWEA's new Central Scenario expects 320 GW of wind energy capacity to be installed in the EU in 2030, 254 GW of onshore wind and 66 GW of offshore wind. That would be more than twice as much as the installed capacity in 2014 (129 GW) and an increase of two thirds from the expected capacity installed in 2020 (192 GW). Wind energy will produce 778 TWh of electricity, equal to 24.4% of the EU's electricity demand. The wind energy industry will provide over 334,000 direct and indirect jobs in the EU and wind energy installations in 2030 will be worth €474 bn. The 96,000 wind turbines installed on land and in the sea will avoid the emission of 436 million of tonnes (Mt) of CO2.

The U.S. Department of Energy (DOE) has released Wind Vision: A New Era for Wind Power in the United States. The new report shows wind energy can supply the U.S. with 10 percent of the country's electricity by 2020, 20 percent by 2030 and 35 percent by 2050 and provides a road map for how to get there. Wind Vision updates and expands on the DOE's 2008 report, 20% Wind Energy by 2030: Increasing wind energy's contribution to the U.S. electricity supply**,** which galvanized the rapid growth of wind so that it now generates 4.5 percent of America's electricity.

There are various types of windmills. The most common one having the blades of airfoil shape is the horizontal axis turbine. Another type is the vertical axis wind turbine. The primary attraction of the vertical-axis wind turbine is the simplicity of its manufacture compared to horizontal axis wind turbine. Among the different vertical axis wind turbines, the Savonius rotor is a slow running wind machine and has a relatively lower efficiency. Still it is being used in the developing countries because of its simple design, easy and cheap technology for construction and a good starting torque independent of wind direction at low wind speeds [l, 2 & 3]. Rigorous studies on the performance characteristics of the Savonius rotor are found in the literatures and these enable the identification of an optimum geometrical configuration for practical design [4, 5, 6, 7 & 8].

1.2 Wind as a Source of Energy

People are extracting energy mainly from the fossil fuels in almost all the countries of the world for a long time. In some of the countries they are also utilizing uranium fuel which is a source of nuclear energy. With the rising demand of energy and for many other reasons, prices of these fuels are increasing day by day. So people are trying to find the alternate sources of energy to exploit them at the cheapest rate. Wind energy is a kind of energy source which will never be finished. It is available almost all the times, in all the places and in large quantities all over the world. Again fossil and uranium fuels will be finished once. These are not available in all the countries. Besides these, people are interested to be self-dependent; they do not like to rely on imported fuel which requires huge amount of foreign currency. On the other hand, to date no effective method has been developed to apply the solar energy. As a result in different parts of the world, people are taking keen interest to develop efficient and economic devices to collect energy from the wind. Recently, the utilization of wind power is increasing highly in many developed as well as developing countries.

1.3 History of Wind Energy

Wind power has been used as long as humans have put sails into the wind. For more than two millennia wind-powered machines have ground grain and pumped water. Wind power was widely available and not confined to the banks of fast-flowing streams, or later, requiring sources of fuel. Wind-powered pumps drained the polders of the Netherlands, and in arid regions such as the American mid-west or the Australian outback, wind pumps provided water for live stock and steam engines.

The first windmill used for the production of electricity was built in Scotland in July 1887 by Prof James Blyth of Anderson's College, Glasgow (the precursor of Strathclyde University) [9]. Blyth's 10 m high, cloth-sailed wind turbine was installed in the garden of his holiday cottage at Marykirk in Kincardineshire and was used to charge accumulators developed by the Frenchman Camille Alphonse Faure, to power the lighting in the cottage, thus making it the first house in the world to have its electricity supplied by wind power [10]. Blyth offered the surplus electricity to the people of Marykirk for lighting the main street, however, they turned down the offer as they thought electricity was the work of the devil. Although he later built a wind turbine to supply emergency power to the local Lunatic Asylum, Infirmary and Dispensary of Montrose the invention never really caught on as the technology was not considered to be economically viable [9].

Across the Atlantic, in Cleveland, Ohio a larger and heavily engineered machine was designed and constructed in the winter of 1887–1888 by Charles F. Brush [10] this was built by his engineering company at his home and operated from 1886 until 1900 [11]. The Brush wind turbine had a rotor 17 m (56 foot) in diameter and was mounted on an 18 m (60 foot) tower. Although large by today's standards, the machine was only rated at 12 kW. The connected dynamo was used either to charge a bank of batteries or to operate up to 100 incandescent light bulbs, three arc lamps, and various motors in Brush's laboratory [12].

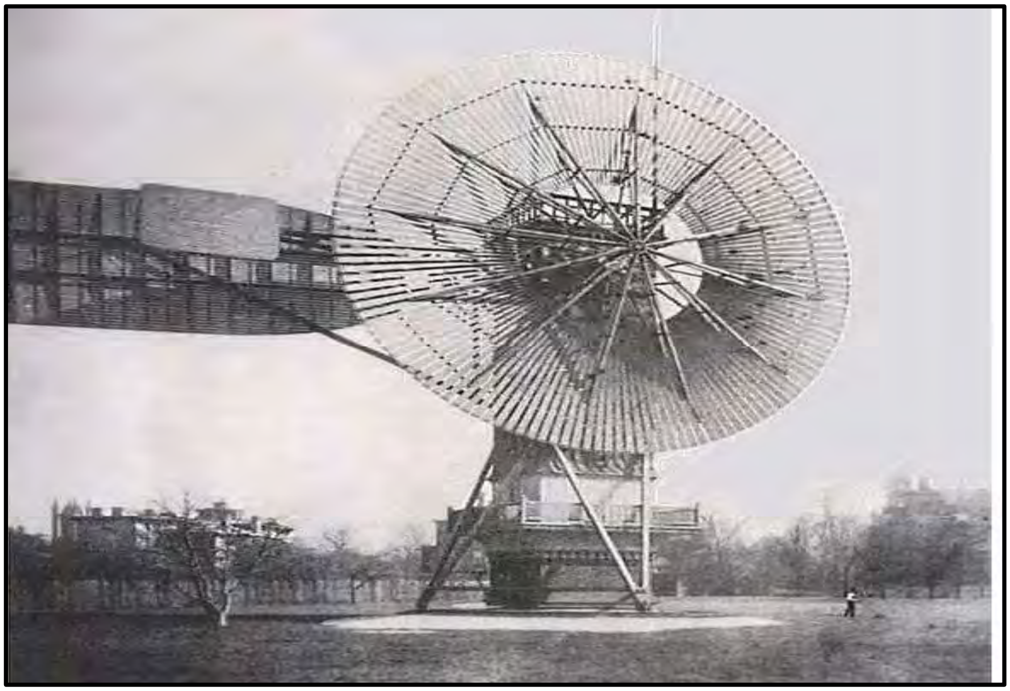

Figure 1.1: Charles Brush's windmill of 1888, used for generating electricity [10]

With the development of electric power, wind power found new applications in lighting buildings remote from centrally-generated power. Throughout the 20th century parallel paths developed small wind stations suitable for farms or residences, and larger utility-scale wind generators that could be connected to electricity grids for remote use of power. Today wind powered generators operate in every size range between tiny stations for battery charging at isolated residences, up to near-gigawatt sized offshore wind farms that provide electricity to national electrical networks.

1.4 Wind Energy Around The World

Wind power is extracted from air flow using wind turbines or sails to produce mechanical or electrical power. Windmills are used for their mechanical power, wind pumps for water pumping, and sails to propel ships. Wind power as an alternative to fossil fuels, is plentiful, renewable, widely distributed, clean, produces no greenhouse gas emissions during operation, and uses little land. The net effects on the environment are far less problematic than those of nonrenewable power sources.

Wind farms consist of many individual wind turbines which are connected to the electric power transmission network. Onshore wind is an inexpensive source of electricity, competitive with or in many places cheaper than coal or gas plants. Offshore wind is steadier and stronger than on land, and offshore farms have less visual impact, but construction and maintenance costs are considerably higher. Small onshore wind farms can feed some energy into the grid or provide electricity to isolated off-grid locations [13].

Wind power is very consistent from year to year but has significant variation over shorter time scales. It is therefore used in conjunction with other electric power sources to give a reliable supply. As the proportion of wind power in a region increases, a need to upgrade the grid and a lowered ability to supplant conventional production can occur. Power management techniques such as having excess capacity, geographically distributed turbines, dispatchable backing sources, sufficient hydroelectric power, exporting and importing power to neighboring areas, using vehicle-to-grid strategies or reducing demand when wind production is low, can in many cases overcome these problems. In addition, weather forecasting permits the electricity network to be readied for the predictable variations in production that occur.

As of 2014, Denmark has been generating around 40% of its electricity from wind [14 & 15], and at least 83 other countries around the world are using wind power to supply their electricity grids [16]. Wind power capacity has expanded to 369,553 MW by December 2014 [17] and total wind energy production is growing rapidly and has reached around 4% of worldwide electricity usage [18].

1.5 Onshore Wind Farms in World

A wind farm is a group of wind turbines in the same location used for production of electricity. A large wind farm may consist of several hundred individual wind turbines distributed over an extended area, but the land between the turbines may be used for agricultural or other purposes. For example, Gansu Wind Farm, the largest wind farm in the world, has several thousand turbines. A wind farm may also be located offshore.

Almost all large wind turbines have the same design a horizontal axis wind turbine having an upwind rotor with three blades, attached to a nacelle on top of a tall tubular tower.

In a wind farm, individual turbines are interconnected with a medium voltage (often 34.5 kV), power collection system and communications network. At a substation, this medium voltage electric current is increased in voltage with a transformer or connection to the high voltage electric power transmission system.

Largest Onshore wind Farms [19, 20, 21, 22, 23, 24, 25, 26, 27 & 28]		
Wind Farm	**Current Capacity (MW)**	**Country**
Gansu Wind Farm	6,000	China
Alta (Oak Creek-Mojave)	1,320	United States
Jaislmer Wind Park	1064	India
Sheperds Flat Wind Foarm	845	United States
Roscoe Wind Farm	782	United States
Horse Hollow Wind Energy Center	736	United States
Capricorn Ridge Wind Farm	662	United States
Fantanele-Cogealac Wind farm	600	Romania
Fowler Ridge Wind Farm	600	United States
Whitelee Wind Farm	539	United Kingdom

1.6 Offshore Wind Farms in World

Offshore wind power refers to the construction of wind farms in large bodies of water to generate electricity. These installations can utilize the more frequent and powerful winds that are available in these locations and have less aesthetic impact on the landscape than land based projects. However, the construction and the maintenance costs are considerably higher [29 & 30].

Siemens and Vestas are the leading turbine suppliers for offshore wind power. The Danish Oil and Natural Gas (DONG) Energy, Vattenfall and E.ON are the leading offshore operators. As of October 2010, 3.16 GW of offshore wind power capacity was operational, mainly in Northern Europe. According to BTM Consult, more than 16 GW of additional capacity will be installed before the end of 2014 and the UK and Germany will become the two leading markets. Offshore wind power capacity is expected to reach a total of 75 GW worldwide by 2020, with significant contributions from China.

Largest Offshore Wind Farms in World [31]				
Wind farm	**Capacity (MW)**	**Country**	**Turbilnes and Model**	**Commissioned**
London Array	630	United Kingdom	175 x Simens SWT-3.6 107	2012
Gwynt Mor	576	United Kingdom	160 x Simens SWT 3.6	2015
Greater Gabbard	504	United Kingdom	140 x Simens SWT-3.6	2012
Anholt	400	Denmark	111 x Simens SWT-3.6-120	2013
BARD Offshore 1	400	Germany	80 BARD 5.0 Turbines	2013

At the end of 2012, 1,662 turbines at 55 offshore wind farms in 10 European countries are generating 18 TWh, which can power almost five million households. As of August 2013 the

London Array in the United Kingdom is the largest offshore wind farm in the world at 630 MW. This is followed by Gwynt y Môr (576 MW), also in the UK.

1.7 Wind power capacity and production

Worldwide there are now over two hundred thousand wind turbines operating, with a total nameplate capacity of 282,482 MW as of end 2012 [27]. The European Union alone passed some 100,000 MW nameplate capacity in September 2012 [28]. While the United States surpassed 50,000 MW in August 2012 and China's grid connected capacity passed 50,000 MW the same month [29 & 30].

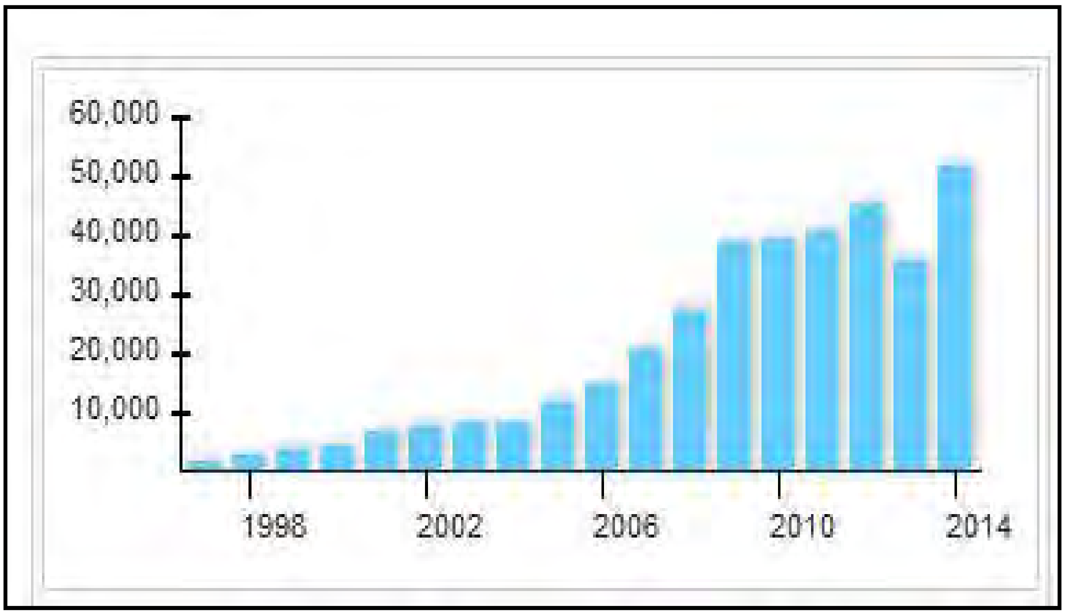

Figure 1.2: Global annual new installed wind capacity 1997-2014 (in MW) [32]

World wind generation capacity more than quadrupled between 2000 and 2006, doubling about every three years. The United States pioneered wind farms and led the world in installed capacity in the 1980s and into the 1990s. In 1997 installed capacity in Germany surpassed the U.S. and led until once again overtaken by the U.S. in 2008. China has been rapidly expanding its wind installations in the late 2000s and passed the U.S. in 2010 to become the world leader. As of 2011, 83 countries around the world were using wind power on a commercial basis [16].

Top Wind power Electricity Producing Countries in 2012 (TWh)		
Country	**Wind Power Production**	**% of World Total**
United States	140.9	26.4
China	118.1	22.1
Spain	49.1	9.2
Germany	46.0	8.6
India	30.0	5.6
United Kingdom	19.6	3.7
France	14.9	2.8
Italy	13.4	2.5
Canada	11.8	2.2
Denmark	10.3	1.9
Rest of World	80.2	15.0
World Total	534.3 TWh	100%

Source: Observer-Electricity production from wind sources [32]

Wind power capacity has expanded rapidly to 336 GW in June 2014, and wind energy production was around 4% of total worldwide electricity usage, and growing rapidly [18]. The actual amount of electricity that wind is able to generate is calculated by multiplying the nameplate capacity by the capacity factor, which varies according to equipment and location. Estimates of the capacity factors for wind installations are in the range of 35% to 44% [33].

Europe accounted for 48% of the world total wind power generation capacity in 2009. In 2010, Spain became Europe's leading producer of wind energy, achieving 42,976 GWh. Germany held the top spot in Europe in terms of installed capacity, with a total of 27,215 MW as of 31 December 2010 [34].

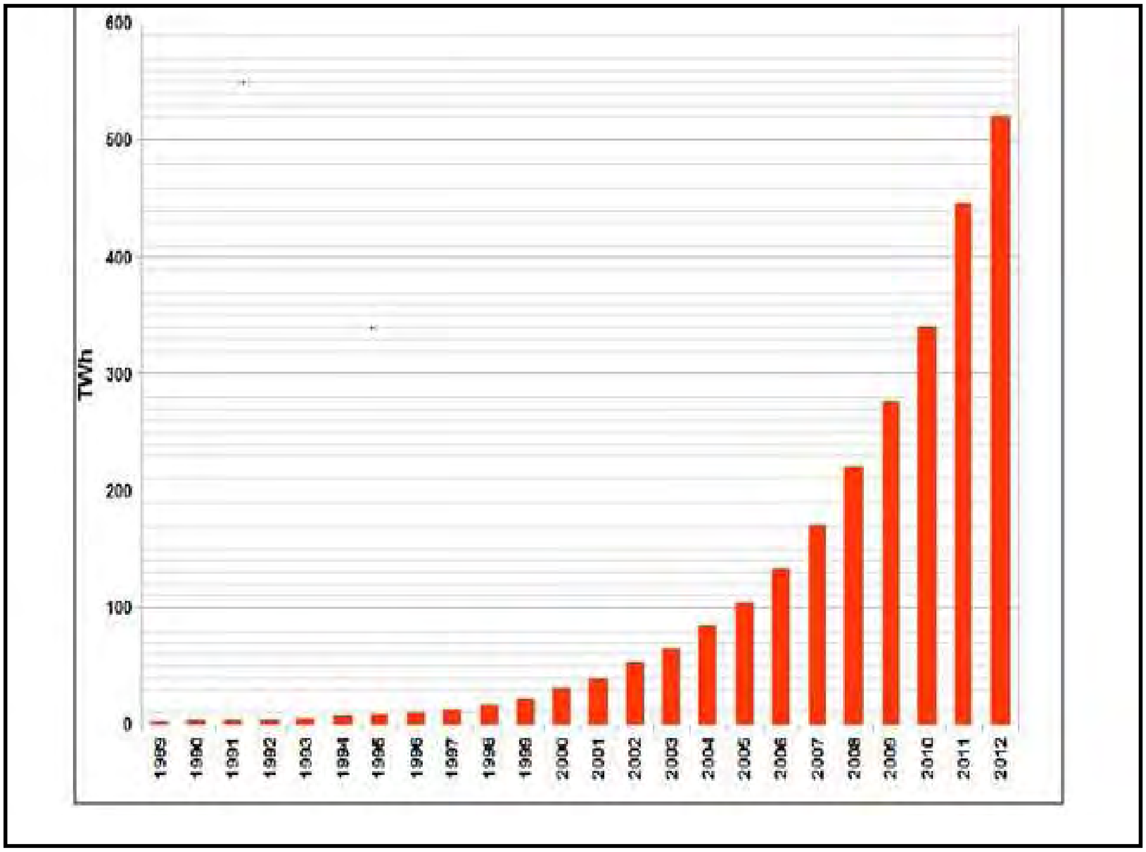

Figure 1.3: Worldwide electricity generation up to 2012 from wind sources [35]

1.8 Growth power of Wind Power

In 2010, more than half of all new wind power was added outside of the traditional markets in Europe and North America. This was largely from new construction in China, which accounted for nearly half the new wind installations (16.5 GW) [36].

Global Wind Energy Council (GWEC) figures show that 2007 recorded an increase of installed capacity of 20 GW, taking the total installed wind energy capacity to 94 GW, up from 74 GW in 2006. Despite constraints facing supply chains for wind turbines, the annual market for wind continued to increase at an estimated rate of 37%, following 32% growth in 2006. In terms of economic value, the wind energy sector has become one of the important players in the energy markets, with the total value of new generating equipment installed in 2007 reaching €25 billion, or US$36 billion [37].

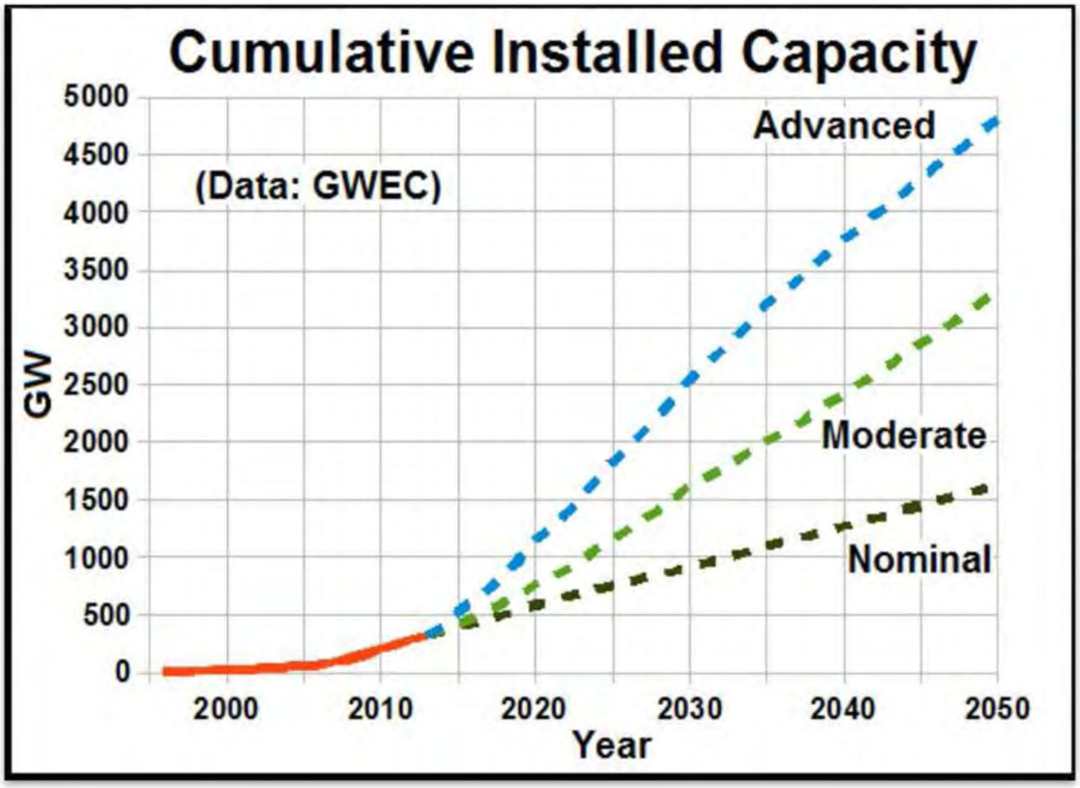

Figure 1.4: Commutative installed capacity up to 2050 of wind power [37]

Although the wind power industry was affected by the global financial crisis in 2009 and 2010, a BTM Consult five-year forecast up to 2013 projects substantial growth. Over the past five years the average growth in new installations has been 27.6% each year. In the forecast to 2013, the expected average annual growth rate is 15.7% [33 & 38]. More than 200 GW of new wind power capacity could come on line before the end of 2014. Wind power market penetration is expected to reach 3.35% by 2013 and 8% by 2018 [39 & 40].

In 2013 wind power constituted 13% of installed power generation capacity in the EU and generated 7.8% of power used.

1.9 Penetration of Wind Power

Wind energy penetration refers to the fraction of energy produced by wind compared with the total generation. There is no generally accepted maximum level of wind penetration. The limit for a particular grid will depend on the existing generating plants, pricing mechanisms, capacity for energy storage, demand management and other factors. An interconnected electricity grid will already include reserve generating and transmission capacity to allow for equipment failures. This reserve capacity can also serve to compensate for the varying power generation produced by wind stations. Studies have indicated that 20% of the total annual electrical energy consumption may be incorporated with minimal difficulty [41]. These studies have been for locations with geographically dispersed wind farms, some degree of dispatchable energy or hydropower with storage capacity, demand management, and interconnected to a large grid area enabling the export of electricity when needed. Beyond the 20% level, there are few technical limits, but the economic implications become more significant. Electrical utilities continue to study the effects of large scale penetration of wind generation on system stability and economics [42, 43, 44 & 45].

A wind energy penetration figure can be specified for different durations of time, but is often quoted annually. To obtain 100% from wind annually requires substantial long term storage or substantial interconnection to other systems which may already have substantial storage. On a monthly, weekly, daily or hourly basis or less wind might supply as much as or more than 100% of current use, with the rest stored or exported. Seasonal industry might then take advantage of high wind and low usage times such as at night when wind output can exceed normal demand. Such industry might include production of silicon, aluminum, steel or of natural gas, and hydrogen, and using future long term storage to facilitate 100% energy from variable renewable energy [46 & 47]. Homes can also be programmed to accept extra electricity on demand, for example by remotely turning up water heater thermostats [48].

In Australia, the state of South Australia generates around half of the nation's wind power capacity. By the end of 2011 wind power in South Australia, championed by Premier (and Climate Change Minister) Mike Rann, reached 26% of the State's electricity generation, edging out coal for the first time. At this stage South Australia, with only 7.2% of Australia's population, had 54% of Australia's installed capacity [49].

1.10 Costs of Wind Energy in World

Wind turbines reached grid parity (the point at which the cost of wind power matches traditional sources) in some areas of Europe in the mid-2000s, and in the US around the same time. Falling prices continue to drive the levelized cost down and it has been suggested that it has reached general grid parity in Europe in 2010, and will reach the same point in the US around 2016 due to an expected reduction in capital costs of about 12% [50].

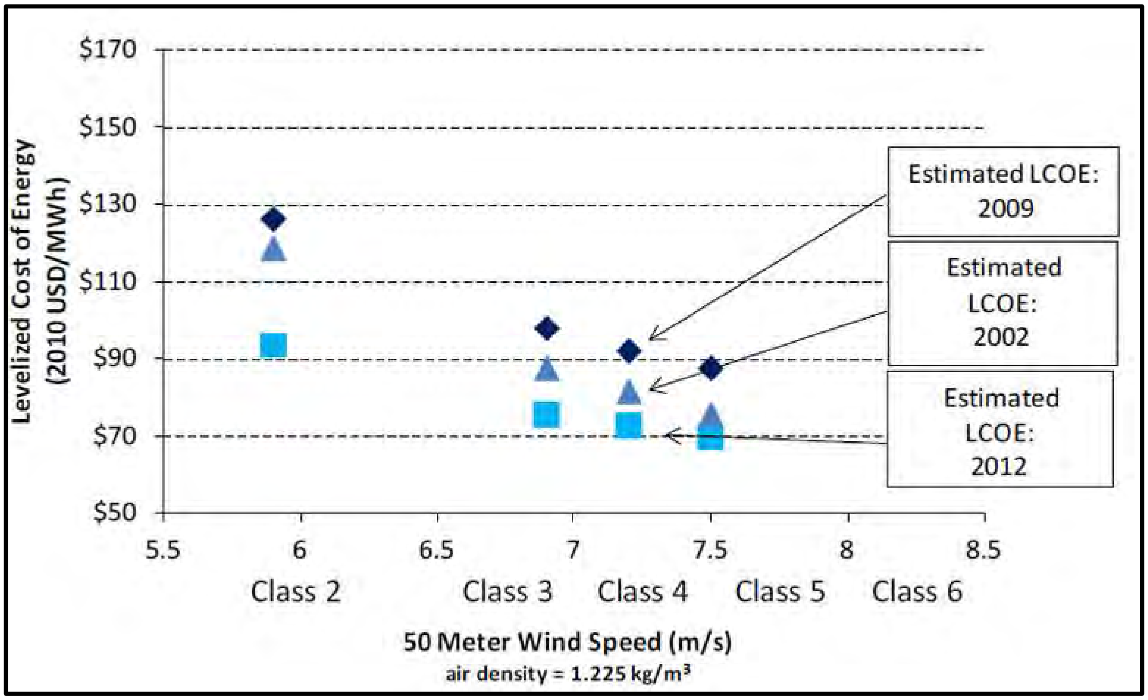

Figure 1.5: Estimated cost per MWh for wind power in Denmark [51]

Wind power is capital intensive, but has no fuel costs [52]. The price of wind power is therefore much more stable than the volatile prices of fossil fuel sources. The marginal cost of wind energy once a station is constructed usually less than 1-cent per kWh.

However, the estimated average cost per unit of electricity must incorporate the cost of construction of the turbine and transmission facilities, borrowed funds, return to investors (including cost of risk), estimated annual production, and other components, averaged over the projected useful life of the equipment, which may be in excess of twenty years. Energy cost estimates are highly dependent on these assumptions so published cost figures can differ substantially. In 2004, wind energy cost a fifth of what it did in the 1980s and some expected that downward trend to continue as larger multi-megawatt turbines were mass-produced [53]. As of 2012 capital costs for wind turbines are substantially lower than 2008 to 2010 but are still above 2002 levels [54]. A 2011 report from the American Wind Energy Association stated, Wind's costs have dropped over the past two years, in the range of 5 to 6 cents per kilowatt-hour recently about 2 cents cheaper than coal-fired electricity, and more projects were financed through debt arrangements than tax equity structures last year winning more mainstream acceptance from Wall Street's banks. Equipment makers can also deliver products in the same year that they are ordered instead of waiting up to three years as was the case in previous cycles. 5,600 MW of new installed capacity is under construction in the United States, more than double the number at this point in 2010. Thirty-five percent of all new power generation built in the United States since 2005 has come from wind, more than new gas and coal plants combined, as power providers are increasingly enticed to wind as a convenient hedge against unpredictable commodity price moves [55].

A British Wind Energy Association report gives an average generation cost of onshore wind power of around 3.2 pence (between US 5 and 6 cents) per kWh (2005) [56]. Cost per unit of energy produced was estimated in 2006 to be 5 to 6 percent above the cost of new generating capacity in the US for coal and natural gas: wind cost was estimated at $55.80 per MWh, coal at $53.10/MWh and natural gas at $52.50 [57]. Similar comparative results with natural gas were obtained in a governmental study in the UK in 2011 [35]. In 2011 power from wind turbines could be already cheaper than fossil or nuclear plants; it is also expected that wind power will be the cheapest form of energy generation in the future [58]. The presence of wind energy, even when subsidised, can reduce costs for consumers (€5 billion/yr in Germany) by reducing the marginal price, by minimising the use of expensive peaking power plants [59].

In February 2013, Bloomberg New Energy Finance (BNEF) reported that the cost of generating electricity from new wind farms is cheaper than new coal or new baseload gas plants. When including the current Australian federal government carbon pricing scheme their modeling gives costs (in Australian dollars) of $80/MWh for new wind farms, $143/MWh for new coal plants and $116/MWh for new baseload gas plants. The modeling also shows that even without a carbon price (the most efficient way to reduce economy-wide emissions) wind energy is 14% cheaper than new coal and 18% cheaper than new gas [46]. Part of the higher costs for new coal plants is due to high financial lending costs because of the reputational damage of emissions-intensive investments. The expense of gas fired plants is partly due to export market effects on local prices. Costs of production from coal fired plants built in the 1970s and 1980s are cheaper than renewable energy sources because of depreciation [46]. In 2015, Bloomberg New Energy Finance (BNEF) calculated The levelized cost of electricity (LCOE) prices per MWh energy in new powerplants (excluding carbon costs) : $85 for onshore wind ($175 for offshore), $66–75 for coal in the Americas ($82–105 in Europe), gas $80–100 [47, 48 & 60].

:

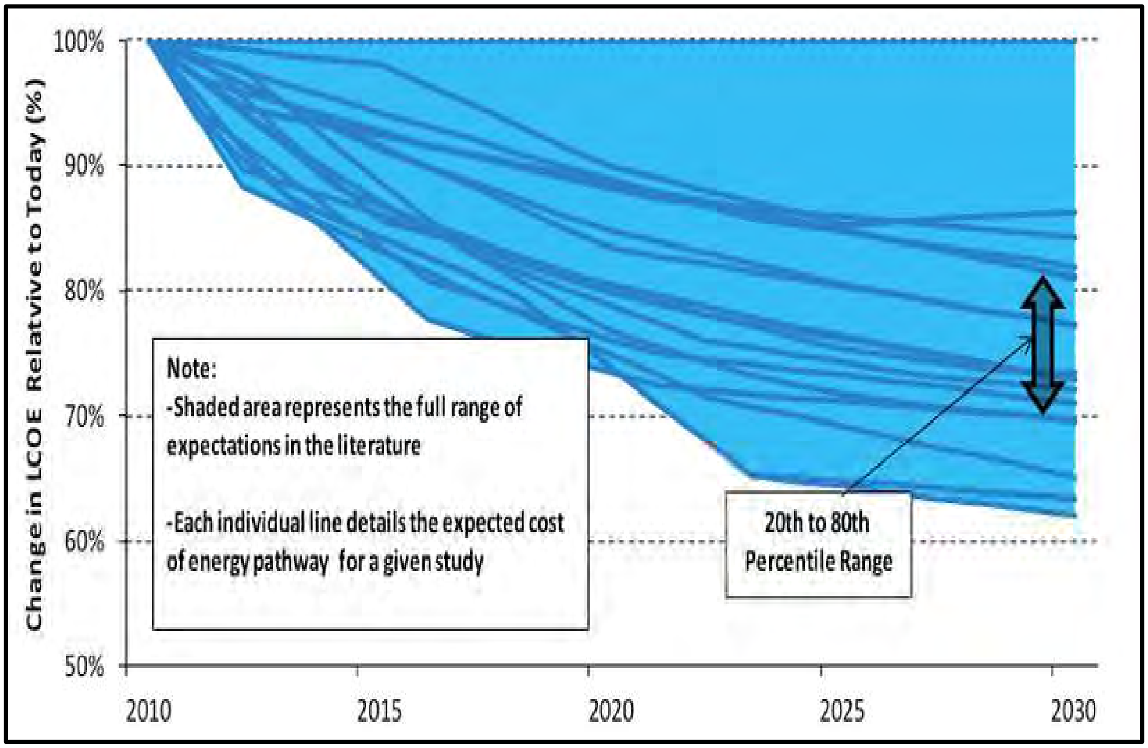

Figure 1.6: The National Renewable Energy Laboratory projects that the levelized cost of wind power in the U.S. will decline about 25% from 2012 to 2030 [50].

An EU study shows base cost of onshore wind power similar to coal, when subsidies and externalities are disregarded. Wind power has some of the lowest external costs [61].

This cost has additionally reduced as wind turbine technology has improved. There are now longer and lighter wind turbine blades, improvements in turbine performance and increased power generation efficiency. Also, wind project capital and maintenance costs have continued to decline [62]. For example, the wind industry in the USA as of early 2014 is able to produce more power at lower cost by using taller wind turbines with longer blades, capturing the faster winds at higher elevations. This has opened up new opportunities and in Indiana, Michigan, and Ohio, the price of power from wind turbines built 300 feet to 400 feet above the ground can now compete with conventional fossil fuels like coal. Prices have fallen to about 4 cents per kilowatt-hour in some cases and utilities have been increasing the amount of wind energy in their portfolio, saying it is their cheapest option [63].

A number of initiatives are working to reduce costs of electricity from offshore wind. One example is the Carbon Trust Offshore Wind Accelerator, a joint industry project, involving nine offshore wind developers, which aims to reduce the cost of offshore wind by 10% by 2015. It has been suggested that innovation at scale could deliver 25% cost reduction in offshore wind by 2020 [64]. Henrik Stiesdal, former Chief Technical Officer at Siemens Wind Power, has stated that by 2025 energy from offshore wind will be one of the cheapest, scalable solutions in the UK, compared to other renewables and fossil fuel energy sources, if the true cost to society is factored into the cost of energy equation [65]. He calculates the cost at that time to be 43 EUR/MWh for onshore, and 72 EUR/MWh for offshore wind [66].

1.11 Environmental Impact of Wind Power

The environmental impact of wind power when compared to the environmental impacts of fossil fuels, is relatively minor. According to the IPCC, in assessments of the life-cycle global warming potential of energy sources, wind turbines have a median value of between 12 and 11 gram CO_2 per kWh depending on whether off or onshore turbines are being assessed [67 & 68]. Compared with other low carbon power sources, wind turbines have some of the lowest global warming potential per unit of electrical energy generated [69].

While a wind farm may cover a large area of land, many land uses such as agriculture are compatible with it, as only small areas of turbine foundations and infrastructure are made unavailable for use [70 & 71].

There are reports of bird and bat mortality at wind turbines as there are around other artificial structures. The scale of the ecological impact may [72] or may not [73] be significant, depending on specific circumstances. Prevention and mitigation of wildlife fatalities and protection of peat bogs [74], affect the siting and operation of wind turbines.

Wind turbines generate some noise. At a residential distance of 300 metres (980 ft) this may be around 45 dB, which is slightly louder than a refrigerator. At 1 mile (1.6 km) distance they become inaudible [75]. There are anecdotal reports of negative health effects from noise on people who live very close to wind turbines [76]. Peer-reviewed research has generally not supported these claims [77, 78 & 79].

Aesthetic aspects of wind turbines and resulting changes of the visual landscape are significant [80]. Conflicts arise especially in scenic and heritage protected landscapes.

1.12 Pros & Cons of Wind Energy

In the U.S., the greatest source of human-caused greenhouse gas emissions is the power sector, at about 38%. The largest source of power is coal, which, even though it produces less than 40% of the power, produces over 70% of the power sector's greenhouse gas emissions. About 20% of the greenhouse gas emissions are from natural gas-fired power plants. Although wind turbines have become familiar in much of the U.S., wind power still 2013 only accounts for about 4% of the power sector.

The potential for wind energy is immense, and experts suggest wind power can easily supply more than 20% of U.S. and world electricity. The advantages and disadvantages of wind energy are detailed here to help you decide what the future of wind should be in the United States.

Advantages:

Revitalizes Rural Economies: Wind energy can diversify the economies of rural communities, adding to the tax base and providing new types of income. Wind turbines can add a new source of property taxes in rural areas that otherwise have a hard time attracting new industry to landowners.

Fewer subsidies: All energy systems are subsidized, and wind is no exception. However, wind receives considerably less than other forms of energy. According to Renewable Energy World magazine, conventional energy receives US$300 billion in subsidies per year, while renewable energy has received less than US$20 billion of tax-payers' money in the last 30 years. A study published by researchers at Harvard in 2011 found that the full life cycle cost of coal power is between about 9.5 and 27 cents per kilowatt-hour, most of which is paid by tax payers in the form of increased health-related costs. These "indirect" subsidies amount to between $175 billion and over $500 billion/year. (Numbers are in 2008 dollars. For more see here.)

Free Fuel: Unlike other forms of electrical generation where fuel is shipped to a processing plant, wind energy generates electricity at the source of fuel, which is free. Wind is a native fuel that does not need to be mined or transported, taking two expensive costs out of long-term energy expenses.

Price Stability: The price of electricity from fossil fuels and nuclear power can fluctuate greatly due to highly variable mining and transportation costs. Wind can help buffer these costs because the price of fuel is fixed and free.

Promotes Cost-Effective Energy Production: The cost of wind-generated electricity has fallen from nearly 40¢ per kWh in the early 1980s to 2.5-5¢ per kWh today depending on wind speed and project size.

Creates Jobs: Wind energy projects create new short and long term jobs. Related employment ranges from meteorologists and surveyors to structural engineers, assembly workers, lawyers, bankers, and technicians. Wind energy creates 30% more jobs than a coal plant and 66% more than a nuclear power plant per unit of energy generated.

National Security/Energy Independence: Wind turbines diversify our energy portfolio and reduce our dependence on foreign fossil fuel. Wind energy is homegrown electricity, and can help control spikes in fossil fuel cost. Distributed generation facilities, like many community wind projects, provide a safeguard against potential terrorist threats to power plants.

Supports Agriculture: It is not often a new crop emerges from thin air. Wind turbines can be installed amid cropland without interfering with people, livestock, or production.

Local Ownership: A significant contribution to the worldwide energy mix can be made by small clusters of turbines or even single turbines, operated by local landowners and small businesses. Developing local sources of electricity means we import less fuel from other states, regions, and nations. It also means our energy dollars are plowed back into the local economy.

Conserves and Keeps Water Clean: Turbines produce no particulate emissions that contribute to mercury contamination in our lakes and streams. Wind energy also conserves water resources.
For example, producing the same amount of electricity can take about 600 times more water with nuclear power than wind, and about 500 times more water with coal than wind.

Clean Air: Other sources of electricity produce harmful particulate emissions which contribute to global climate change and acid rain. Wind energy is pollution free.

Negligible Greenhouse Gases: The sources of most of our power, coal and natural gas, produce large quantities of greenhouse gases. (Coal much more than natural gas.) Wind power produces none, other than in the manufacture, installation and maintenance of the turbines. On average those greenhouse gases are offset by the clean power the turbines produce within 9 months of operation.

Mining & Transportation: Harvesting the wind preserves our resources because there no need for destructive resource mining or fuel transportation to a processing facility.

Land Preservation: Wind farms are spaced over a large geographic area, but their actual footprint covers only a small portion of the land resulting in a minimum impact on crop production or livestock grazing.

Disadvantages:

A Variable Resource: Wind Turbines produce electricity only when the wind blows. This variability is monitored and compensated in the same way utilities monitor demand changes each day, so there are not any actual changes in power supply for the end users.

Aesthetics: People have widely varied reactions to seeing wind turbines on the landscape. Some people see graceful symbols of economic development and environmental progress or sleek icons of modern technology. Others might see industrial encroachment in natural and rural landscapes. There are many ways to minimize the visual impact of wind turbines, including painting them a neutral color, arraying them in a visually pleasing manner, and designing each turbine uniformly.

Shadow Flicker: Shadow flicker occurs when the blades of the rotor cast a shadow as they turn. Research has shown the worst-case conditions would affect, by way of light alteration, neighboring residents a total of 100 minutes per year, and only 20 minutes per year under normal circumstances. Designers of wind farms avoid placing turbines in locations where shadow flicker would be a problem any significant amount of time.

Sound: Wind turbines are not silent. The sounds they produce are typically foreign to the rural settings where wind turbines are most often used, but as turbine technology has improved over the years, the amount of sound has fallen considerably. The sounds of wind turbines do not interfere with normal activities, such as quietly talking to one's neighbor.

Biological Resource Impacts: As with any construction project or large structure, wind energy can impact plants and animals, depending on the sensitivity of the area. Loss of wildlife habitat and natural vegetation are the primary wildlife concerns associated with wind energy. With modern turbines, mounted on tubular towers and whose blades spin only about 15 times per minute, bird collisions are now rare. Extensive environmental impact analysis is an integral part of project development to mitigate impacts as much as possible. The Audubon Society and Sierra Club both support wind energy development, because the environmental advantages far outweigh the disadvantages.

Construction: Wind systems can involve the transportation of large and heavy equipment. This can cause a large temporarily disturbed area near the turbines. Erosion is another potential environmental problem that can stem from construction projects. The single most reliable technique for limiting erosion is to avoid grading roads and to perform site reclamation post construction.

Radar: Radar interference by wind turbines is rare and easily avoided through technological improvements and proper siting of turbines that are close to sensitive areas. A number of U.S. government installations have both wind turbines and functional radar, and the British military has a track record of successfully addressing these challenges.

1.13 Wind Turbine

The Sun heats our atmosphere unevenly, so some patches become warmer than others. These warm patches of air rise, other air blows in to replace them and we feel a wind blowing.

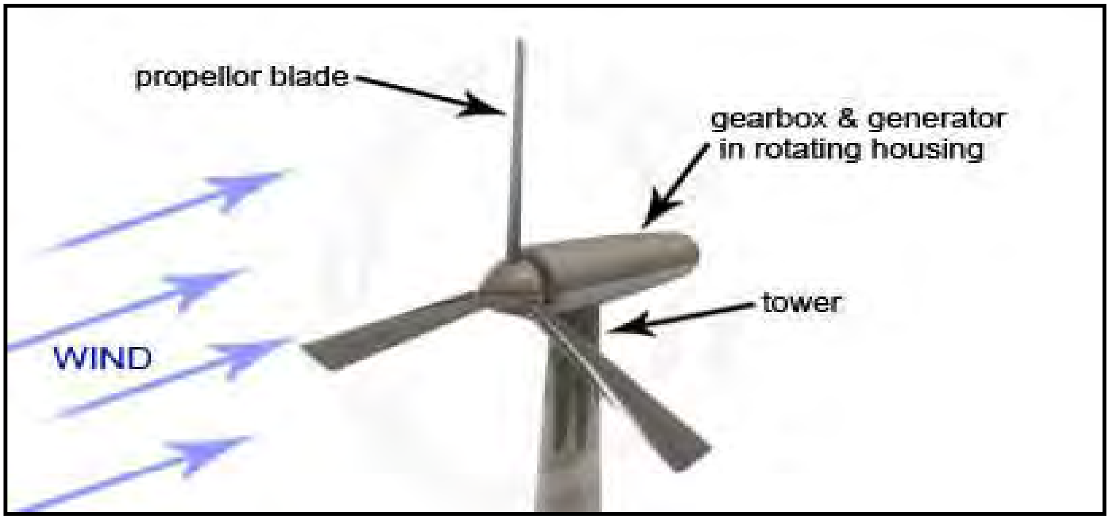

Figure 1.7: Wind turbine [81]

The wind blows the propeller round, which turns a generator to produce electricity. We tend to build many of these towers together, to make a wind farm and produce more electricity.

The more towers, the more wind, and the larger the propellors, the more electricity we can make. It's only worth building wind farms in places that have strong, steady winds, although boats and caravans increasingly have small wind generators to help keep their batteries charged.

The best places for wind farms are in coastal areas, at the tops of rounded hills, open plains and gaps in mountains - places where the wind is strong and reliable. Some are offshore.

To be worthwhile, you need an average wind speed of around 25 km/h. Most wind farms in the UK are in Cornwall or Wales. Isolated places such as farms may have their own wind generators. In California, several wind farms supply electricity to homes around Los Angeles.

The propellors are large, to extract energy from the largest possible volume of air. The blades can be angled to fine or coarse pitch, to cope with varying wind speeds, and the generator and propellor can turn to face the wind wherever it comes from. Some designs use vertical turbines, which don't need to be turned to face the wind.

The towers are tall, to get the propellors as high as possible, up to where the wind is stronger. This means that the land beneath can still be used for farming.

1.14 Prospects of Wind Energy in Bangladesh

Wind can be a vital source of energy if properly utilized and exploited. But before high-end projects are implemented, adequate research should be done to study the feasibility and determine a suitable type of project to implement. The primary parameter needed is wind speed and direction. Bangladesh is situated between 20.30-26.48 degrees North latitude and 88.04-92.44 degrees east.

In general, daily and seasonal changes as well as wind direction are important considerations while sitting wind systems. From five LGED stations, it was found that the average annual wind speed values at 10 m, 20 m, 30 m height for the five wind stations vary from 1.73 m/s to 4.17 m/s. The highest average annual wind speed (4.17 m/s) was observed in Kuakata and the lowest value (1.32 m/s) was observed in Khagrachari. The analysis showed that highest wind speed was found during summer at Kutubdia and Kuakata. The annual cycle of monthly average wind speed shows fairly [82].

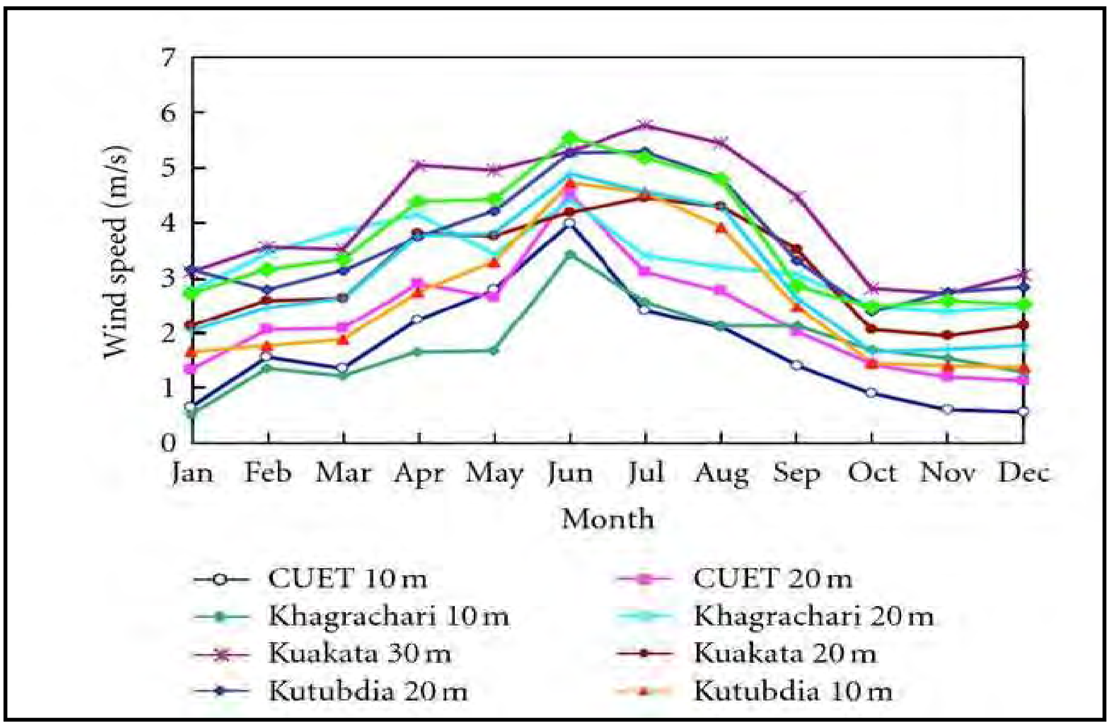

Figure 1.8: Monthly variation of wind speed for sites at different heights [82].

large seasonal variation, the appearance of which is typical for measurement sites, with minimum values in winter (October–March) and maximum values during summer (April–September). Similar variations also observed for the Bangladesh Centre for Advanced Studies (BCAS) Kutubdia and Kuakata stations [82].

The analysis of the daily cycle of the wind speed at different time instants, however, suggests that the dominance of daytime winds over night winds that is characteristic of mainland measurement sites also contributes to this feature. The hourly variation of wind speed is shown in Figure 1.9. While there is almost no dependence of the wind speed on the measurement time for Kuakata and a weak maximum becomes evident at afternoon for all stations. Such a variation is similar to that observed for at BCAS wind monitoring station of Kutubdia and Kuakata wind measurement sites [82]. A part of this cycle is obviously due to the local sea breeze. The typical spatial scale for changes of the diurnal cycle apparently

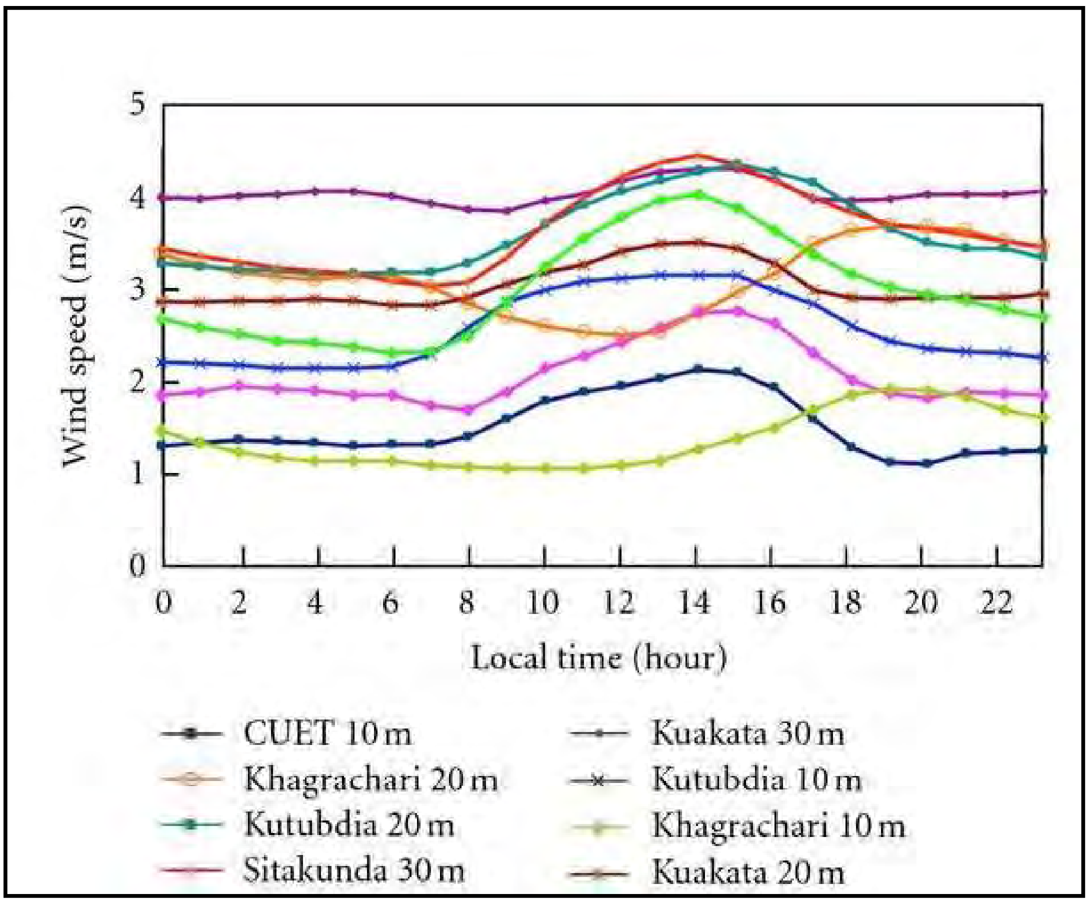

Figure 1.9: The hourly variation of wind speed [82].

depends on many factors such as the area covered by sea breeze, the geometry of the coastal region, or the mutual orientation of the land and sea, and the direction of air flow. From the above analysis it might be concluded that the daily cycle of wind speed should be taken into account when a wind farm is planned in the vicinity of a specific site.

1.14. 1 Wind Power Projects

Implemented Project

The potential of wind energy is limited to coastal areas, off-shore islands, rivers sides and other inland open areas with strong wind regime. In order to generate electricity from Wind Energy, BPDB installed 4x225 kW = 900 kW capacity grid connected Wind Plant at Muhuri Dam area of Sonagazi in Feni.

Another project of 1000 kW Wind Battery Hybrid Power Plant at Kutubdia Island was completed in 2008 which consists of 50 Wind Turbines of 20 kW capacity each.

Ongoing Projects

- Repairing work of the existing 900 kW grid connected Wind Power Project at Muhuri Dam of Sonagazi in Feni is going on.

- Repair and operation & maintenance of the existing Kutubdia 1000 kW Wind Battery Hybrid Power Project is underway

- Steps have been taken to install 15 MW Wind Power Plant across the coastal regions of Bangladesh after 1 year Wind Resources Assessment in Muhuri Dam Area of Feni, Mognamaghat of Cox’s Bazar, Parky Beach of Anwara in Chittagong, Kepupara of Borguna and Kuakata of Patuakhali. Wind Mapping is going on at Muhuri Dam area of Feni and at Mognamaghat of Cox’s Bazar by Regen Powertech Ltd. of India.

- Installation of Wind Monitoring Stations at Inani Beach of Cox’s Bazar, Parky Beach of Anwara, Sitakundu of Chittagong and at Chandpur under USAID TA project is underway.

Projects under Planning

 BPDB has planned to implement 50-200 MW Wind Power Project at Parky Beach area, Anawara in Chittagong on IPP basis.

 Power Division and BPDB have primarily identified 22 potential sites for Wind Resource Mapping in Bangladesh. Wind monitoring stations will be installed at these sites for comprehensive Wind Resource Assessment (WRA).

 PDB has also plan to expand On-shore Wind Power Plants along the coastline of coastal regions of Bangladesh.

1.15 Aim of the Present Work

Until now, both aerodynamic and structural works have been done on the vertical axis Savonius wind turbine in many parts of the world. Islam et al. [83] investigated the aerodynamic forces acting on a stationary S-shaped rotor and made an attempt to predict the dynamic performances from these forces. Islam et al. [84] analyzed the performance of S-shaped rotor by placing a plate in front of the returning blade. F. Diaz et al. [85] analyzed the drag and lift coefficient of Savonius wind machine, in order to obtain quantitative information about the aerodynamic performance of the Savonius rotor. However, little attention has been given on the static and dynamic characteristics when the number of blade of the Savonius rotor is increased. Nahar [86] analyzed the performance of S-shaped rotor by placing a plate in front of the returning blade.

The present work consists of finding static drag coefficients at the normal and tangential direction of the chord, static torque coefficient C_q at a fixed Reynolds number of a five bladed S-shaped Savonius rotor different angle of rotation ranging from $\alpha = 0^0$ to 360^0 by measuring the surface pressures blade of blades. The quasi-steady approach applied to the analysis of a Darrieus rotor has been finally considered for predicting the performance of the five bladed S-shaped Savonius rotor

Objectives with Specific Aims

The objectives of the present study are as follows:

1. To study the effect of the five bladed S-shaped Savonius rotor on the aerodynamic characteristics i.e. torque coefficient, drag coefficient etc. Determination of the variation of the separation point with the increase of rotor angle.
2. To determine the drag coefficient, torque coefficient by measuring the pressure difference between the convex and concave surfaces over the blades of five bladed S-shaped Savonius rotor.
3. Finally, a comparison will be made of the present research (for five bladed S-shaped Savonius rotor) in terms of torque coefficient, drag coefficient with other existing experimental results

1.16 Scope of the Thesis

The prime objective of the investigation is to observe the effect of the five bladed S-shaped Savonius rotor on the aerodynamic characteristics i.e. torque coefficient, drag coefficient etc.

The present research covers only the experimental investigation of pressure distribution over the blade surfaces of the Savonius rotor both on the convex and concave surfaces for different angles of rotation, ranging from 0^0 to 360^0 for every 10^0 interval. The several phases of the entire investigation are described in this thesis. Chapter Two provides with the brief description of the findings of several researchers in the field of flow over different types of Savonius rotor, Darrieus rotor and S-shaped rotor with-different conditions. Notable contributions were mainly made by E.H. Lysen, H.G. Bos, E.H. Cordes, J. Park, R.D. Littler, M.D. Huda, M.A. Selim, M.Q. Islam, A.K.M.S. Islam, A.C. Mandal, M. M. Razzaque, J. Gavalda, J. Massons, F. Diaz, T. K. Aldoss, M.A. Koth, T. Ogawa and H. Yoshida. Besides these, findings of several other researchers are also included in this chapter.

In chapter three, mainly an account of the experimental arrangements and procedures adopted for the investigation are presented. It includes the description of the wind tunnel, the constructional details of the test section and five bladed Savonius rotor used for the study. The experiment was conducted in the wind tunnel for only two dimensional uniforms cross flow keeping the velocity and turbulence intensity constant.

Chapter Four presents the derivation technique of different non-dimensional parameters both for static and dynamic aerodynamic characteristics.

Chapter Five presents the analysis concerning the results and discussions of the present experimental results, which are presented in graphical forms. In few cases, the existing experimental results of different researchers are correlated with the present one. Finally, the conclusions which are drawn from the present investigation are given in chapter Six. This chapter also includes an outline regarding further research in this field.

CHAPTER-2

REVIEW OF LITERATURE

CHAPTER 2

REVIEW OF LITERATURE

2.1 Introduction

Arising from the increasing practical importance of wind turbine aerodynamics, there have been, over the past few decades, an enormous increase in research works concerning laboratory simulations, full-scale measurements and more recently, numerical calculations and theoretical predications for flows over a wide variety of Savonius rotors. Researchers in different countries have contributed greatly to the knowledge of analytical prediction methods of wind turbines, but the major part of the reported works are of fundamental nature involving the flow over horizontal axis wind turbine and vertical axis Darrieus rotor. Most of the researchers have conducted research works on either two semi cylindrical bladed Savonius rotor or S-shaped rotor with various flow parameters. A brief description of some of the papers related to the present work is given in this chapter.

2.2 Historical Background

From the ancient period people have been working on various classes of wind contrivances to extract energy from the wind. Works on windmills have probably been started from 2000 B. C. The period from the ancient time up to the end of the nineteenth century may be categorized as the ancient development period while that from the end of nineteenth century up to date may be termed as the modern development period.

In the ancient development period, in the middle of seventh century, Persian vertical axis windmill circa (Figure 2.1) was constructed which was used to grind grain. That kind of windmill was working up to about twelfth century, when simultaneously in France and England different type of windmills were made whose purpose were to grind grain and pump water. These windmills were of horizontal axis types. Up to the end of nineteenth century people were working with these classes of windmills only.

At the end of nineteenth century, the first modern windmill of horizontal axis type with

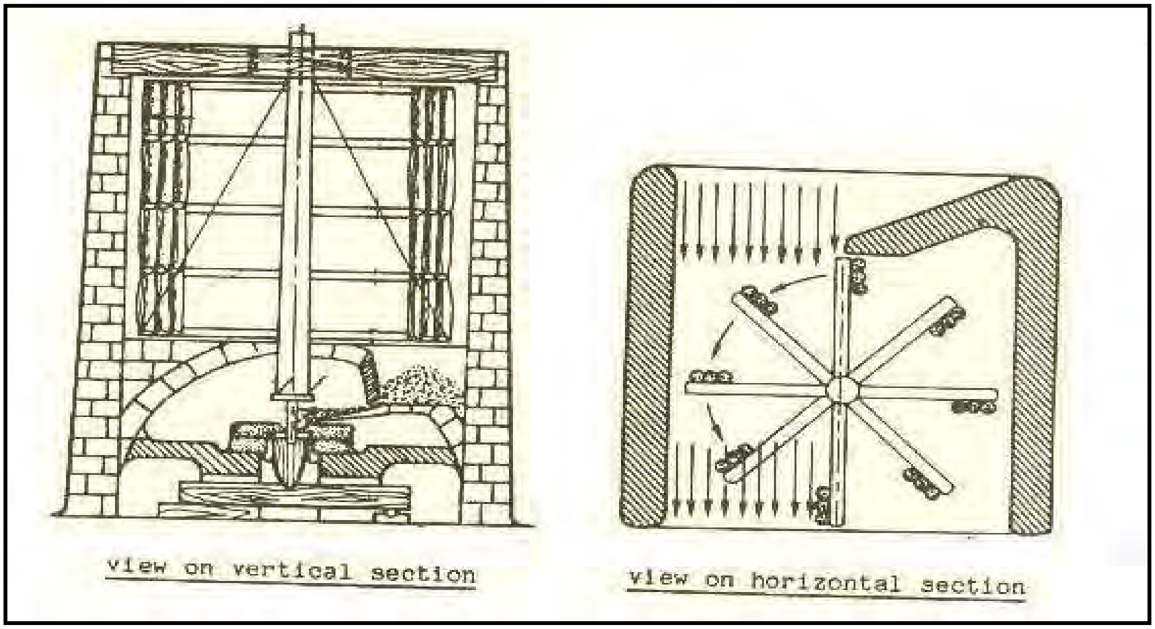

Figure 2.1: Persian windmill of vertical-axis type

multi-blade was built in Denmark to produce electricity. It was the beginning of the modern development period. Starting from that time people in different countries especially in rural America have been constructing a large number of multi-bladed wind turbines for pumping water and generating electricity. Afterwards, as a consequence of development works for several years, two or three bladed propeller type of windmills with airfoil shaped blades were built in near about 1925. In 1931, a 100 kW Russian horizontal axis wind turbine was constructed, while in 1934, the large 1,250 kW Smith- Putnam horizontal-axis wind turbine was built.

Modern development period have really begun with the development of horizontal axis wind turbines. In 1924, Finnish Engineer S. J. Savonius constructed the first Savonius rotor of vertical axis type (Figure 2.2) and he conceived the idea from the Flettner's Rotor. In 1925 G. J. M. Darrieus of France, proposed for United States patent a new type of wind turbine designed for the generation of power. The patent issued in 1931 as Number 1,835,018 was for a "turbine having its rotating shaft transverse to the flow of the current". The straight-bladed configuration was also covered in the original Darrieus patent. This kind of wind machine is called Darrieus turbine (Figure 2.3) after the name of G. J. M. Darrieus.

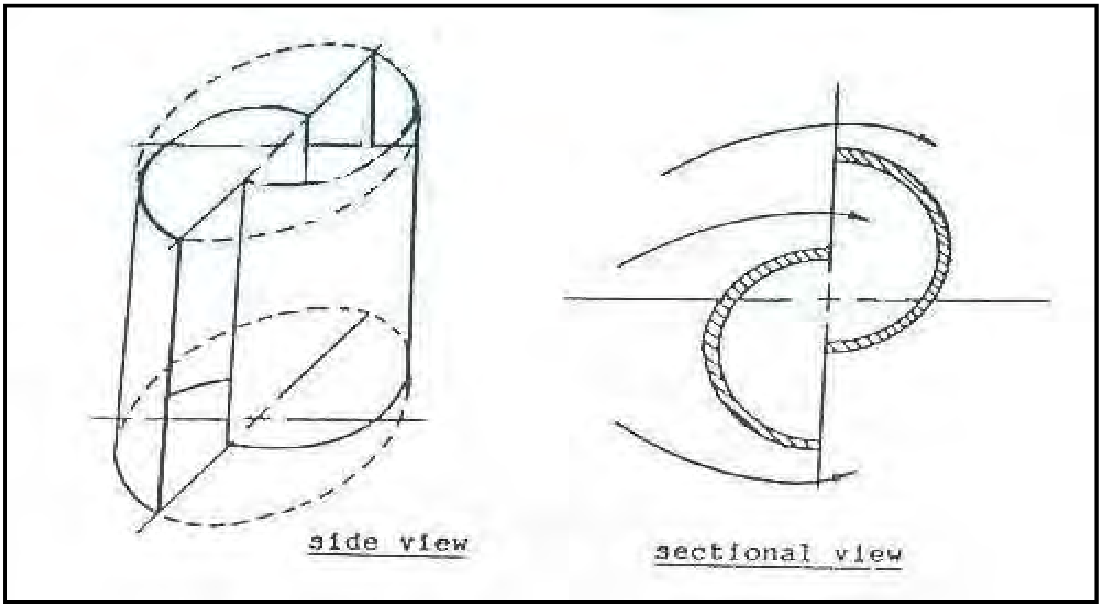

Figure 2.2: Savonius rotor

Since the beginning of the twentieth century, researchers in the various parts of the world had been giving much effort in the development works of the wind turbines but from about the middle of this century, it began to lose its momentum for further development. In about 1970's people took renewed interest in this field. Especially in 1973 with oil embargo, people were thinking regarding the alternate sources of energy. As a result in many developed and developing countries, a lot of new projects concerning the development of wind turbines have been taken.

Only during the last decade in the different countries enormous attention has been paid in the field of performance prediction method applicable to wind turbines. As an outcome, a number of analytical prediction methods have been developed. Works have also been extended to both the static and dynamic analyses of wind turbines. Different types of design methods have been worked out in many places. Still there exists no good and reasonable analytical performance prediction method especially for a high solidity Darrieus wind turbine.

2.3 Literature Concerning S-Shaped Savonius Rotor

Islam et al. [2] investigated the aerodynamic forces acting on a stationary S-shaped rotor and made an attempt to predict the dynamic performance from these forces. The work was done by measuring the pressure distribution over the surfaces of the blades. The measurement were carried out in a uniform flow jet produced by an open circuit wind tunnel and at a constant wind speed of 8.9 m/s which corresponds to a Reynolds number (Re = U_0 D/ν) of $1.1x10^{5.}$ The results indicate that flow separates over the front and back surfaces of the blades and the point of separation depends on the rotor angle.

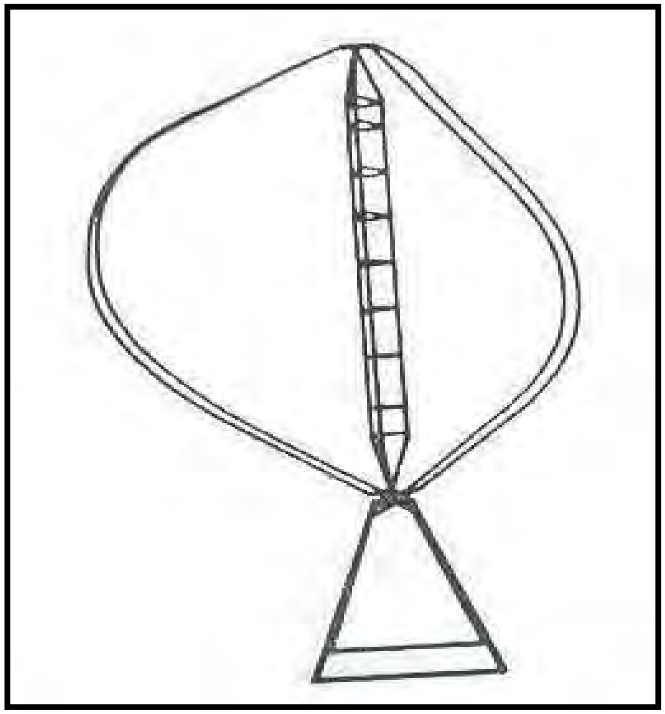

Figure 2.3: Darrieus wind turbine

The pressure difference was observed between the two surfaces of each blade, which in turn, gives drag coefficients. The drag and hence, the torque of each blade varies with rotor angle and becomes maximum at α = 45° for the advancing blade and at α = 105° for the returning blade. The net torque is highest at α = 45° and becomes negative in the range of rotor angle between 135° to 165°.

Islam et al. [83] analyzed the performance of S-shaped rotor by placing a flat plate in front of the returning blade. They found that the power coefficient of a S-rotor was dependent on the Reynolds number and the value of (power coefficient) increased with Reynolds number in the range of the Reynolds number studied and maximum 20% of power coefficient could be increased by using the deflecting plate which occurs at a deflecting angle of 35° for b = 0.5D, where b = distance between plate and rotor center and D = diameter of the rotor. Bowden, G. J. and McAleese, S. A. [87] made some measurements on the Queensland optimum S-shaped rotor to examine the properties of isolated and coupled S-shaped rotor. In particular, it is shown that the efficiency of the turbine is 18%, which is lower than the figure of 23% given by earlier workers. In the experimental setup the University of New South Wales (UNSW) open jet air-stream, diameter 0.76 m, was used to produce wind speeds in the range 0 to 30 m/s. The turbulence $\sqrt{u^2}/V\alpha$ in the jet stream was low. Wind flow measurements were investigated using 'tell-tales' (light pieces of cotton attached to a probe) and a stroboscope. In this way, it was possible to detect the direction of the air flow relative to the angular position of the rotor blades. Many photographs were taken and later used to construct a visual air flow pattern around the rotor. The linearized hot-wire anemometer, on the other hand, enabled measurements to be made of velocity magnitudes and fluctuations to an upper frequency limit of 5 kHz. It cannot, however, be used to measure direction. The hot-wire anemometer linearizer was based on a design due to the Institute of Sound and Vibration Research (ISVR), Southampton University, U. K. In general, a storage oscilloscope was used to record the data, particularly from the more structured turbulent regions. However, measurements of turbulence intensity were also made by connecting an rms voltmeter to the output of the hot wire linearizer. The results of this research were subsequently used to suggest that some form of active coupling between Savonius rotors might be possible. In particular, it has been shown that if two counter rotating rotors are placed side by side, a natural phase locking occurs between the two turbines.

2.4 Literature Concerning Vertical Axis Darrieus Wind Turbine

The most simple prediction method for the calculation of the performance characteristics of a Darrieus wind turbine is the single streamtube mode. It has been introduced first by Dr. Templin [88] in 1974. In this model the whole turbine is assumed to be enclosed within the single streamtube. Dr. Templin first incorporated the concept of the windmill actuator disc theories into the analytical model of a Darrieus wind turbine. In the actuator disc theory the induced velocity (rotor axial flow velocity) is assumed to be constant through the "disc" and is obtained by equating the stream wise drag with the change in axial momentum. In the assumption of Templin, the actuator disc is considered as the surface of the imaginary body of revolution. It is assumed that the flow velocity is constant through the upstream and the downstream faces of the swept volume. This theory presented by Templin is the first approach to permit numerical design calculations for a vertical-axis Darrieus wind turbine.

An analytical method using single streamtube model is presented by Noll and Ham [89] for the performance prediction of a vertical-axis wind turbine with straight blades which are cyclically pitched. They added the effect of strut drag, turbulent wake state and dynamic stall to their analytical method.

An improvement to the above method is the multiple streamtube model introduced by Wilson and Lissaman [90]. In this model the swept volume of the turbine is divided into a series of adjacent, aerodynamically independent streamtubes. Blade element and momentum theories are then employed for each streamtube. In their method, they consider the flow as inviscid and incompressible for the calculation of the induced velocity through the streamtube. As a result, there appears only the lift force in the calculation of induced velocity. Wilson et al. considered the theoretical lift for their calculation. This induced velocity varies over the frontal disc area both in the vertical and the horizontal directions. Atmospheric wind shear can be included in the multiple streamtube models. Multiple streamtube models are still inadequate in its description of the flow field. Wilson's model can be applied only for a fast running lightly loaded wind turbine.

Strickland [91] in his paper presents a multiple streamtube model for a vertical axis Darrieus turbine. He finds the induced velocity by equating the blade clement forces (including airfoil drag) and the change in the momentum along each streamtube. The basic difference between Wilson's and Strickland's model is that Wilson used the lift force (theoretical) only in the calculation of induced velocity while Strickland added the effect of drag force as well for the similar calculation. Wilson's model gives first convergence while Strickland's model gives slow convergence.

An improved version of multiple streamtube method is presented by Read and Sharpe [92] for vertical-axis Darrieus wind turbines. In their model, the parallel streamtube concept is dispensed with and the expansion of the streamtube is included. It is strictly applicable to low solidity lightly loaded wind turbines with large aspect ratio. It can predict the instantaneous aerodynamic blade forces and the induced velocities better than that by the conventional multiple streamtube model. But prediction of overall power coefficients cannot be made with reasonable accuracy. It usually gives lower power than that obtained experimentally.

In the paper presented by Paraschivoiu and Delclaux [93], they have made improvements in the double multiple streamtube model. They consider the induced velocity variation as a function of the azimuthal angle for each streamtube. They have added a new formulation for an approximate Troposkien shape by considering the effect of gravitational field and a semi-empirical dynamic stall model.

Paraschivoiu, Fraunie and Beguier [94] introduce in their paper the expansion effects of the streamtubes through the rotor and these are included with the double multiple streamtube model. With the measured and the predicted data they observe that streamtube expansion effects are relatively significant at high tip speed ratios.

Fanacci and Walters [95] presented a two dimensional vortex model applicable to a straight-bladed wind turbine. In their analysis, they consider the angle of attack very small thereby eliminating the stall effect.

Holme [96] presents a vortex model for a fast running vertical-axis wind turbine having a large number of straight, very narrow blades and a high height-diameter ratio (in order to make a two dimensional flow assumption). The analysis is valid for a lightly loaded wind turbine only.

Wilson [97] also introduces a two dimensional vortex analysis to predict the performance of a giromill. In his method he does not take into account the stall effect, because the angle of attack is assumed to be small.

2.5 Literatures Concerning Two Semi-cylindrical Bladed Savonius Rotor

F. Diaz et al. [3] analyzed the drag and lift coefficients of Savonius wind machine, in order to obtain quantitative information about the aerodynamic performance of the Savonius rotor. The experiments were carried out in a low turbulence open jet of 30 x 50 cm section outlet, which provides an air speed adjustable between 0 and 30 m/s. The results of this work showed that for e/d = 1/6, at which the rotor generates the optimum power, the drag and lift coefficients are little dependent on the operating conditions (Reynolds number, tip speed ratio λ) if λ is near the optimum value $\lambda \approx 1$. There are three findings of this work: (a) the maximum efficiency of the Savonius rotor, in terms of power coefficient, takes place for $\lambda \approx 1$, and that C_D decreases sharply when λ increases or decreases from this value, (b) for a given Reynolds number, as the tip speed ratio increases from zero, the drag values are maintained practically constant, $C_D \approx 1.5$ in the interval ranging from $\lambda = 0$ to $\lambda = 1.25$. The most interesting zone for power extraction is located near $\lambda \approx 1$, where C_D shows minimal values. For tip speed ratios greater than 1.25, the drag coefficient increases, (c) in a wide interval around $\lambda = 1$ (the most important region of operation of the Savonius rotor) the lift coefficient remains practically constant at $C_L \approx 0.5$.

Sawada, T., Nakamura, M. and Kamada, S., [98] experimentally studied the mechanism of rotation of Savonius rotor which have two semi-cylindrical blades. The force acting on a blade is measured in a water tank for both cases. Where a rotor is at rest and where it is rotated. A flow around the rotor is observed by using aluminum powder floating on the water surface. Although the Savonius rotor is classified as a resistance type, the lift produces a torque in a pretty wide range of blade angles relative to the flow. The researchers concluded that (a) when the rotor is at rest, the rotor with overlap ratio a/d =0.21 produces a positive torque at any attack angle, (b) the lift around 240° ~ 330° contributes a lot to the torque occurring when the rotor is rotated. Although the Savonius rotor is classified as a resistance type, the lift produce a torque in a pretty wide range of angles relative to the flow, (c) when the rotor is rotated, the effect of the pressure recovery by the flow through the overlap portion on the lift is little for the rotor of a/d = 0.21. For the rotor of a/d = 0.51, the existence of a flow through the center of the rotor contributes to the production of a negative torque opposing the clockwise rotation.

Taha K. Aldoss and Khalid M. Obeidat [99] analyzed the performance of two Savonius rotors running side by side at different separations using the discrete vortex method. Two configurations were considered. The torque and power coefficients were computed and compared with the available experimental results presented by Aldoss and Najjar in an earlier paper.

R. D. Litler et al. [100] made comparative tests of the Savonius rotor at constant Reynolds number. They suggested that a plain S-rotor may be as good as or better than the conventional Savonius rotor with an inter-vane gap. A single S-rotor gives a $C_p > 0.15$ (0.225 uncorrected wind-tunnel value); although duplex rotors have given $C_p > 0.18$ (0.32 uncorrected value). Comparative particle flow visualization studies within these rotors (Savonius rotor with conventional gap, S-rotor with no gap, and a rotor with separated vanes ('negative' gap) in a water-channel) suggest the importance of attached flow round the convex surfaces of the vanes, the doubtful value of the conventional gap, and the importance of vane shape.

Sivasegaram, S. and Sivapalan, S. [101] made an experiment in improving the sectional geometry of slow-running vertical-axis wind rotors of the Savonius type has resulted in considerable improvement in rotor performance. They suggested that further improvement in power output from a rotor of given overall dimensions demands the use of power augmenting systems. The influence of important design parameters of the augmenting system and that of wind direction has been investigated and the system configuration giving maximum power augmentation has been determined. They showed that an eighty percent increase in power output could be achieved using a pair of vanes of moderate size.

Islam et al. [102] investigated aerodynamic characteristics of a Stationary Savonius rotor of two semi-cylindrical blades. The test was carried out in a uniform flow jet produced by an open circuit wind tunnel. The exit of the wind tunnel consists of a square section nozzle with a side length of 500 m. The rotor was placed at the jet axis and 750 mm. downstream of the nozzle exit. This study was carried out at a constant wind speed of U_0 = 13.3 m/s i.e. at Reynolds number, Re = $2x10^5$. The results of this work showed that flow separates over the convex surface of the blades and the separation point moves towards the leading and trailing edges of the advancing and returning blades respectively as the rotor angle increases from 0° to 90°. Beyond 90°, flow separates over the convex surface of the returning blade only. They also found that the difference in pressure on the convex and concave surfaces produces drag coefficients, and C_t in the normal and tangential directions of the chord. Drag coefficients, C_n and C_t are functions of rotor angle and their resultant reaches maximum value at $\alpha = 120°$ and minimum value at $\alpha = 0°$.

CHAPTER-3

EXPERIMENTAL SET UP AND PROCEDURE

CHAPTER 3

EXPERIMENTAL SET-UP AND PROCEDURE

3.1 Introduction

The objectives of the investigation of wind loading on the five bladed S-shaped Savonius rotor have been analyzed essentially with the help of a subsonic wind tunnel, experimental set-up of the Savonius rotor and an inclined multimanometer. Pressure distribution over the convex and concave surfaces of each blade of the Savonius rotor placed normal to the approaching uniform flow was measured with the help of the multimanometer. The following sections describe in detail regarding the experimental set-up and techniques adopted for the investigation.

3.2 The Wind Tunnel

The open circuit subsonic wind tunnel was 6.55 m (21.5 ft) long with a test section of (49cmx 49cm) cross-section. Figure 3.1 depicts the wind tunnel used for the experiment. The successive sections of the wind tunnel comprised of converging mouth entry, Perspex section, rectangular section, fan section (two rotary axial flow fans), butterfly section, silencer with honeycomb section, an eddy breaker, diverging section, converging section, 2 ft long rectangular section, 1 ft long flow straightened section, 2 ft long rectangular exit section. The central longitudinal axis of the wind tunnel was maintained at a constant height from the floor.

The converging mouth entry was incorporated into the system for easy entry of air into the tunnel and to maintain uniform flow into the duct free from outside disturbances. The exposed surface of the mouth entry was covered with cloth for extra protection against dust and for uniform flow.

The Perspex section was (30.48 cm x 30.48 cm) 61 cm long which may be used for the experiment of flow around a circular cylinder. A 92 cm long rectangular diverging section was used to make the flow uniform from rotation.

1. Converging Mouth Entry
2. Perspex Section
3. Rectangular Diverging Section
4. Fan Section
5. Butterfly Section
6. Silencer with Honey Comb Section
7. Diverging Section
8. Converging Section
9. Rectangular Section
10. Flow Straightener Section
11. Rectangular Exit Section

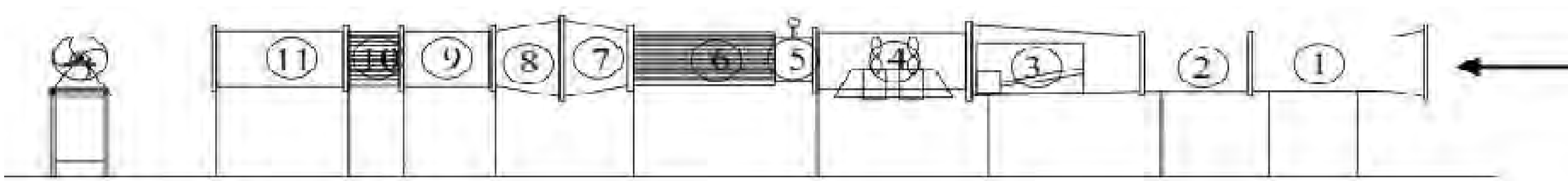

Figure 3.1: Schematic diagram of wind tunnel

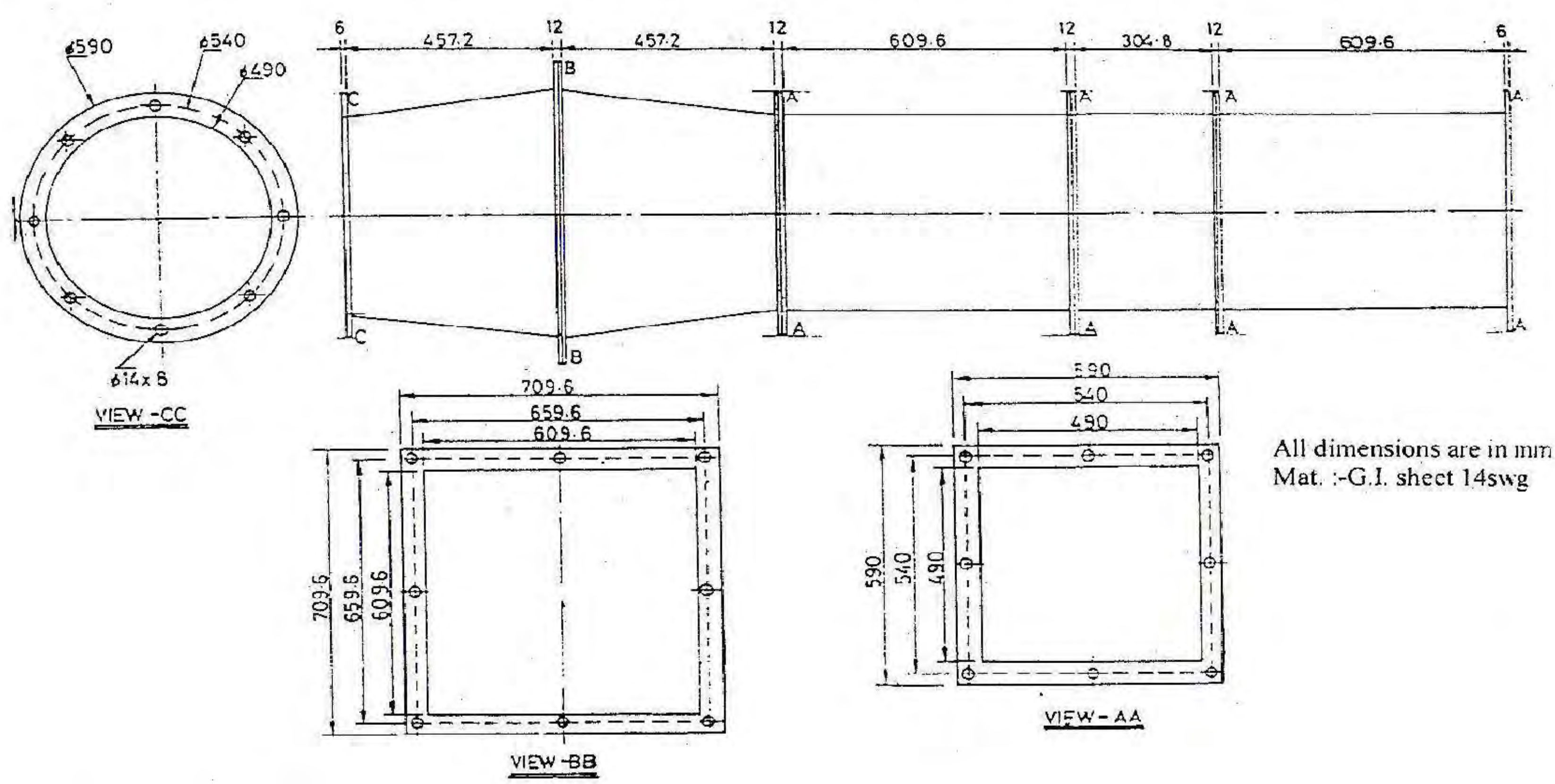

Figure 3.2: Modification part of the wind tunnel

The induced flow through the wind tunnel was produced by a two-stage rotating axial flow fan of capacity 30,000 cfm at the head of 15.24 cm of water and rpm 1475. A butterfly valve, actuated by a screw thread mechanism, was placed behind the fan and was used to control the flow.

A silencer was fitted at the end of the flow controlling section in order to reduce the noise of the system. At the same time flow straightening system was performed in this section. All these sections were in the existing sections of the wind tunnel. Further modification was done to make the flow uniform (Figure 3.2). The modified parts were diverging section, converging section, 2 ft long square section, flow straightener section and 2 ft long square exit section. The diverging and converging sections of the wind tunnel were 46cm long and made of 14 SWG G. I. sheets. The angle of divergence and convergence was 7°, which was done with a view to minimize expansion and contraction loss and to reduce the possibility of flow separation. Other three square sections were used to make the flow straight and uniform.

3.3 The Five Bladed S-shaped Savonius Rotor

The constructional details of the test section are shown in the Figures 3.3 (a), 3.3 (b) and 3.4 (a), 3.4 (b). The Savonius S-shaped rotor was made up of five blades, chord length = 105 mm, rotor diameter = 260 mm and height, H = 300 mm. The blades were made of PVC material. The whole rotor was fixed on an iron frame by using two side shafts and two ball bearings.

The pressure measurements were done at 12 pressure tappings on one blade of the five bladed S-shaped Savonius rotor. The tappings were made with copper tubes of 1.5mm outer diameter and 10mm length which were press fitted to the tapping holes. The tapings were located at the mid-plane of one side of each blade, so that pressure distribution at every 10° on the blade surface could be measured. The pressure tappings were connected to an inclined multimanometer (manometric fluid was water and had an accuracy of ± 0.1 mm of water column) through 2mm PVC tubes. The pressures were measured at every 10° interval of rotor angle so that a detailed picture of the aerodynamic loading and torque characteristics could be obtained.

Figure 3.3 (a,b): Constructional details of the test section

Figure 3.4 (a,b): Test acting on the blades

3.4 Experimental Procedure

The flow velocity in the test section was kept constant at 13m/s. The Reynolds number based on the rotor diameter D = 0.26 m was 2.1×10^5. The effect of temperature was considered in this experiment and the experiment was carried out at atmospheric temperature i.e. at T = 30°C where kinematic viscosity of air was $\nu = 1.6 \times 10^{-5}$ m^2/s.

Before measuring the pressure distribution the mean velocity was measured in a vertical plane 75 cm downstream from the exit of the wind tunnel without placing the rotor by means of an anemometer. The measured velocity distribution was uniform which can be seen from the Figure 3.5.

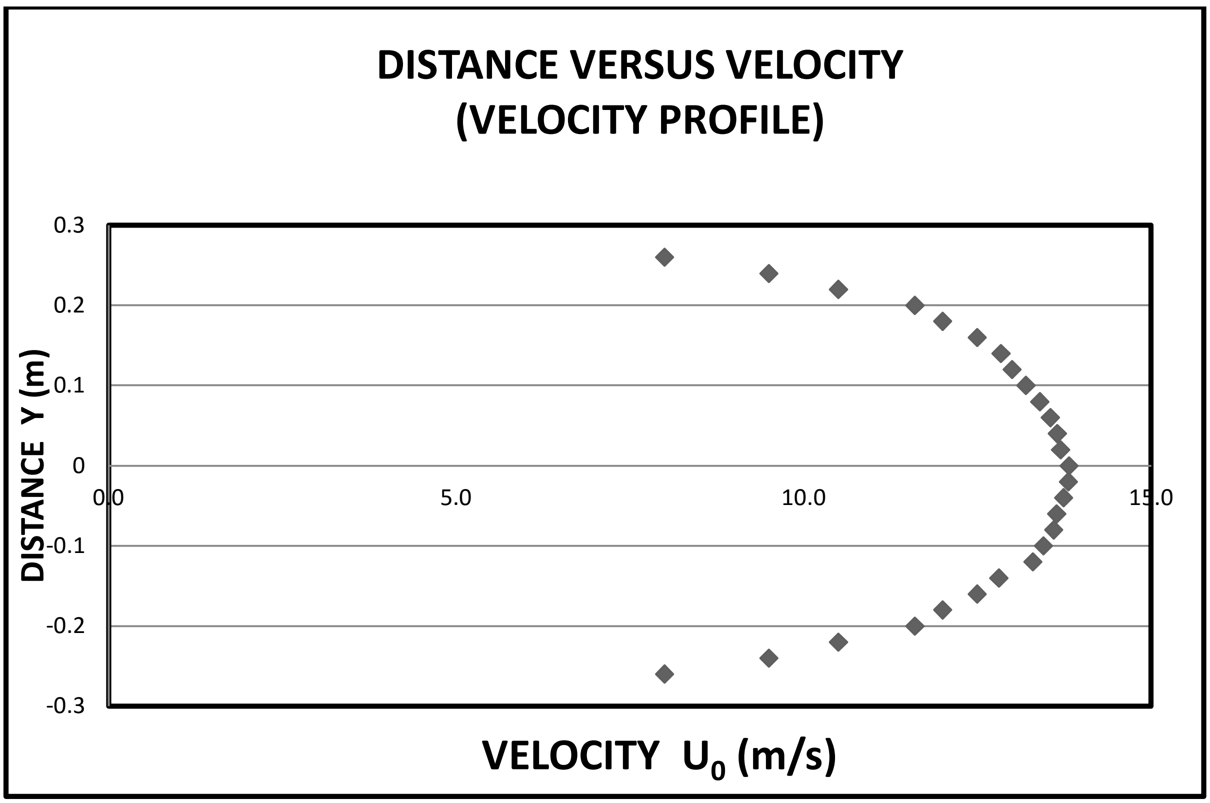

Figure 3.5: Velocity distribution in upstream side of test section

The pressure distribution over the blade surfaces were measured step by step by the multimanometer. At first, power was not supplied to the wind tunnel and the Savonius rotor with the frame placed 75 cm in front of the exit section of the tunnel on a table. By fixing one blade of the rotor parallel to the free stream velocity i.e. parallel to the horizontal which was called the reference plane and from this plane angle of rotation was measured. In this case, the first blade was at 0° angle of rotation, exposing the convex surface in front of free stream of air, so the other four blades were in the position of 72°, 144°, 216° and 288° angle of rotation respectively.

The rotor was then made static by fixing the one side shaft of the rotor with the angle fixing device. Power was then supplied to the tunnel to flow the free stream of air with uniform velocity over the blades of the rotor. Pressure on the convex surface of blades was measured at a particular rotor angle, fixing the rotor at static condition. Gradually, pressure on the convex surface was measured in this process for every 10° interval of rotor angle up to 350° angle of rotation. The same steps were performed for the measurement of the pressure on the concave surfaces.

At a particular rotor angle , the rotor blades experience forces (per unit span length) due to the pressure difference between the concave surface and convex surface and these forces can be resolved into two components F_n and F_t. Note that, the rotor was rotated only in the direction of the flow and the pressure difference was made by subtracting the pressure of the convex surface from the concave surface pressure, as maximum time of rotation the concave surface was exposed to the free stream.

CHAPTER-4

DERIVATION TECHNIQUE OF NON-DIMENSIONAL PARAMETERS

CHAPTER 4

DERIVATION TECHNIQUE OF NON-DIMENSIONAL PARAMETERS

4.1 Introduction

The local surface pressure on the blade surfaces of the rotor were measured relative to the free upstream static pressure prevailing in the test section of the wind tunnel. The data obtained experimentally are presented in terms of non-dimensional coefficients. The equations of coefficient of pressure, normal and tangential drag, torque, total static torque are derived briefly in this chapter.

4.2 Derivation of Aerodynamic Characteristics

Aerodynamic characteristics are derived in two steps

Step 1: From the experimental data pressure coefficients both for concave and convex surfaces of blade are calculated for angle of rotation ranging from 0^0 to 350^0.

Step 2: Using the pressure difference between concave and convex surfaces of blades of the Savonius rotor, the drag coefficients in normal and tangential directions were calculated. The flow pattern produced by the rotor blade is characterized by high turbulence, unsteadiness and flow separation. The combined effect of these flow features in turn produces pressure differences result in aerodynamic forces and hence torques. These forces can be resolved components F_n and F_t along normal and tangential directions of the rotor chord.

4.2.1 Pressure Coefficient

In the experiment, the pressure measurements were made at 12 pressure tappings on each blade for the angle of rotation (α) of every 10° interval ranging from 0° to 350° both on the convex and concave surfaces. Using these raw data pressures, coefficient on convex surfaces (C_{px}) and pressure coefficient on concave surfaces (C_{pe}) of the blades were calculated by using the following expression

$$C_p = \frac{P - P_o}{\frac{1}{2}\rho U_0^2} \tag{4.1}$$

Where,

$p-p_0$ = Difference between blade and atmospheric pressure in Pascal

ρ = Density of air = 1.2 kg/m^3

U_0 = Free stream velocity, 13 m/s

4.2.2 Drag Coefficient

These pressure differences between concave and convex surfaces of the blade result in aerodynamic forces and hence torques. These forces can be result in aerodynamic forces and hence torques. These forces can be resolved into component F_n and F_t along normal and tangential directions of the rotor chord Shown in Figure 4.1

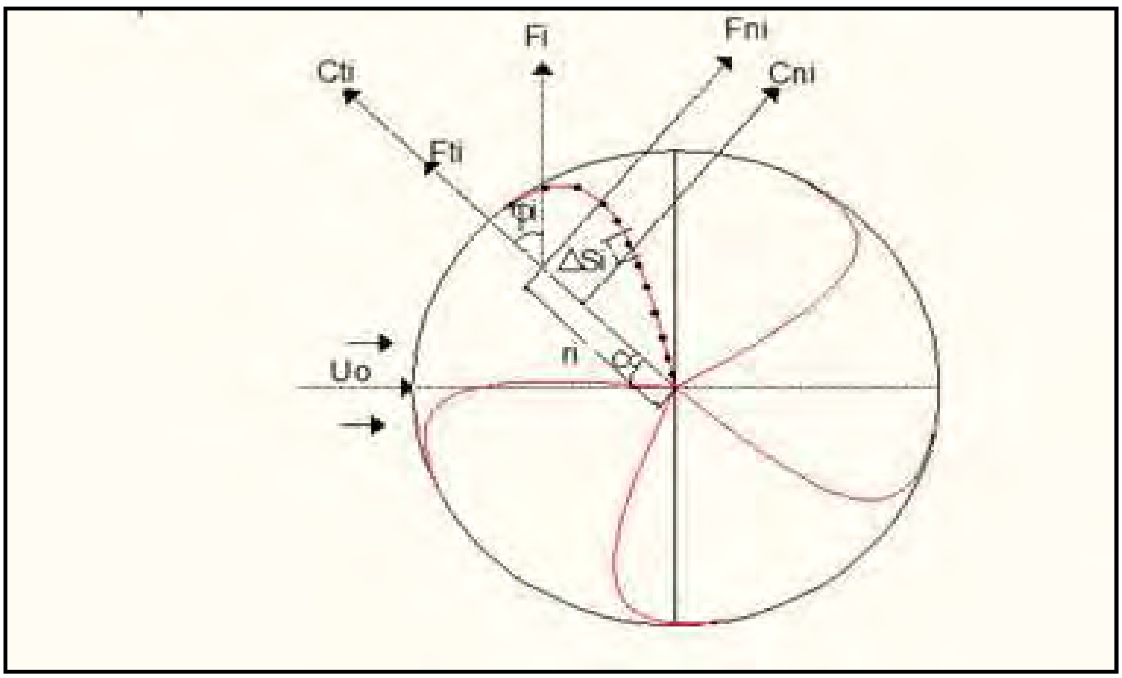

Figure 4.1 Pressure Tapping and Forces acting on a blade of five bladed S-shaped Savonius rotor.

The corresponding Drag coefficients can be expressed as

$$C_{ni} = \frac{F_{ni}}{\frac{1}{2}\rho U_0^2 R} \tag{4.2}$$

$$C_{ti} = \frac{F_{ti}}{\frac{1}{2}\rho U_0^2 R} \tag{4.3}$$

Where subscript i indicate the pressure tapping number.

The forces Fn and Ft can be evaluated from the pressure differences as

$$Fni = \Delta P_i \Delta S_i \sin\phi_i \tag{4.4}$$

$$Fti = \Delta P_i \Delta S_i \cos\phi_i \tag{4.5}$$

Where ΔP_i is the pressure difference between the concave and convex surfaces of the blade at a particular pressure tapping, ΔS_i is the chord length around the tapping, where a uniform pressure is assumed, ϕ_i is the angle between the normal of segment and direction of flow, R is the rotor radius.

4.2.3 Torque Co-efficient

The normal force is responsible for producing torque on the rotor shaft and this torque can be expressed for an element of the blade as $T_i = F_{ni} r_i$

Torque coefficient can be written as

$$C_{qi} = \frac{T_i}{\frac{1}{2}\rho U_0^2 R \frac{R}{2}} \tag{4.6}$$

Total drag coefficient and torque coefficient for an individual blade at a particular rotor angle, α are evaluated by integrating the coefficients over the blade surfaces. Then

$$C_{ni}(\propto = \sum_{i=1}^{i=12} C_{ni} \tag{4.7}$$

$$C_{ti}(\propto) = \sum_{i=1}^{i=12} C_{ti} \tag{4.8}$$

$$C_{qi} = \sum_{i=1}^{i=12} C_{qi} \tag{4.9}$$

CHAPTER-5

RESULTS AND DISCUSSIONS

CHAPTER 5

RESULTS AND DISCUSSIONS

5.1 Introduction

This chapter provides with the discussions of the results of experimental investigation conducted for the wind tunnel flow over the five bladed S-shaped Savonius rotor. The results of the pressure distribution over the convex and concave surface of the blade at different angle of rotation are analyzed first. Nature of the drag and torque characteristics are also analyzed in this chapter.

5.2 Aerodynamic Characteristics

This topic includes the analysis of pressure distribution over the surface of blade, drag coefficients and torque coefficient with respect to constant velocity for five bladed S-shaped Savonius rotor .

5.2.1 Pressure distribution

Air velocity has taken 13 m/s in this experiment for comparison to other existing results. The pressure distributions over the blades concave and convex surface were measured at 10^0 interval of rotor angle between 0^0 to 350^0. The results are presented in the Figures 5.1 to 5.36.

At rotor angle $\alpha = 0^0$ (Figure 5.1), pressure on the convex surface of the blade almost constant in the negative region from $\phi = 0^0$ to 25^0 which means maximum air flow separation occurs in this region, then pressure increases from negative to atmospheric region up to $\phi = 25^0$ to 50^0 that means air flow separation decreases with increase tapping angle. After that pressure remains approximately constant up to $\phi = 135^0$ which means small amount of air flow separation occurs in this area. Then pressure decreases slightly in the negative region up to $\phi = 180^0$ that means air flow separation increases in this region. Pressure coefficient on convex surface situated in the negative region means pressure on convex surface lower than atmospheric pressure at all tapping points. At rotor angle $\alpha = 0^0$ (Figure 5.1), pressure on the concave surface of the blade pressure remains constant negative value up to $\phi = 0^0$ to 80^0 that means small amount of air flow separation occurs in this region, then pressure more decreases in negative region up to $\phi = 100^0$ and maximum air flow separation occurs at $\phi =$

100^0. After that pressure increases in negative region up to $\phi = 135^0$ and approximately remains constant up to $\phi = 180^0$. Pressure coefficient on concave surface situated in the negative region means pressure on concave surface lower than atmospheric pressure.

At rotor angle $\alpha = 10^0$ (Figure 5.2), pressure on the convex surface of the blade increase in the negative region from $\phi = 0^0$ to 45^0, then pressure more decreases in the negative region up to $\phi= 60^0$, after that pressure increases from negative to positive values up to $\phi = 120^0$. Again, pressure decreases from positive to negative values up to $\phi = 165^0$ and remain constant negative values up to $\phi = 180^0$. At rotor angle $\alpha = 10^0$ (Figure 5.2), pressure on the concave surface of the blade increases in the negative region $\phi = 0^0$ to 15^0, then more decreases pressure in the negative region from $\phi = 15^0$ to 35^0. Again pressure increases in the negative region from $\phi = 35^0$ to 55^0, then decreases in the negative region from $\phi = 55^0$ to 100^0 and approximately remains constant values from $\phi = 100^0$ to 180^0.

At rotor angle $\alpha = 20^0$ (Figure 5.3), pressure on the convex surface of the blade increases from negative to positive values between $\phi = 0^0$ to 35^0, then pressure decreases to positive values from $\phi = 35^0$ to 55^0 , after that pressure remains constant positive up to $\phi = 110^0$. Then pressure increases in the positive region up to $\phi = 130^0$, again pressure decreases from positive to negative region up to $\phi = 160^0$ and approximately remains negative values up to $\phi = 180^0$. At rotor angle $\alpha = 20^0$ (Figure 5.3), pressure on the concave surface of the blade increases in the negative region from $\phi = 0^0$ to 15^0, then more decreases from $\phi = 15^0$ to 35^0, after that pressure remain constant in the negative region from $\phi = 35^0$ to 60^0, then decreases again in the negative region $\phi = 60^0$ to 105^0 and approximately constant negative values from $\phi = 105^0$ to 180^0.

At rotor angle $\alpha = 30^0$ (Figure 5.4), pressure on the convex surface of the blade decreases up to $\phi = 0^0$ to 20^0, then pressure rises to positive values up to $\phi = 20^0$ to 30^0. Again pressure decreases to positives values up to $\phi = 55^0$, then remains constant up to $\phi = 105^0$ and pressure decreases to positive up to $\phi = 180^0$. Pressure coefficient on convex surface situated in the positive region means pressure on convex surface higher than atmospheric pressure at all tapping points. At rotor angle $\alpha = 30^0$ (Figure 5.4), pressure on the concave surface of the blade increases from $\phi = 0^0$ to 15^0, then again decreases pressure in the negative region from $\phi = 15^0$ to 40^0, then pressure increases in the negative region from $\phi = 40^0$ to 60^0 and more decreases pressure in negative region between $\phi = 60^0$ to 165^0. After that, pressure increases up to 180^0.

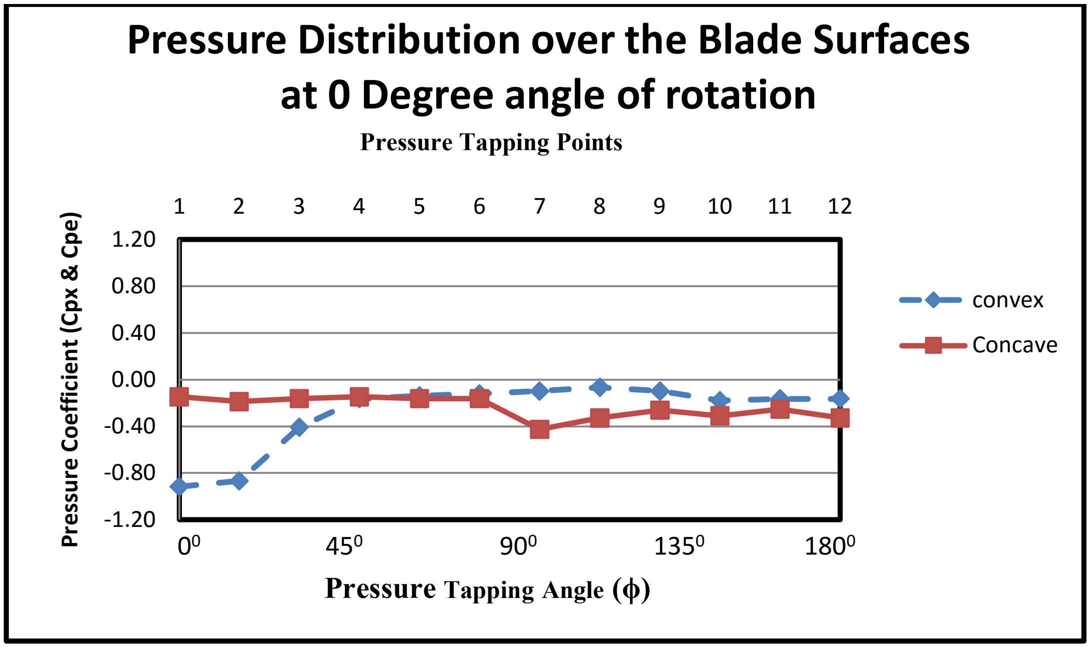

Figure 5.1 Pressure Distribution over the blade surfaces at 0 Degree angle of rotation

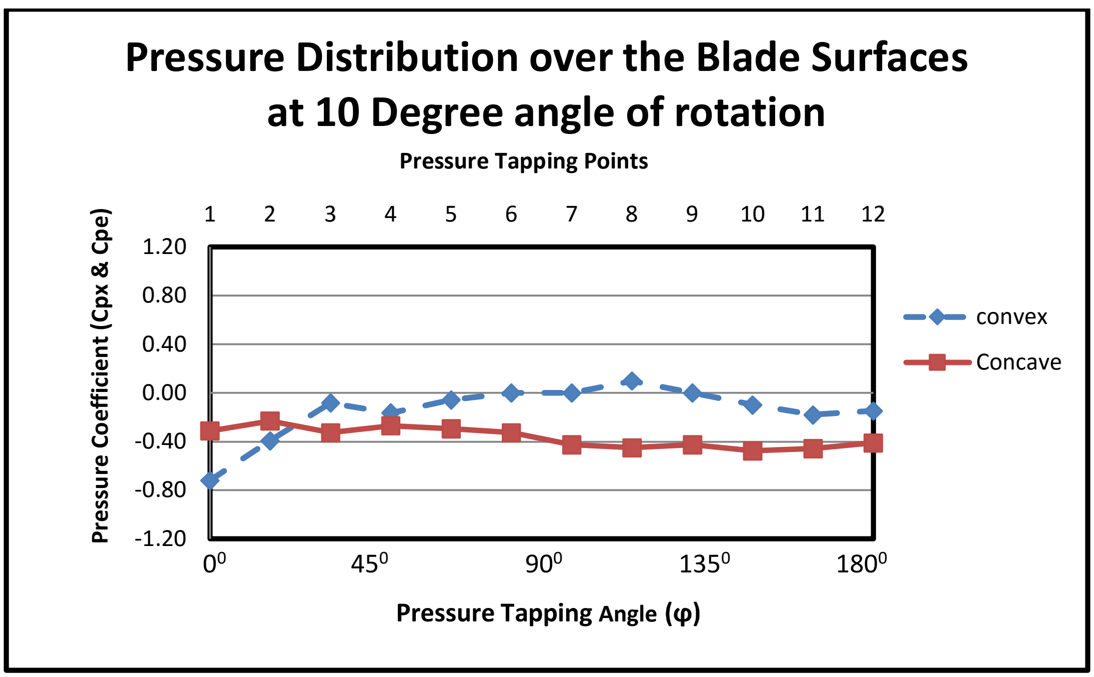

Figure 5.2 Pressure Distribution over the blade surfaces at 10 Degree angle of rotation

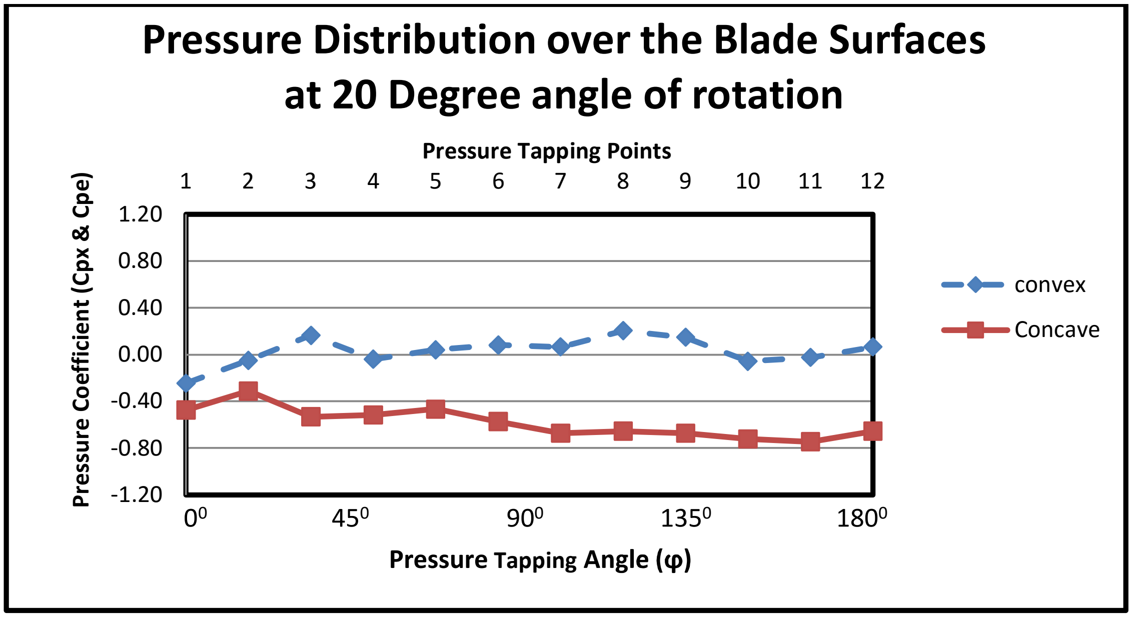

Figure 5.3 Pressure Distribution over the blade surfaces at 20 Degree angle of rotation

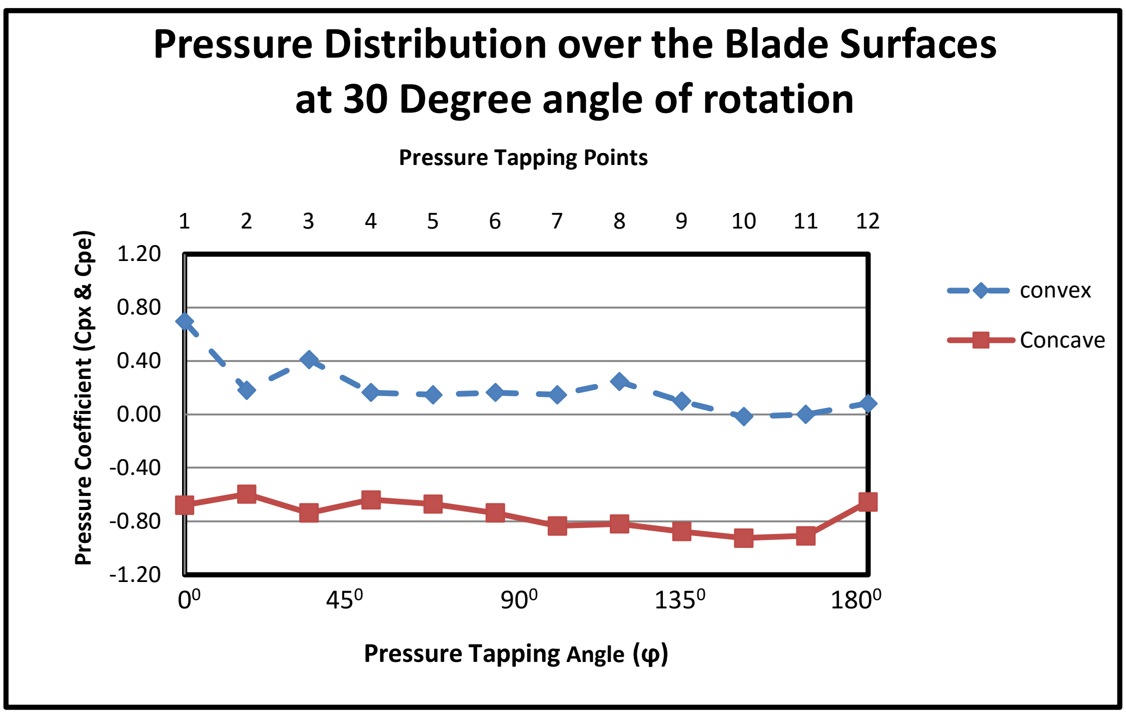

Figure 5.4 Pressure Distribution over the blade surfaces at 30 Degree angle of rotation

At rotor angle $\alpha = 40^0$ (Figure 5.5), pressure on the convex surface of the blade decreases up to $\phi = 0^0$ to 50^0, then pressure increases to positive values up to $\phi = 50^0$ to 60^0. Again pressure decreases to positives values up to $\phi = 105^0$, then approximately remains constant up to $\phi = 115^0$. After that pressure decreases to positive to $\phi = 140^0$ and remains constant up to =180^0. At rotor angle $\alpha = 40^0$ (Figure 5.5), pressure on the concave surface of the blade decreases in the negative region between $\phi = 0^0$ to 50^0, then increases pressure in the negative region from $\phi = 50^0$ to 60^0, again decreases pressure in the negative region from $\phi = 60^0$ to 95^0, then pressure almost remains constant in the negative region between $\phi = 95^0$ to 140^0 and then increases from $\phi = 140^0$ to 180^0.

At rotor angle $\alpha = 50^0$ (Figure 5.6), pressure on the convex surface of the blade slightly decreases from $\phi = 0^0$ to 65^0, then rises to positive values up to $\phi = 65^0$ to 80^0. Again, pressure decreases up to $\phi = 100^0$, then pressure increases to positive values from $\phi = 100^0$ to 115^0. After that pressure decreases up to 150^0 and remains constant up to $\phi = 180^0$. At rotor angle $\alpha = 50^0$ (Figure 5.6), pressure on the concave surface of the blade remains constant from $\phi = 0^0$ to 50^0, then decreases in negative region from $\phi = 50^0$ to 110^0. Then almost remains constant in negative region from $\phi = 110^0$ to 130^0. Next, pressure increases in negative region from $\phi = 130^0$ to 180^0.

At rotor angle $\alpha = 60^0$ (Figure 5.7), pressure on the convex surface of the blade slightly decreases from $\phi = 0^0$ to 65^0, then slightly increases to positive values from $\phi = 65^0$ to 80^0. Again pressure decreases to positives values up to $\phi = 90^0$, then pressure increases to positive values up to $\phi = 90^0$ to 115^0. The positive pressure almost remains constant up to $\phi = 180^0$. At rotor angle $\alpha = 60^0$ (Figure 5.7), pressure on the concave surface decreases from $\phi = 0^0$ to 30^0, then remain constant in negative region from $\phi = 30^0$ to 70^0. Again pressure decreases to negative values up to $\phi = 90^0$, then remain constant in negative region from $\phi = 90^0$ to 145^0. Then the pressure increases in negative region from $\phi = 145^0$ to 180^0.

At rotor angle $\alpha = 70^0$ (Figure 5.8), pressure on the convex surface of the blade decreases up to $\phi = 0^0$ to 55^0, then pressure increases to positive value up to $\phi = 55^0$ to 85^0. Again pressure decreases to positives values up to $\phi = 100^0$, then pressure increases to positive values up to $\phi = 100^0$ to 115^0, then almost constant positive pressure up to $\phi = 180^0$. At rotor angle $\alpha = 70^0$ (Figure 5.8), pressure on the concave surface of the blade decreases up to $\phi = 0^0$ to 20^0, then almost remains constant from 20^0 to 55^0. After that, pressure decreases to negative values up

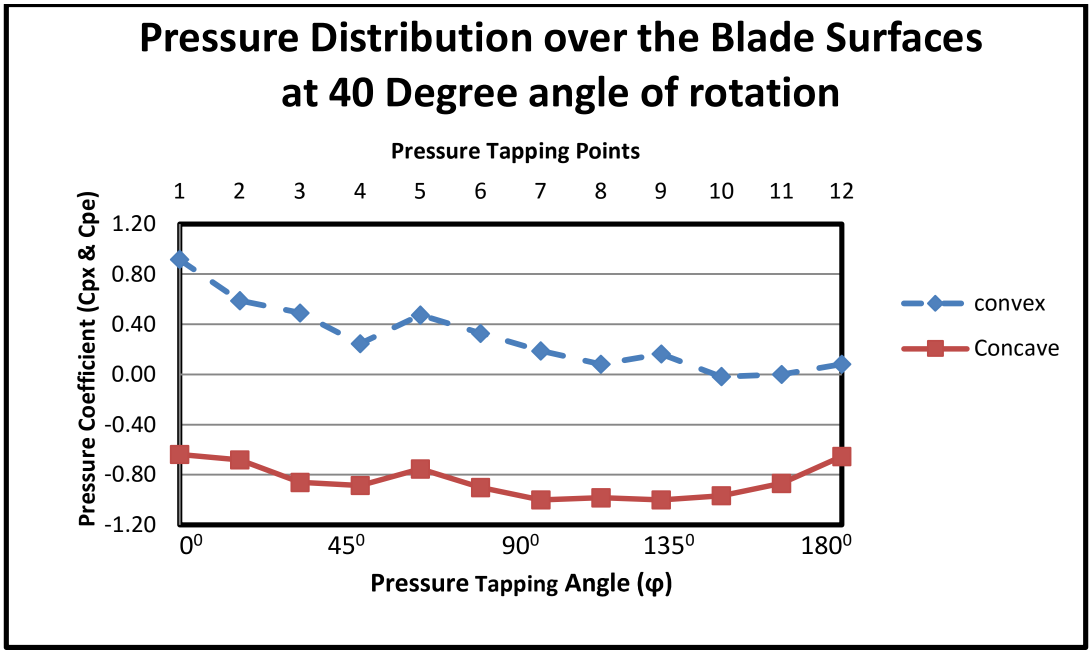

Figure 5.5 Pressure Distribution over the blade surfaces at 40 Degree angle of rotation

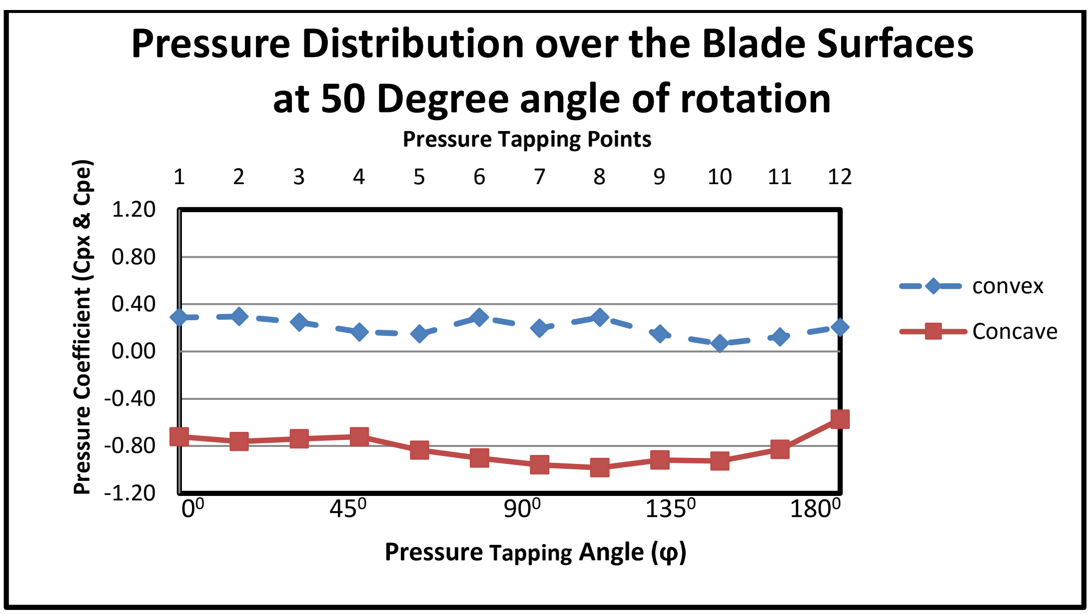

Figure 5.6 Pressure Distribution over the blade surfaces at 50 Degree angle of rotation

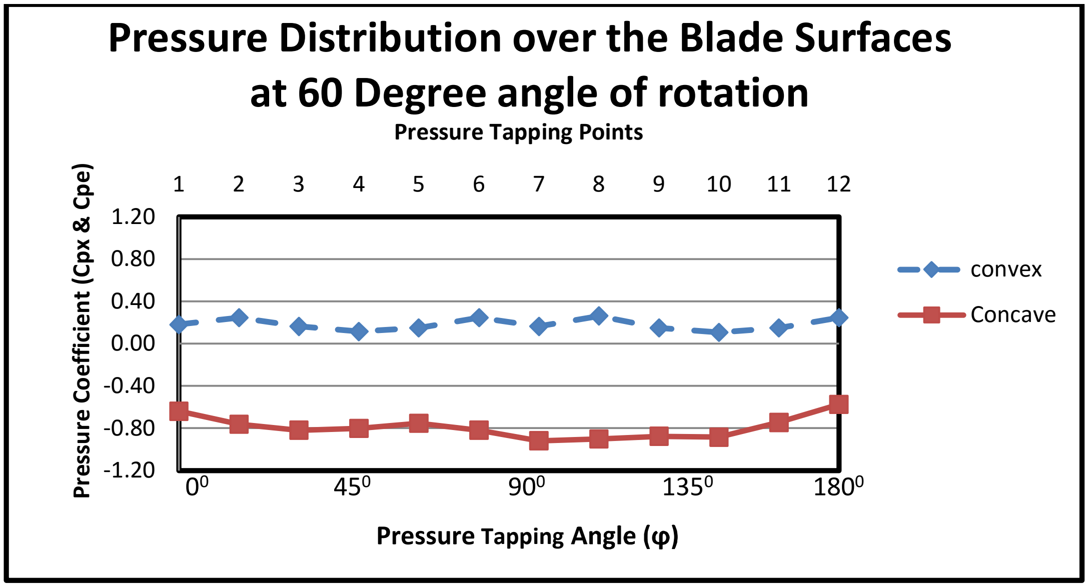

Figure 5.7 Pressure Distribution over the blade surfaces at 60 Degree angle of rotation

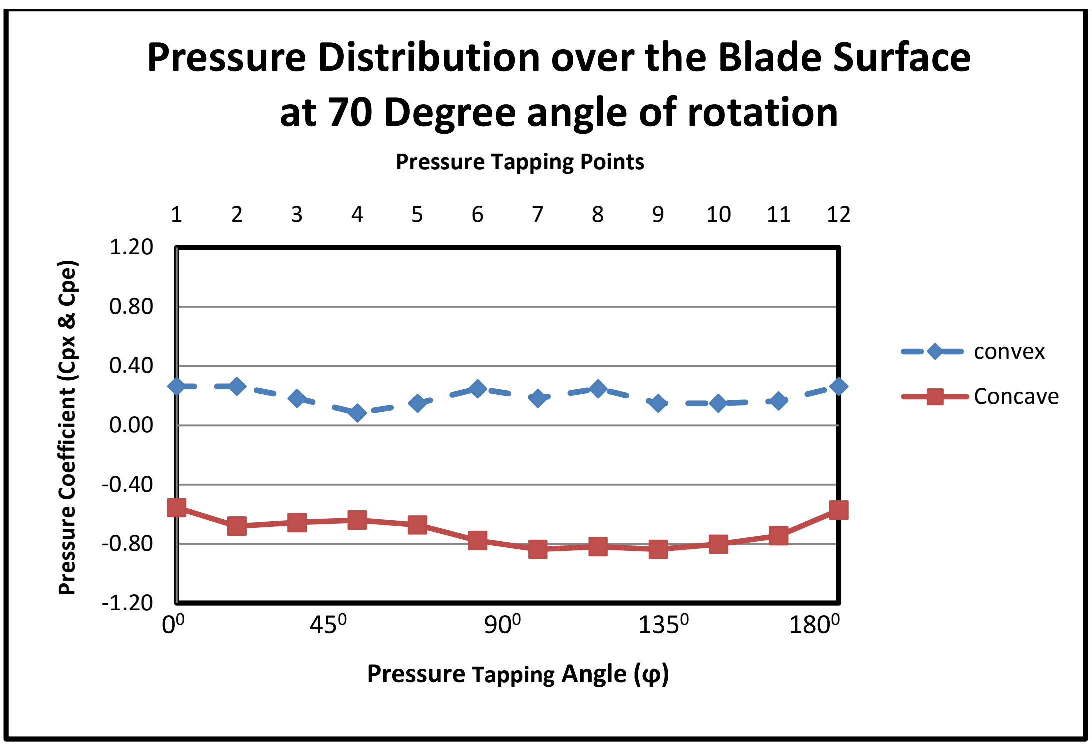

Figure 5.8 Pressure Distribution over the blade surfaces at 70 Degree angle of rotation

to $\phi = 100^0$, then remain constant in negative region from $\phi = 100^0$ to 150^0, then again increases pressure in negative region from $\phi = 150^0$ to 180^0.
At rotor angle $\alpha = 80^0$ (Figure 5.9), pressure on the convex surface of the blade decreases from $\phi = 0^0$ to 50^0, then increases to positive values from to $\phi = 50^0$ to 80^0. Next the positive pressure remains constant up to $\phi= 180^0$. At rotor angle $\alpha = 80^0$ (Figure 5.9), pressure on the concave surface of the blade decreases from $\phi = 0^0$ to 15^0, then remains almost constant in the negative region from $\phi = 15^0$ to 70^0. Again, pressure decreases to negative values up to $\phi = 90^0$. After that increases in the negative region between $\phi = 90^0$ to 110^0. Again more decreases negative values up to $\phi = 150^0$ and then increases sharply in the negative region between $\phi = 150^0$ to 180^0.

At rotor angle $\alpha = 90^0$ (Figure 5.10), on the convex surface of the blade pressure remains almost constant positive from $\phi = 0^0$ to 180^0. At rotor angle $\alpha = 90^0$ (Figure 5.10), pressure on the concave surface of the blade decreases up to $\phi = 0^0$ to 15^0, then increases up to 35^0. Again, pressure decreases up to 70^0 and approximately remains constant in the negative region from $\phi = 70^0$ to 110^0. After that, increases pressure in the negative region from $\phi = 110^0$ to 180^0.

At rotor angle $\alpha = 100^0$ (Figure 5.11), pressure on the convex surface of the blade decreases from $\phi = 0^0$ to 50^0, then increases values from $\phi = 50^0$ to 80^0. Again, decreases to positive values up to $\phi = 90^0$ and then pressure increases to positive values from $\phi = 90^0$ to 135^0. Then the positive pressure remains constant up to $\phi = 180^0$. At rotor angle $\alpha = 100^0$ (Figure 5.11), pressure on the concave surface of the blade decreases from $\phi = 0^0$ to 15^0, then increases pressure in the negative region from $\phi = 15^0$ to 30^0. After that, decreases to negative values up to $\phi = 60^0$, then again increases pressure in the negative the region between $\phi = 60^0$ to 165^0 and then negative pressure remain constant up to $\phi = 180^0$.

At rotor angle $\alpha = 110^0$ (Figure 5.12), pressure on the convex surface of the blade decreases from $= 0^0$ to 55^0, then pressure increases to positive values up to $\phi = 55^0$ to 85^0. Again, pressure decreases to positives values up to $\phi = 95^0$ and then pressure increases to positive values from $\phi = 95^0$ to 105^0. Next almost constant positive pressure up to $\phi = 180^0$. At rotor angle $\alpha = 110^0$ (Figure 5.12), pressure on the concave surface of the blade decreases to positive to negative region between $\phi = 0^0$ to 15^0, then increases pressure to negative from ϕ

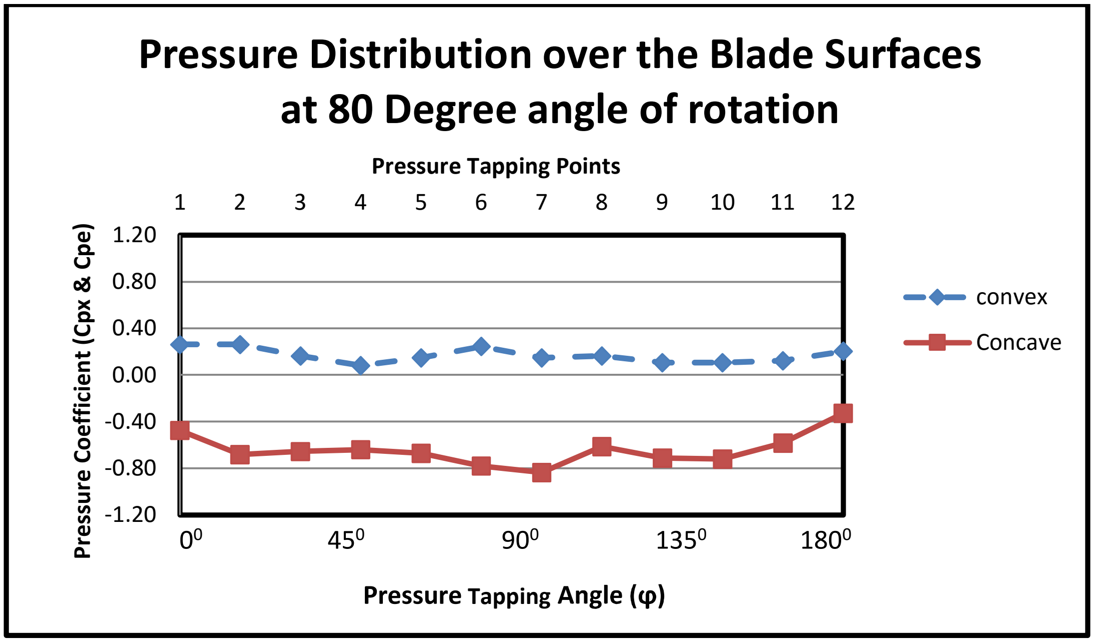

Figure 5.9 Pressure Distribution over the blade surfaces at 80 Degree angle of rotation

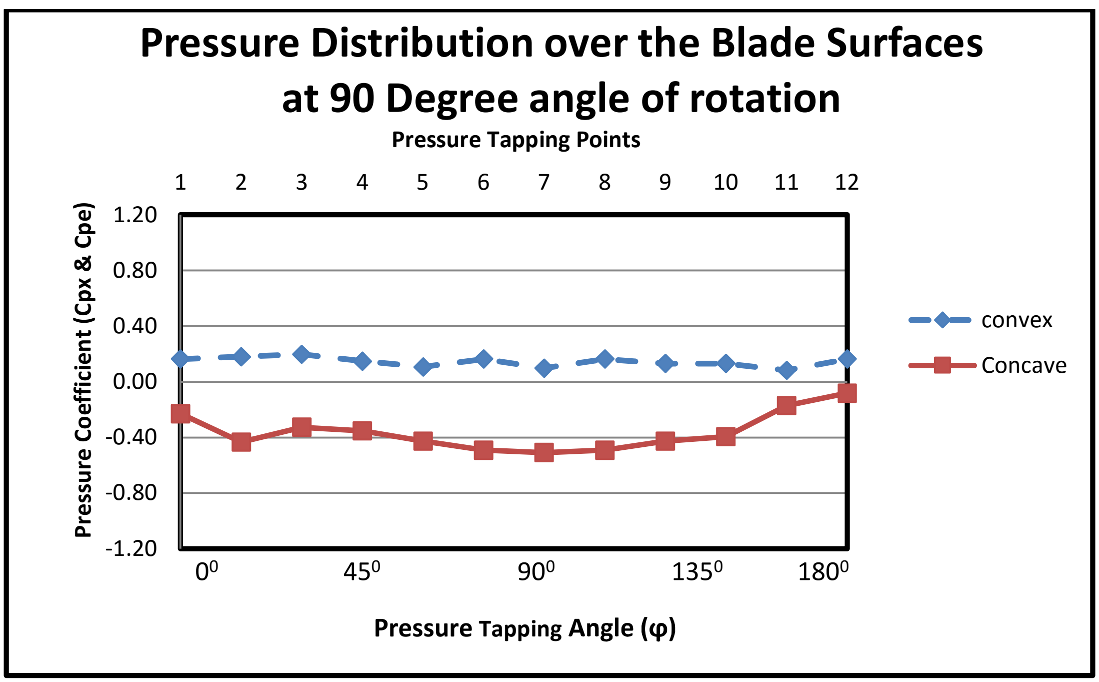

Figure 5.10 Pressure Distribution over the blade surfaces at 90 Degree angle of rotation.

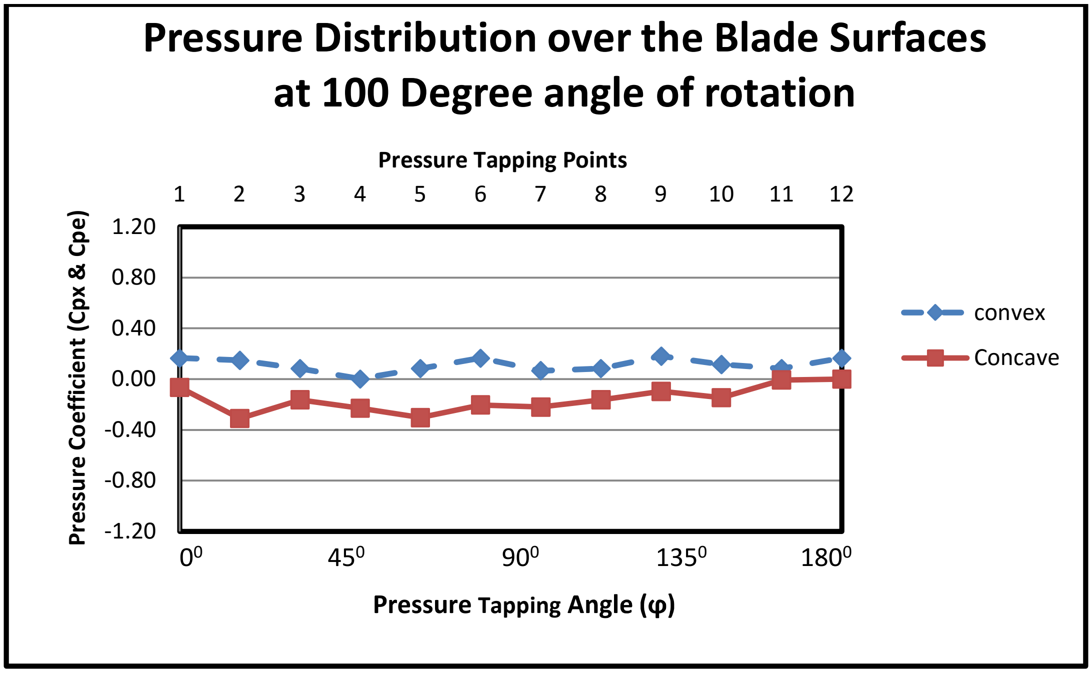

Figure 5.11 Pressure Distribution over the blade surfaces at 100 Degree angle of rotation

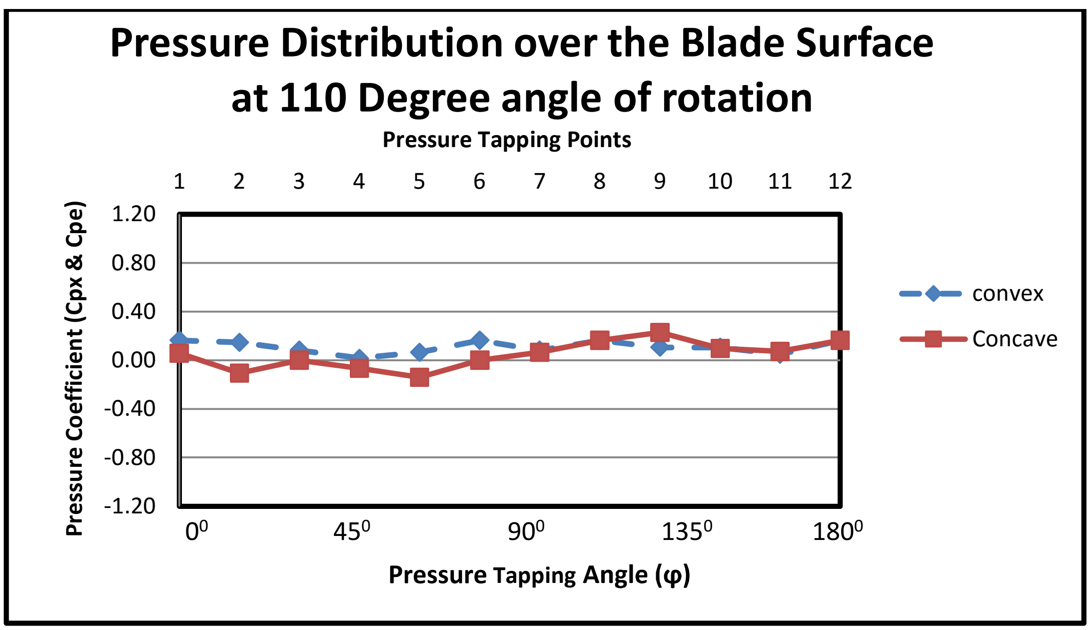

Figure 5.12 Pressure Distribution over the blade surface at 110 Degree angle of rotation

= 15^0 to 30^0. Again, pressure decreases to negative values up to $\phi = 60^0$, then increases negative to positive region from $\phi = 60^0$ to 135^0. After that, pressure decreases to positive values up to $\phi = 145^0$ and then almost remains constant positive up to $\phi = 180^0$.

At rotor angle $\alpha = 120^0$ (Figure 5.13), pressure on the convex surface of the blade approximately constant from = 0^0 to 60^0, then increases to positive values from $\phi = 60^0$ to 80^0. After that, decreases from positive to negative region between $\phi = 80^0$ to 165^0 and then pressure rises from negative to positive region up to $\phi = 180^0$. At rotor angle $\alpha = 120^0$ (Figure 5.13), pressure on the concave surface of the blade decreases positive values from $\phi = 0^0$ to 20^0, then pressure increases to positive from $\phi = 20^0$ to 130^0. Again, pressure decreases to positive values from $\phi = 130^0$ to 145^0 and next almost constant positive up to $\phi = 180^0$.

At rotor angle $\alpha = 130^0$ (Figure 5.14), pressure on the convex surface of the blade approximately constant positive pressure up to $\phi = 50^0$, then pressure increases from $\phi = 50^0$ to 80^0. Again, pressure decreases positive values from $\phi = 90^0$ to 135^0. The positive pressure remains constant up to $\phi = 180^0$. At rotor angle $\alpha = 130^0$ (Figure 5.14), pressure on the concave surface of the blade almost constant positive pressure up to $\phi = 100^0$. Then pressure rises to positive values between $\phi = 100^0$ to 130^0. After that, pressure decreases positive values from $\phi = 130^0$ to 150^0, next constant pressure up to $\phi = 180^0$.

At rotor angle $\alpha = 140^0$ (Figure 5.15), pressure on the convex surface of the blade almost constant positive pressure up to $\phi = 45^0$, then rises to positive from to $\phi = 45^0$ to 85^0. After that, constant positive pressure up to $\phi = 125^0$ and then pressure decreases positive values up to $\phi = 125^0$ to 135^0. Then the positive pressure remains almost constant up to $\phi = 180^0$. At rotor angle $\alpha = 140^0$ (Figure 5.15), pressure on the concave surface of the blade approximately constant positive up to $\phi = 70^0$. Then pressure increases to positive from $\phi = 70^0$ to 85^0. Next positive pressure remain constant up to $\phi = 180^0$.

At rotor angle $\alpha = 150^0$ (Figure 5.16), pressure on the convex surface of the blade constant positive pressure up to $\phi = 45^0$, then pressure increases from $\phi = 45^0$ to 80^0. Again, constant positive pressure up to $\phi = 120^0$, next decreases to positive values from $\phi = 120^0$ to 135^0, then constant positive pressure up to $\phi = 180^0$. At rotor angle $\alpha = 150^0$ (Figure 5.16), pressure on the concave surface of the blade approximately constant positive pressure up to $\phi = 60^0$. Then pressure rises to positive from to $\phi = 60^0$ to 85^0. Again, positive pressure remains constant up to $\phi = 180^0$.

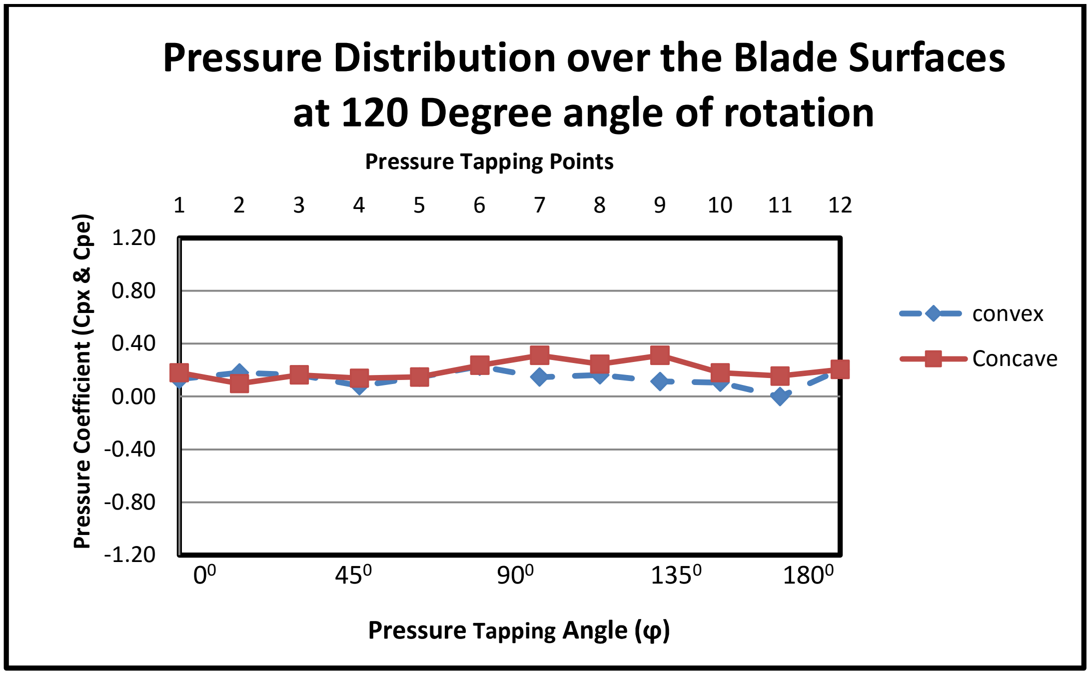

Figure 5.13 Pressure Distribution over the blade surfaces at 120 Degree angle of rotation

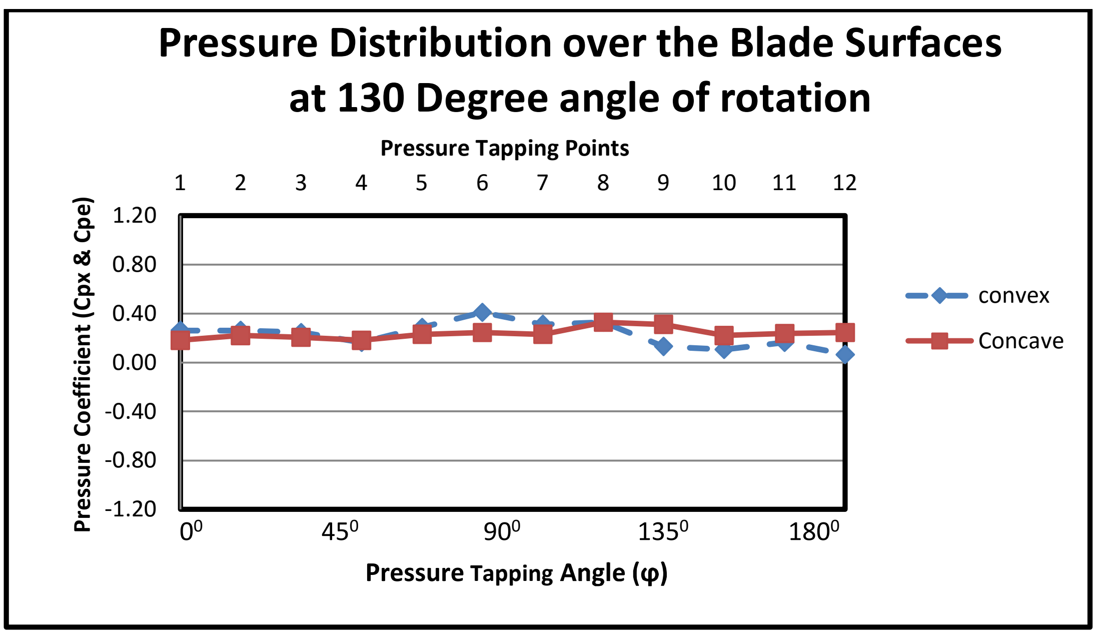

Figure 5.14 Pressure Distribution over the blade surfaces at 130 Degree angle of rotation

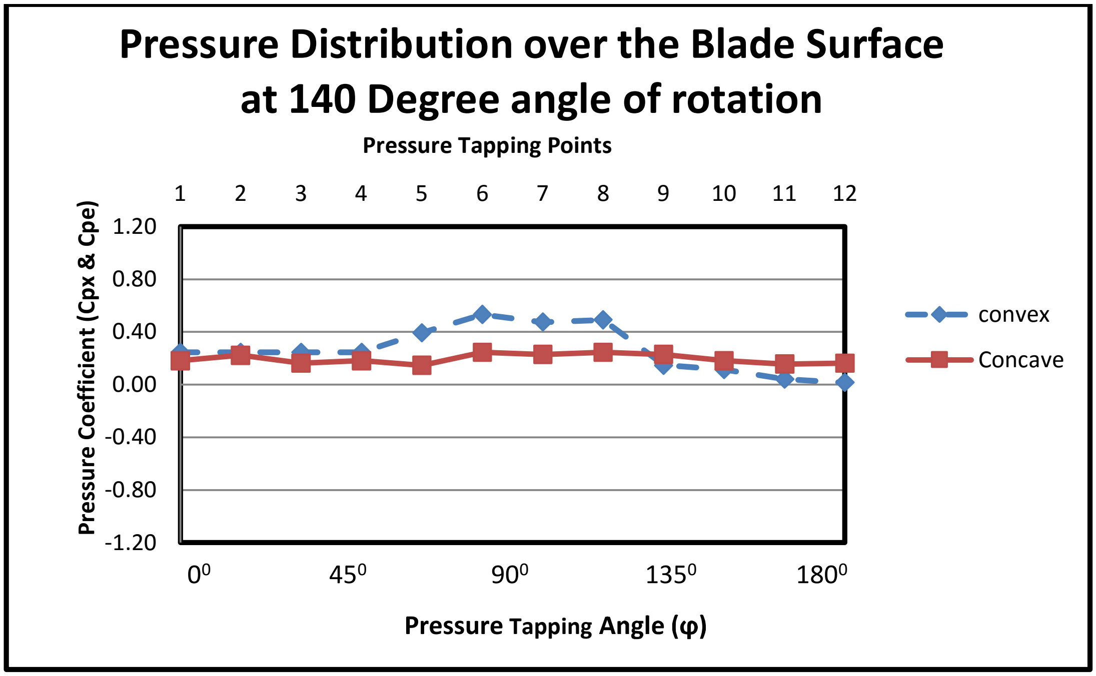

Figure 5.15 Pressure Distribution over the blade surfaces at 140 Degree angle of rotation

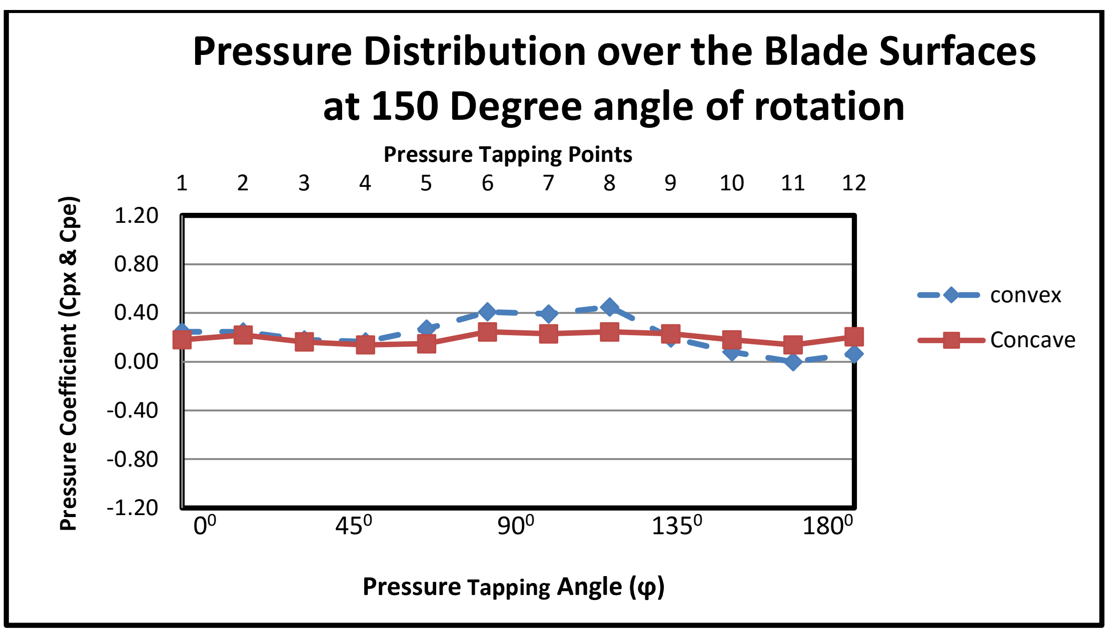

Figure 5.16 Pressure Distribution over the blade surfaces at 150 Degree angle of rotation

At rotor angle α = 160^0 (Figure 5.17), pressure on the convex surface of the blade approximately constant positive pressure up to ϕ = 50^0, then more rises positive values from ϕ = 50^0 to 85^0. Again, constant positive up to ϕ = 120^0. After that decreases to positive values up to ϕ= 120^0 to 165^0 and then positive pressure increases up to ϕ = 180^0. At rotor angle α = 160^0 (Figure 5.17), pressure on the concave surface of the blade approximately constant positive pressure up to ϕ = 165^0. Then increases to positive values up to ϕ = 165^0 to 180^0.

At rotor angle α = 170^0 (Figure 5.18), pressure on the convex surface of the blade approximately constant positive pressure up to ϕ = 50^0, then pressure increases to positive up to ϕ = 50^0 to 90^0. Next, constant positive pressure up to ϕ = 120^0, then pressure decreases positive values up to ϕ = 120^0 to 165^0 and again constant positive up to ϕ = 180^0. At rotor angle α = 170^0 (Figure 5.18), pressure on the concave surface of the blade approximately remains constant positive up to ϕ = 170^0. Then pressure rises to positive values from ϕ = 170^0 to 180^0.

At rotor angle α = 180^0 (Figure 5.19), pressure on the convex surface of the blade almost constant positive pressure up to ϕ = 60^0, then sharply increases positive values from ϕ = 60^0 to 125^0. After that, more decreases to positive values from ϕ = 125^0 to 135^0 and then remain constant positive pressure up to ϕ = 160^0. Again pressure increases from positive to negative region up to ϕ = 180^0. At rotor angle α = 180^0 (Figure 5.19), pressure on the concave surface of the blade approximately constant positive pressure up to ϕ = 180^0.

At rotor angle α = 190^0 (Figure 5.20), pressure on the convex surface of the blade approximately constant positive pressure up to ϕ = 60^0, then increases to positive from ϕ = 60^0 to 125^0. Again pressure sharply decreases from positive to negative region up to ϕ = 180^0. At rotor angle α = 190^0 (Figure 5.20), pressure on the concave surface of the blade approximately constant positive pressure up to ϕ = 170^0. Then pressure more increases positive values from ϕ = 170^0 to 180^0.

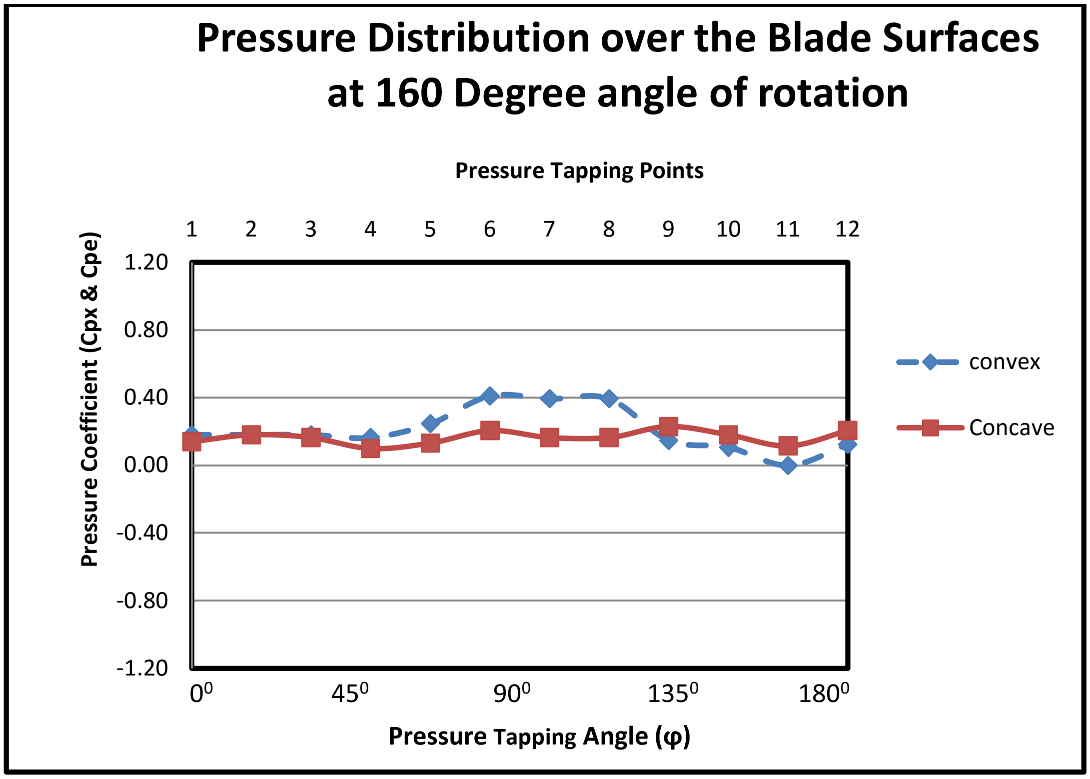

Figure 5.17 Pressure Distribution over the blade surfaces at 160 Degree angle of rotation

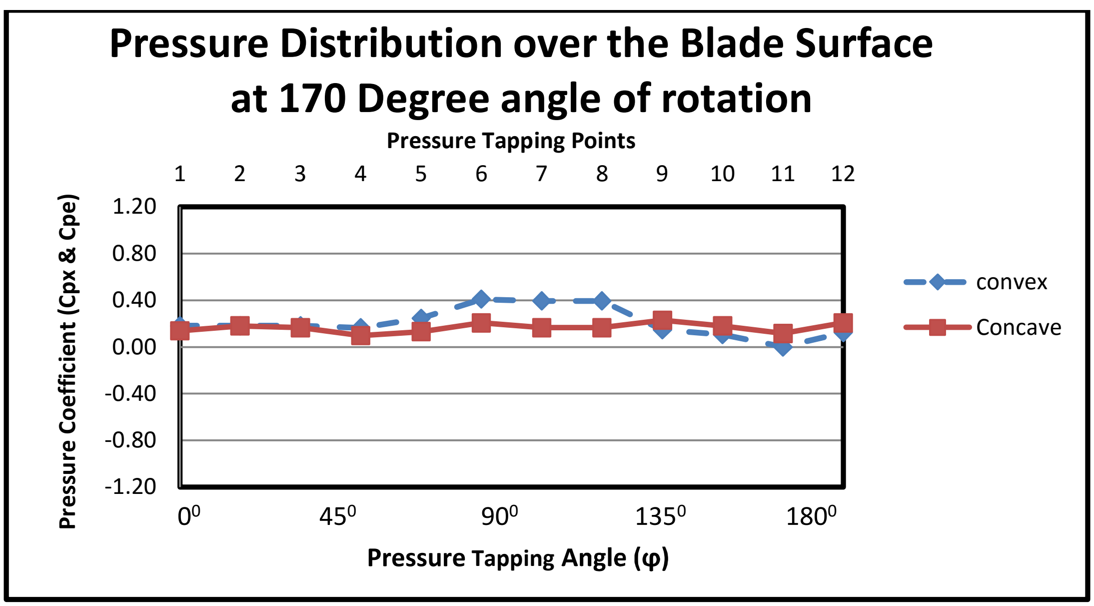

Figure 5.18 Pressure Distribution over the blade surface at 170 Degree angle of rotation

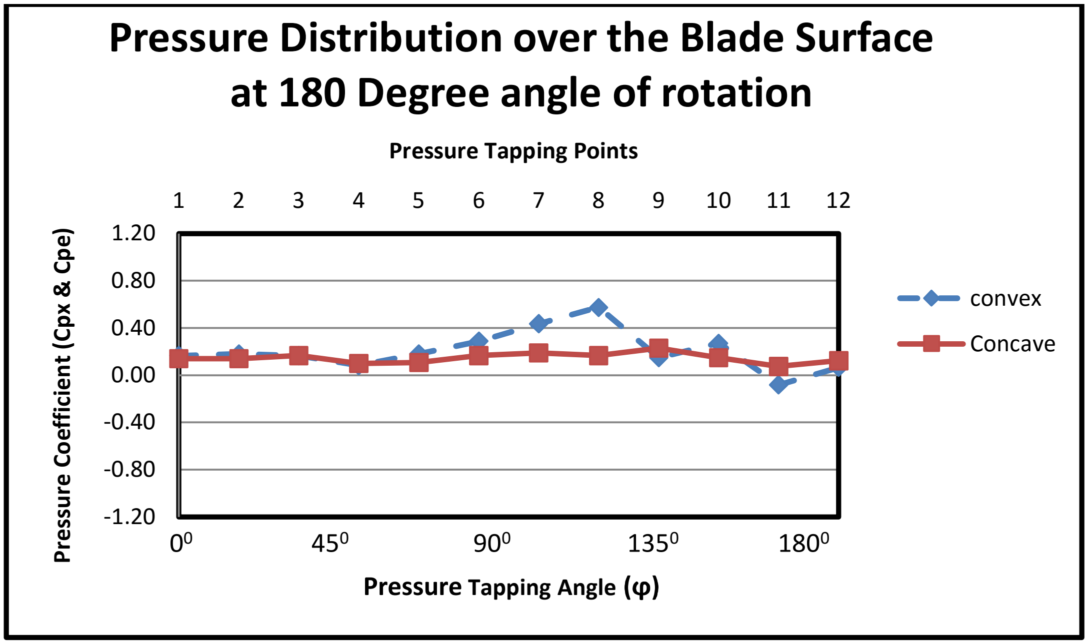

Figure 5.19 Pressure Distribution over the blade surfaces at 180 Degree angle of rotation

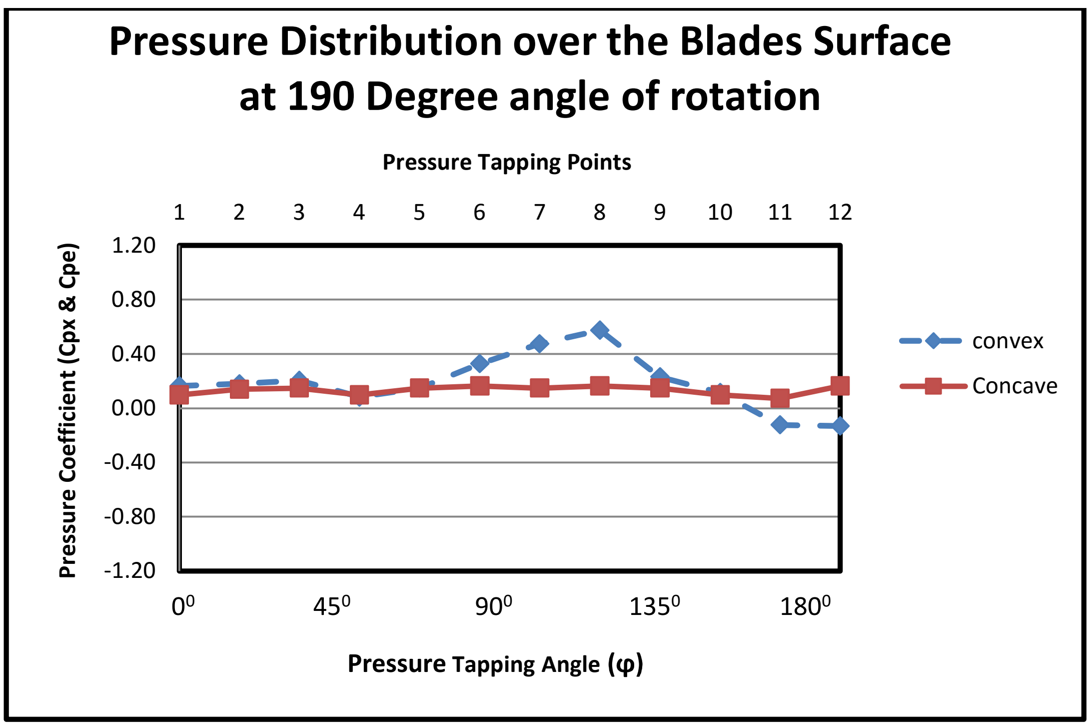

Figure 5.20 Pressure Distribution over the blade surfaces at 190 Degree angle of rotation

At rotor angle $\alpha = 200^0$ (Figure 5.21), pressure on the convex surface of the blade approximately constant positive up to $\phi = 65^0$, then sharply increases to positive values from $\phi = 65^0$ to 120^0 and pressure sharply decreases from positive to negative region up to $\phi = 180^0$. At rotor angle $\alpha = 200^0$ (Figure 5.21), pressure on the concave surface of the blade almost remains constant positive values up to $\phi = 180^0$.

At rotor angle $\alpha = 210^0$ (Figure 5.22), pressure on the convex surface of the blade remains constant positive pressure up to $\phi =70^0$, then more increases to positive from $\phi = 70^0$ to 120^0. After that, sharply decreases from positive to negative region up to $\phi = 180^0$. At rotor angle $\alpha = 210^0$ (Figure 5.22), pressure on the concave surface of the blade approximately constant positive pressure up to $\phi = 80^0$, then more rises to positive values up to $\phi = 125^0$. Next, the positive pressure remains constant up to $\phi = 180^0$.

At rotor angle $\alpha = 220^0$ (Figure 5.23), pressure on the convex surface of the blade almost remains constant positive pressure up to $\phi = 45^0$, then more increases to positive values from $\phi = 45^0$ to 125^0. After that, sharply decreases from positive to negative region up to $\phi = 180^0$. At rotor angle $\alpha = 220^0$ (Figure 5.23), pressure on the concave surface of the blade approximately remains constant positive pressure up to $\phi = 120^0$, then more increases to positive values up to $\phi = 135^0$. After that pressure decreases up to 145^0 and again constant positive values up to $\phi = 180^0$.

At rotor angle $\alpha = 230^0$ (Figure 5.24), pressure on the convex surface of the blade approximately remains constant positive pressure up to $\phi = 40^0$, then more increases to positive from $\phi = 40^0$ to 120^0. Next, sharply decreases from positive to negative region up to $\phi = 180^0$. At rotor angle $\alpha = 230^0$ (Figure 5.24), pressure on the concave surface of the blade approximately remains constant positive pressure up to $\phi = 70^0$, then slightly increases to positive values up to $\phi = 90^0$. After that, pressure almost remains constant up to 135^0, then slightly decreases to positive values up to $\phi = 160^0$ and again remains constant positive up to $\phi = 180^0$.

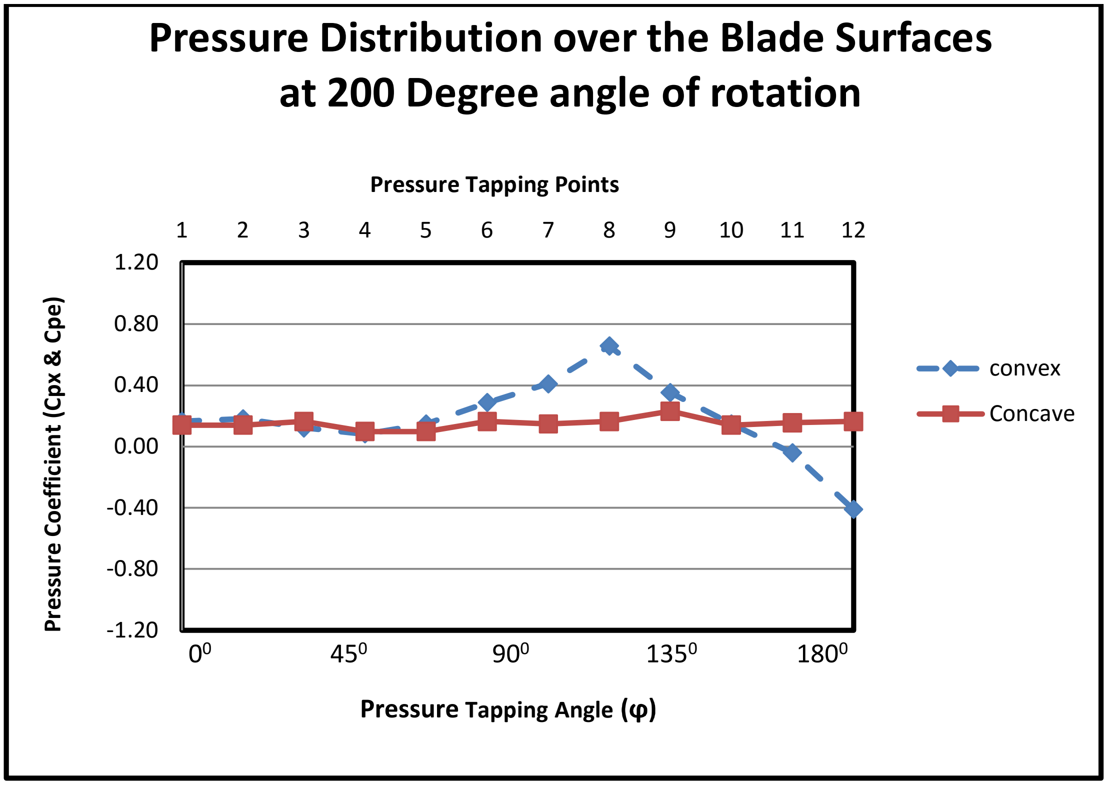

Figure 5.21 Pressure Distribution over the blade surface at 200 Degree angle of rotation

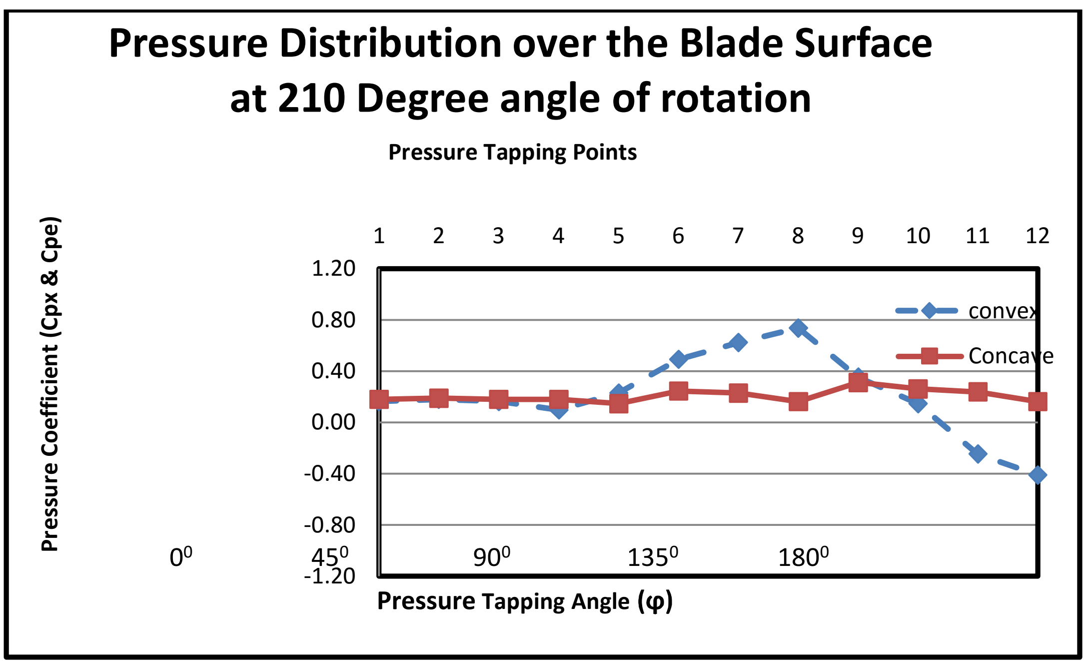

Figure 5.22 Pressure Distribution over the blade surface at 210 Degree angle of rotation

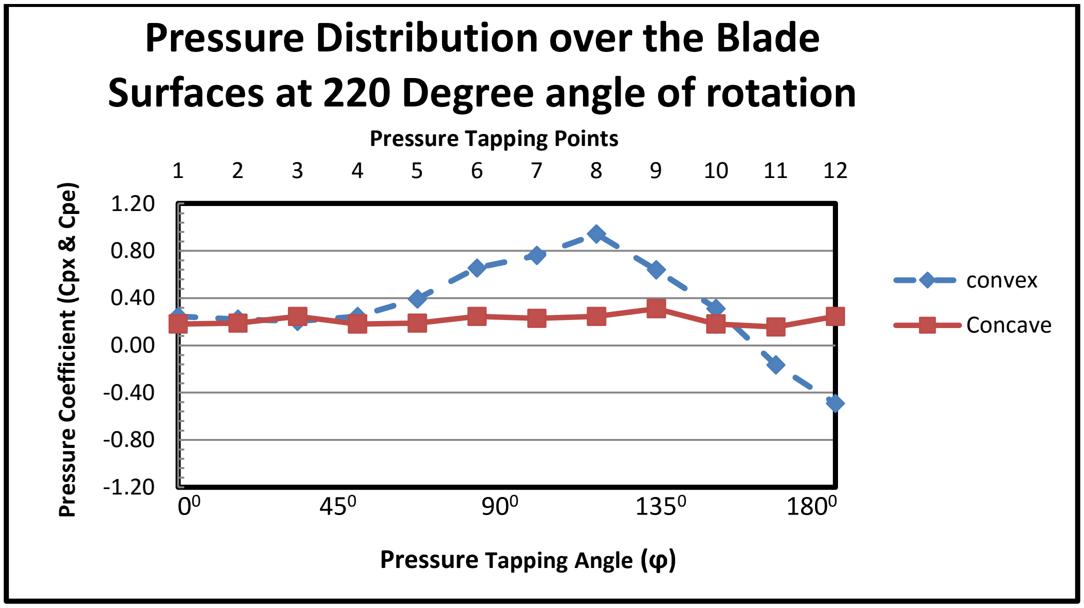

Figure 5.23 Pressure Distribution over the blade surfaces at 220 Degree angle of rotation

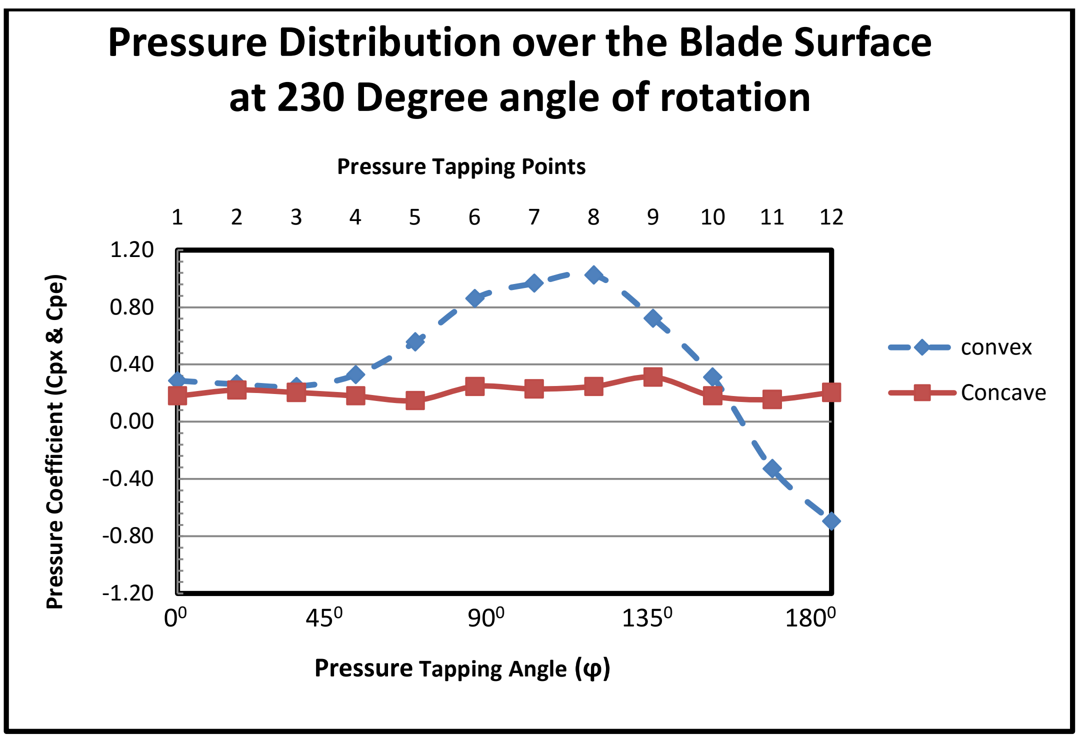

Figure 5.24 Pressure Distribution over the blade surface at 230 Degree angle of rotation

At rotor angle α = 240^0 (Figure 5.25), pressure on the convex surface of the blade approximately remains constant positive pressure up to ϕ = 15^0, then sharply rises to positive values from ϕ = 15^0 to 120^0. After that, sharply decreases from positive to negative region up to ϕ = 180^0. At rotor angle α = 240^0 (Figure 5.25), pressure on the concave surface of the blade almost remain stagnant pressure up to ϕ = 60^0, then pressure slightly increases to positive values up to ϕ = 90^0. The positive pressure remains constant values up to ϕ = 180^0.

At rotor angle α = 250^0 (Figure 5.26), pressure on the convex surface of the blade sharply increases up to ϕ = 50^0, then pressure more decreases to positive from ϕ = 50^0 to 80^0. Again, pressure gradually increases positive values up to ϕ = 130^0. After that, sharply decreases from positive to negative region up to ϕ = 180^0. At rotor angle α = 250^0 (Figure 5.26), pressure on the concave surface of the blade almost constant positive pressure up to ϕ = 50^0, then more rises positive values up to ϕ = 75^0. After that, constant positive pressure up to ϕ = 130^0 and then more decreases to positive values up to ϕ = $160^{0.}$ Next, the positive pressure remain constant up to ϕ = 180^0.

At rotor angle α = 260^0 (Figure 5.27), pressure on the convex surface of the blade sharply increases positive values up to ϕ = 50^0, then pressure sharply decreases from positive to negative region up to ϕ = 50^0 to 120^0. Again pressure gradually rises to positive values up to ϕ = 135^0 and remains constant up to ϕ = 160^0, then pressure sharply decreases from positive to negative region up to ϕ = 180^0. At rotor angle α = 260^0 (Figure 5.27), pressure on the concave surface of the blade approximately constant positive pressure up to ϕ = 70^0, then more rises positive values up to ϕ = 135^0. After that, pressure slightly decreases up to ϕ = 160^0 and again increases pressure up to ϕ = 180^0.

At rotor angle α = 270^0 (Figure 5.28), pressure on the convex surface of the blade sharply increases to positive values up to ϕ = 30^0, then decreases from positive to negative region from ϕ = 30^0 to 90^0. Next, pressure gradually rises to positive values up to ϕ = 145^0 and remains constant positive pressure up to ϕ =180^0. At rotor angle α = 270^0 (Figure 5.28), pressure on the concave surface of the blade almost remains constant positive pressure up to ϕ = 60^0, then slightly rises values up to ϕ = 130^0. After that, pressure slightly decreases up to ϕ = 165^0 and constant positive values up to ϕ = 180^0.

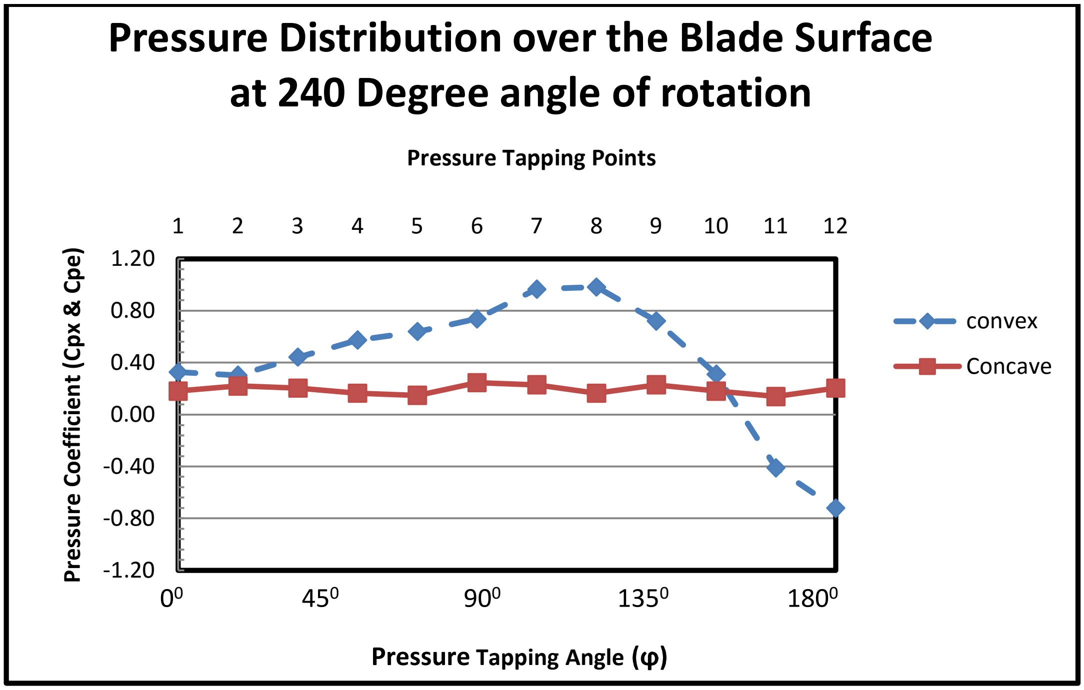

Figure 5.25 Pressure Distribution over the blade surface at 240 Degree angle of rotation

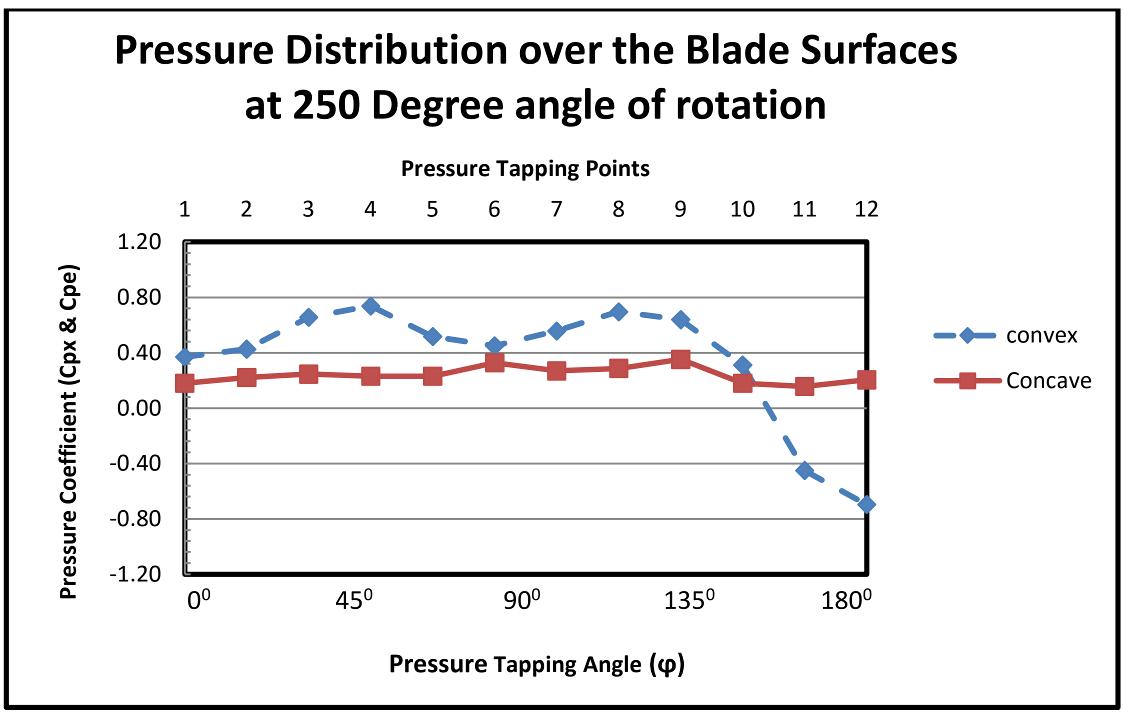

Figure 5.26 Pressure Distribution over the blade surface at 250 Degree angle of rotation

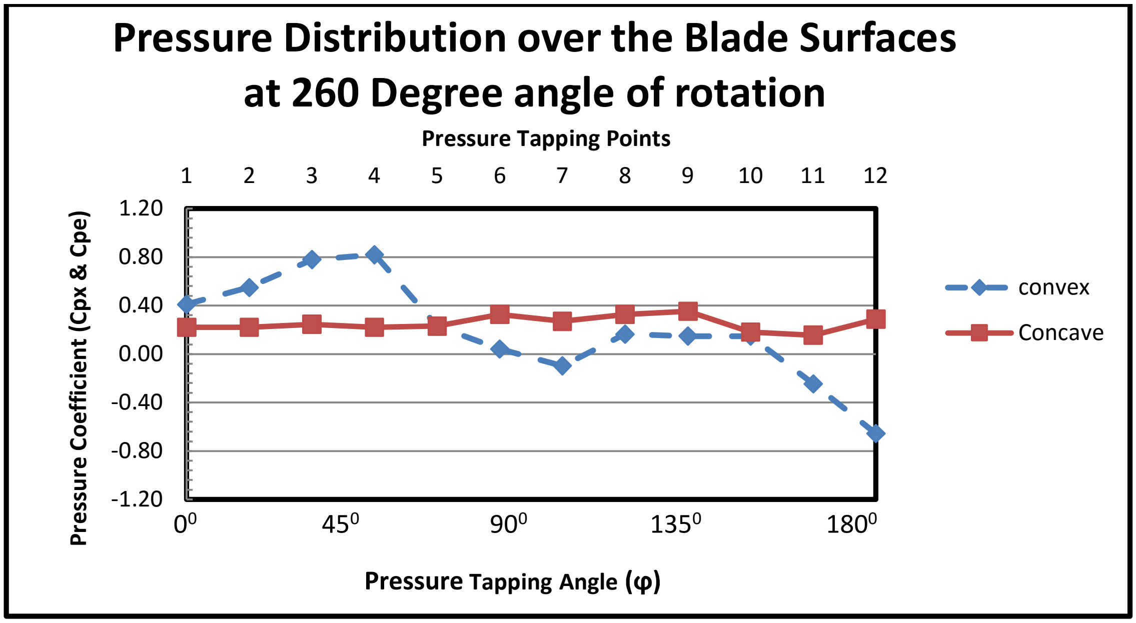

Figure 5.27 Pressure Distribution over the blade surfaces at 260 Degree angle of rotation

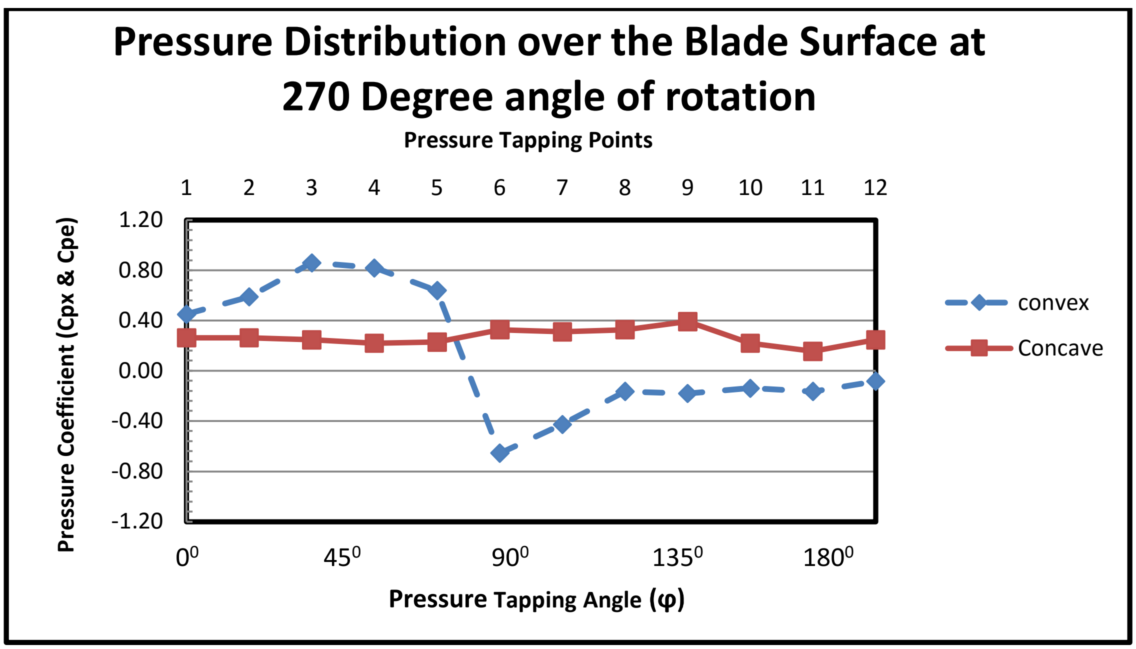

Figure 5.28 Pressure Distribution over the blade surface at 270 Degree angle of rotation

At rotor angle $\alpha = 280^0$ (Figure 5.29), pressure on the convex surface of the blade remains constant positive pressure up to $\phi = 15^0$, then sharply increases up to $\phi = 30^0$ and remains constant positive up to $\phi = 45^0$. After that pressure sharply decreases from positive to negative region from $\phi = 45^0$ to 110^0 and again gradually rises from negative to positive region up to $\phi = 180^0$. At rotor angle $\alpha = 280^0$ (Figure 5.29), pressure on the concave surface of the blade approximately stagnant pressure up to $\phi = 60^0$, then slightly increases to positive values up to $\phi = 130^0$. Next, pressure slightly decreases to positive values up to $\phi = 145^0$and again positive pressure approximately remains constant up to $\phi = 180^0$.

At rotor angle $\alpha = 290^0$ (Figure 5.30), pressure on the convex surface of the blade remains constant up to $\phi = 30^0$, then more decreases to positive values up to $\phi = 70^0$. After that, sharply decreases from positive to negative region from $\phi = 70^0$ to 85^0 and again gradually increases from negative to positive region up to $\phi = 180^0$. At rotor angle $\alpha = 290^0$ (Figure 5.30), pressure on the concave surface of the blade almost remains constant positive up to $\phi = 50^0$ and next, pressure slightly increases to positive values up to $\phi = 135^0$. Then pressure more decreases to positive values up to $\phi = 145^0$. Again, the positive pressure remains constant up to $\phi = 180^0$.

At rotor angle $\alpha = 300^0$ (Figure 5.31), pressure on the convex surface of the blade remains stagnant pressure up to $\phi = 20^0$, then sharply decreases from positive to negative region up to $\phi = 95^0$ and again pressure gradually increases from negative to positive region up to $\phi = 180^0$. At rotor angle $\alpha = 300^0$ (Figure 5.31), pressure on the concave surface of the blade approximately constant positive pressure up to $\phi = 70^0$, then slightly rises up to $\phi = 130^0$. After that, more decreases positive values up to $\phi = 145^0$ and again remains constant positive values up to $\phi = 180^0$.

At rotor angle $\alpha = 310^0$ (Figure 5.32), pressure on the convex surface of the blade sharply decreases from positive to negative region from $\phi = 90^0$ and gradually rises from negative to positive region up to $\phi = 180^0$. At rotor angle $\alpha = 310^0$ (Figure 5.32), pressure on the concave surface of the blade slightly decreases up to 20^0, then approximately remains constant positive up to $\phi = 120^0$, then slightly increases positive values up to $\phi = 135^0$. After that, pressure slightly decreases positive values up to $\phi = 145^0$. Then positive pressure increases up to $\phi = 180^0$.

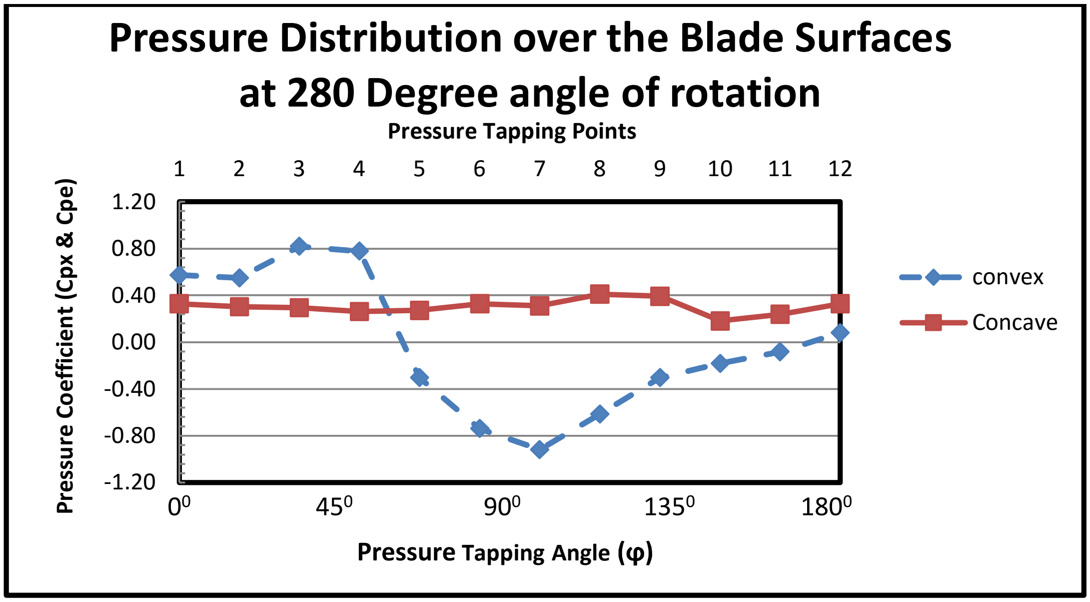

Figure 5.29 Pressure Distribution over the blade surfaces at 280 Degree angle of rotation

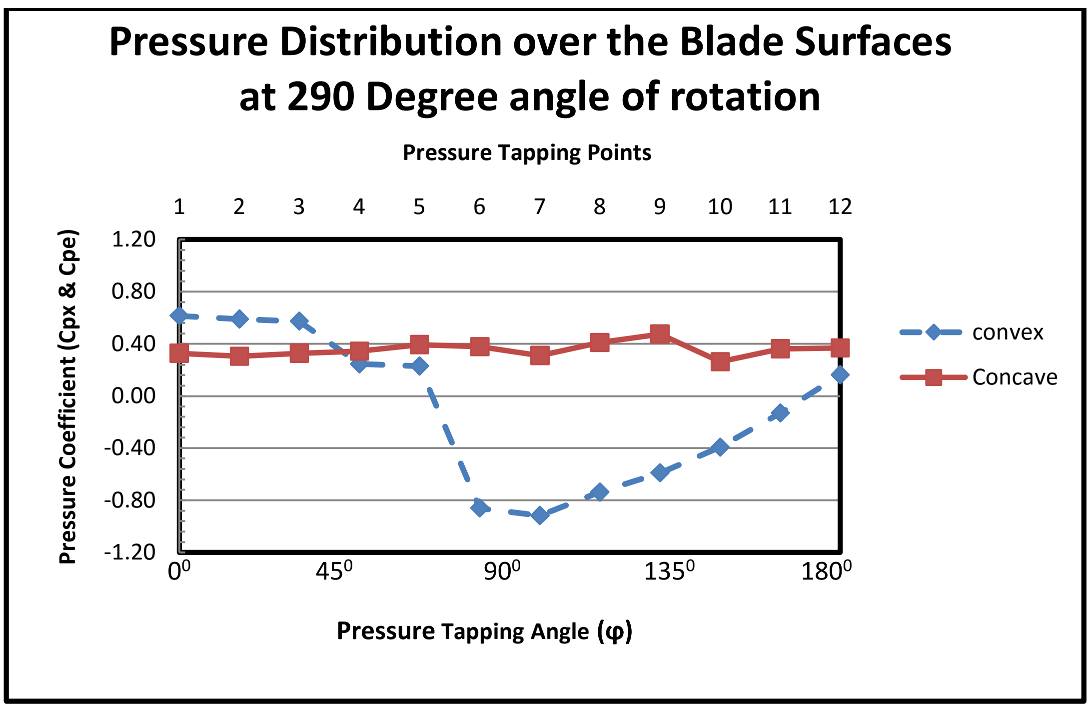

Figure 5.30 Pressure Distribution over the blade surfaces at 290 Degree angle of rotation

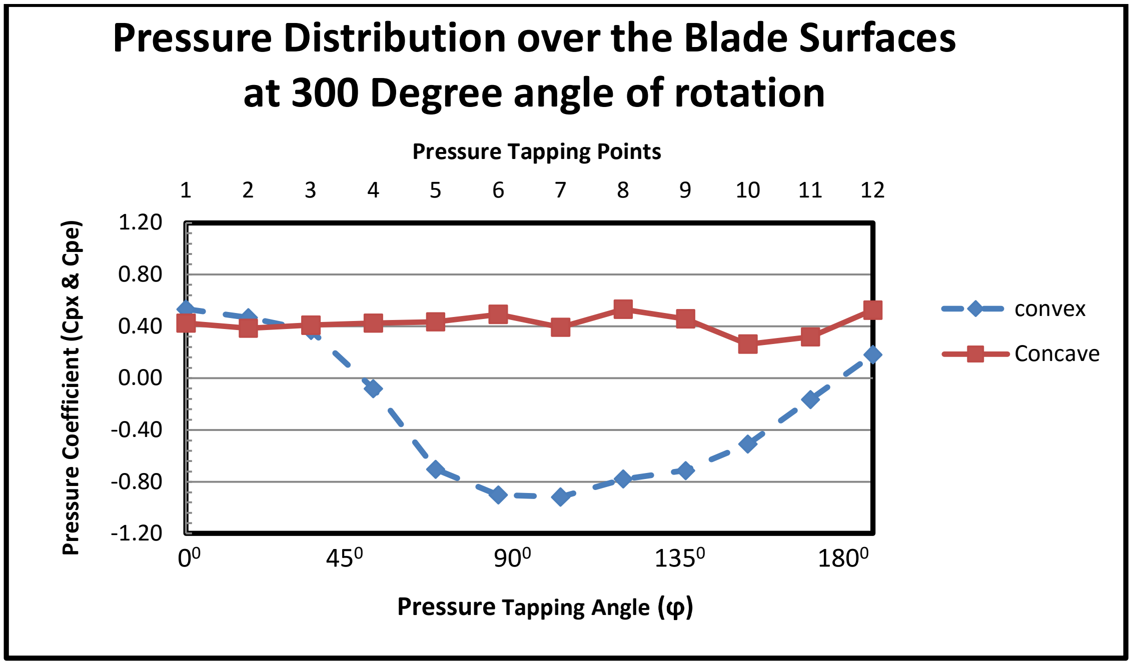

Figure 5.31 Pressure Distribution over the blade surfaces at 300 Degree angle of rotation

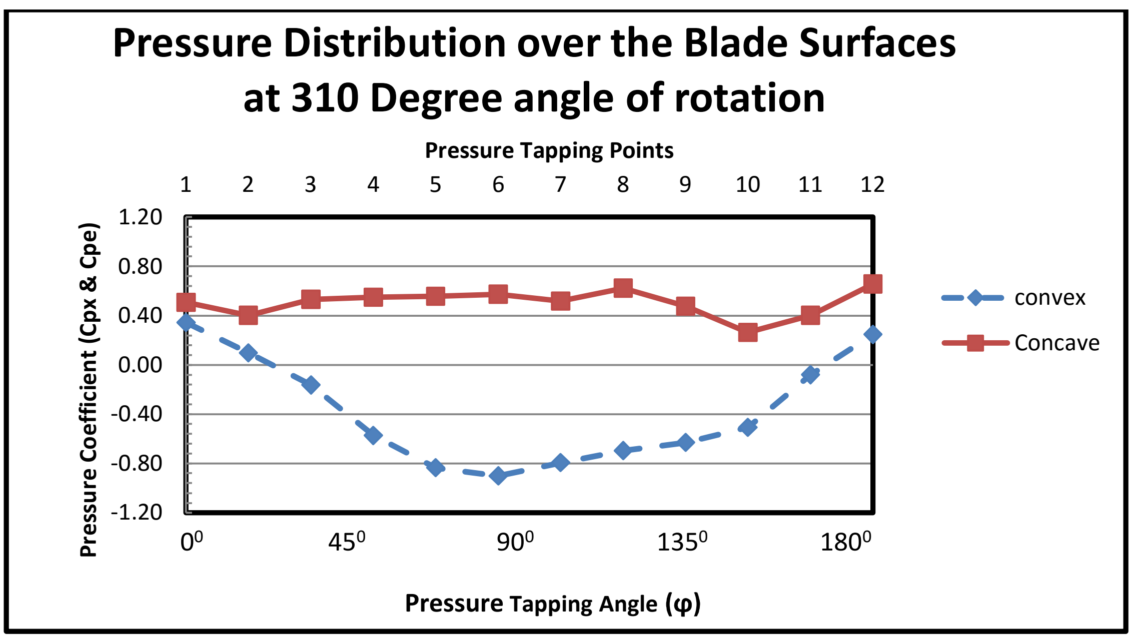

Figure 5.32 Pressure Distribution over the blade surface at 310 Degree angle of rotation

At rotor angle $\alpha = 320^0$ (Figure 5.33), pressure on the convex surface of the blade sharply decreases from positive to negative region up to $\phi = 50^0$ and gradually rises from negative to positive region up to $\phi = 180^0$. At rotor angle $\alpha = 320^0$ (Figure 5.33), pressure on the concave surface of the blade almost constant positive up to $\phi = 100^0$ and after that, slightly increases values up to $\phi = 120^0$. Next, pressure slightly decreases to positive values up to $\phi = 140^0$ and again, more increases positive values up to $\phi = 180^0$.

At rotor angle $\alpha = 330^0$ (Figure 5.34), pressure on the convex surface of the blade sharply decreases in the negative region up to $\phi = 40^0$, then pressure gradually increases from negative to positive region up to $\phi = 100^0$, then approximately constant negative pressure up to $\phi = 130^0$ and again pressure increases up to $\phi = 180^0$. At rotor angle $\alpha = 330^0$ (Figure 5.34), pressure on the concave surface of the blade approximately constant positive pressure up to $\phi = 105^0$, then pressure slightly increases to positive values up to $\phi = 125^0$. After that, pressure slightly decreases positive values up to $\phi = 160^0$ and again more rises positive values up to $\phi = 180^0$.

At rotor angle $\alpha = 340^0$ (Figure 5.35), pressure on the convex surface of the blade sharply decreases in the negative region up to $\phi = 20^0$, then pressure gradually increases from negative to positive region up to $\phi = 90^0$. Next, the negative pressure almost remains constant up to $\phi = 130^0$ and then increases. At rotor angle $\alpha = 340^0$ (Figure 5.35), pressure on the concave surface of the blade approximately remains constant positive up to $\phi = 120^0$, then slightly increases positive up to $\phi = 135^0$. After that, slightly decreases to positive values up to $\phi = 145^0$ and again more increases positive values up to $\phi = 180^0$.

At rotor angle $\alpha = 350^0$ (Figure 5.35), pressure on the convex surface of the blade slightly decreases in the negative region up to $\phi = 20^0$, then gradually increases from negative to atmospheric region up to $\phi = 70^0$. Then the negative pressure almost remains constant up to $\phi = 180^0$. At rotor angle $\alpha = 350^0$ (Figure 5.35), pressure on the concave surface of the blade almost remain constant negative up to $\phi = 50^0$, then slightly rises to positive values up to $\phi = 70^0$. Next, pressure slightly decreases up to $\phi = 100^0$ and again, slightly increases up to $\phi = 180^0$.

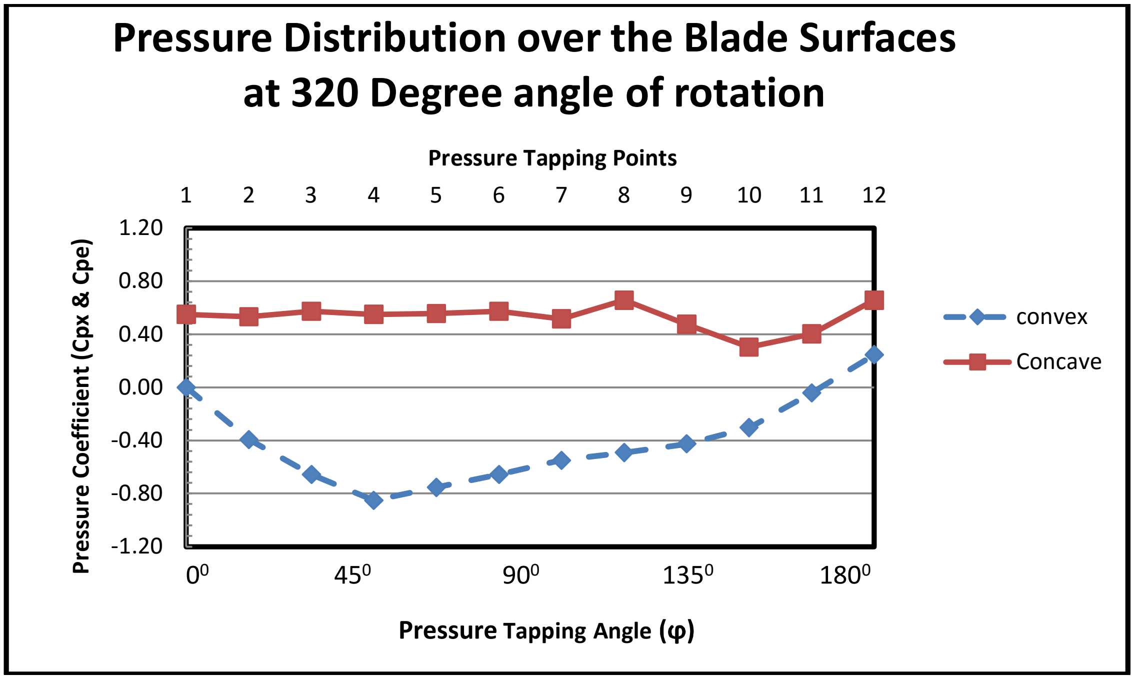

Figure 5.33 Pressure Distribution over the blade surface at 320 Degree angle of rotation

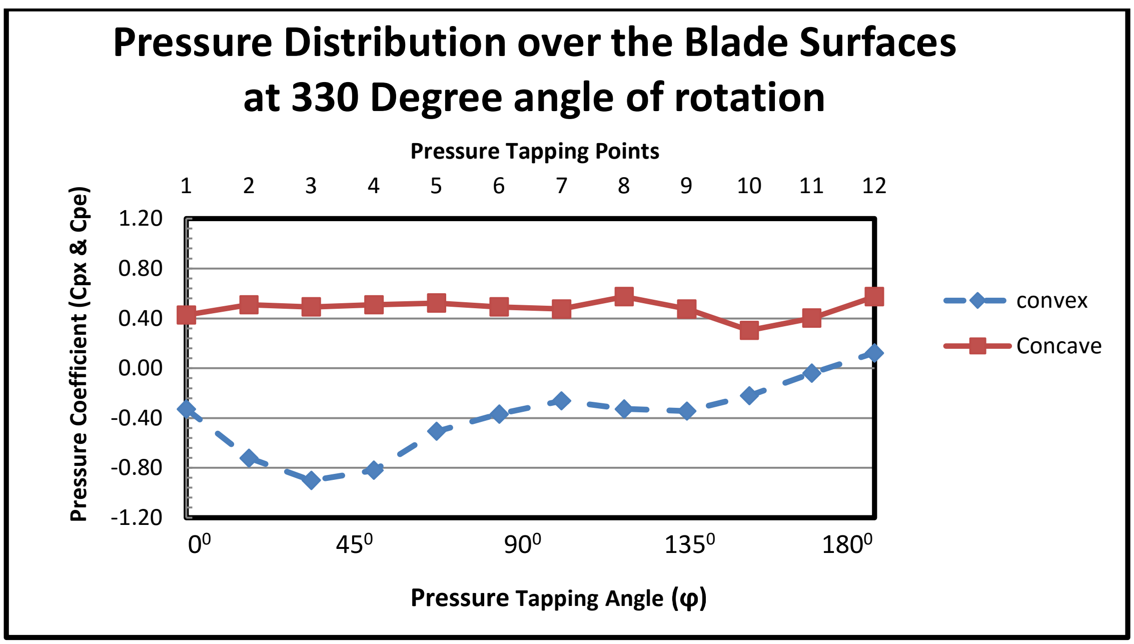

Figure 5.34 Pressure Distribution over the blade surface at 330 Degree angle of rotation

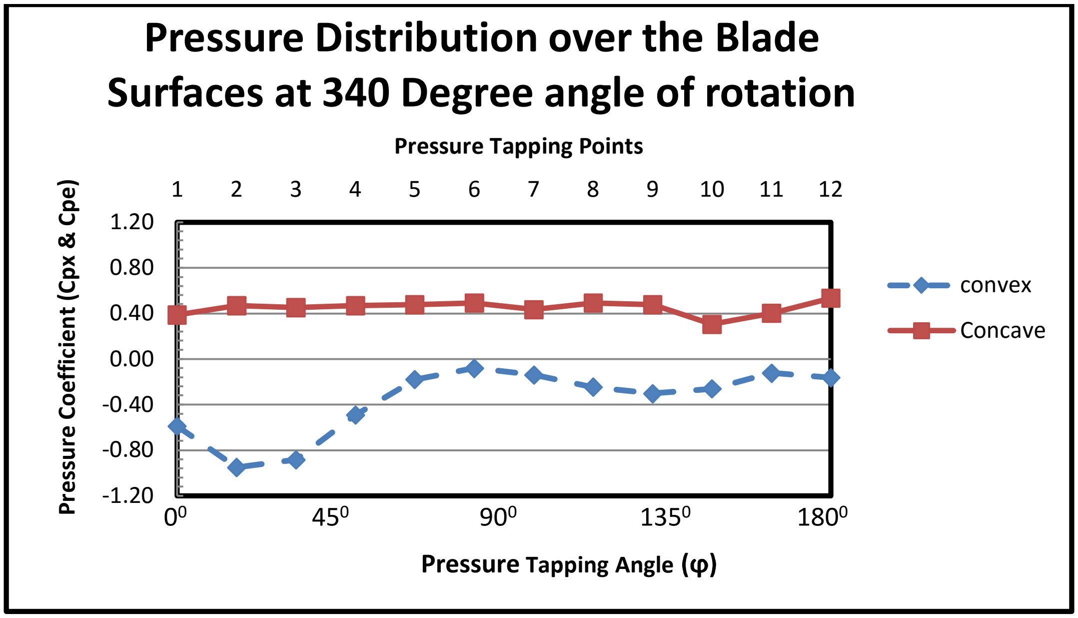

Figure 5.35 Pressure Distribution over the blade surfaces at 340 Degree angle of rotation

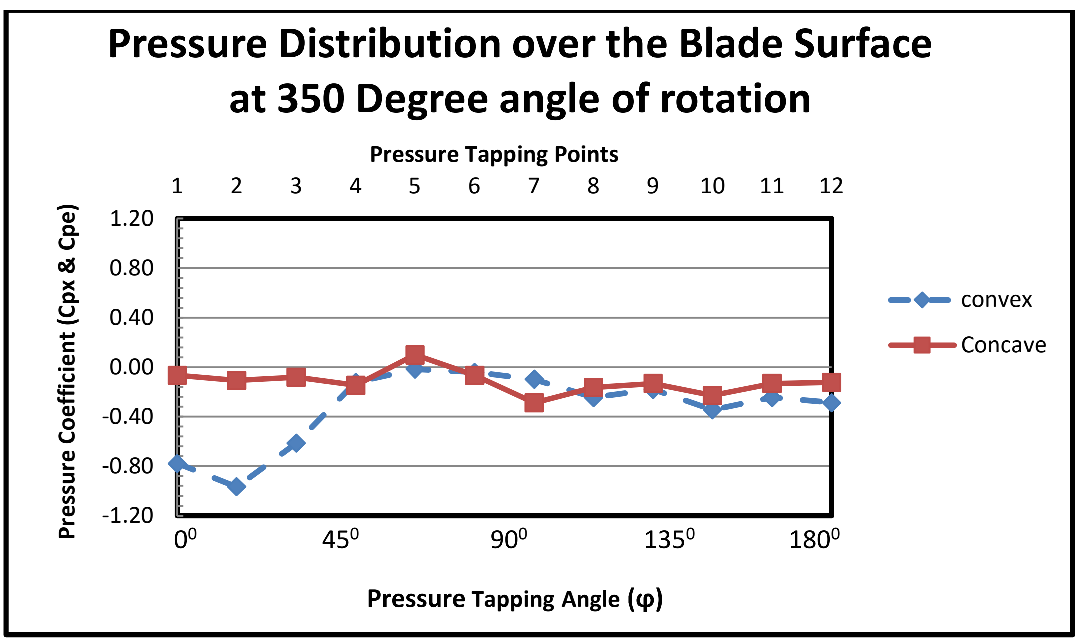

Figure 5.36 Pressure Distribution over the blade surface at 350 Degree angle of rotation

5.2.2 Drag coefficient

As mentioned earlier, the differences in pressure between the front and backside of the rotor blade result drag forces in normal and tangential direction. The variations of these drag coefficients are graphically presented here. Normal drag coefficient C_n of an individual blade of five bladed S-shaped rotor is shown here in Fig 5.37

When rotor angle $\alpha = 0^0$ to 40^0 increases, values of positive normal drag coefficient C_n increases and maximum positive normal drag coefficient C_n occurs at $\alpha = 40^0$. The value of C_n decreases smoothly between 40^0 to 120^0, but positive value of C_n between 40^0 to 110^0, negative values exist of C_n between 110^0 to 120^0. The value of C_n increases from negative to positive smoothly between 120^0 to 140^0. After that value of C_n remain constant up to 210^0, again the positive value of C_n increases smoothly between 210^0 to 240^0. The values of C_n decreases smoothly between 240^0 to 310^0 but positive value exist between 240^0 to 260^0, then negative values exist between 260^0 to 310^0. The minimum value of C_n occurs at $\alpha = 3\ 10^0$. The values of C_n increases from negative to positive smoothly between 310^0 to 0^0.

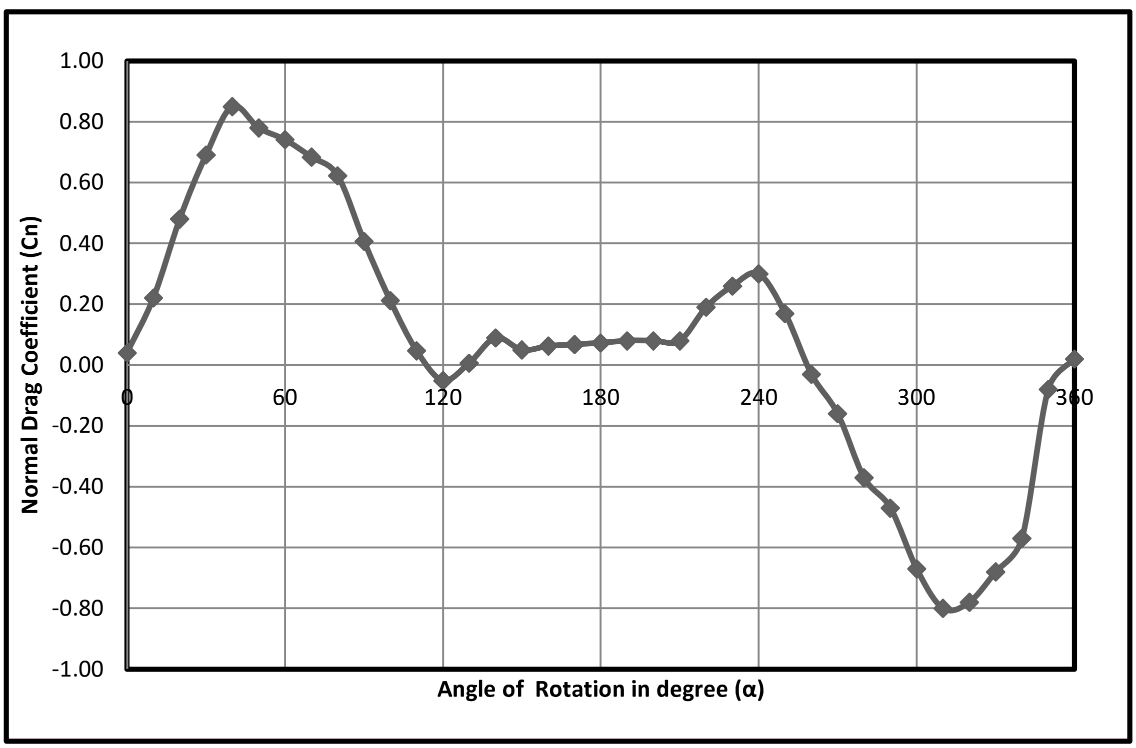

Fig 5.37 Variation of normal drag coefficient, C_n with rotor angle (α)

Tangential drag coefficient C_t of an individual blade of five bladed S-shaped rotor is shown here in Fig 5.38

When rotor angle $\alpha = 0^0$ to 15^0 increases, value of tangential drag coefficient C_t increases from negative to positive direction, then slightly constant up to 25^0 and rotor angle $\alpha = 25^0$ to 40^0 increases, value of tangential drag coefficient C_t increases negative to positive sharply. Then value of C_t decreases positive to negative abruptly between 40^0 to 70^0. Then value of C_t increases from negative to positive sharply between 70^0 to 80^0.

Then positive value of C_t nearly constant between 80^0 to 220^0. Then positive value of C_t increases abruptly between 220^0 to 260^0. Then positive value of C_t decreases abruptly between 260^0 to 270^0. And positive value of C_t increases abruptly between 260^0 to 290^0, then value of C_t decreases positive to negative smoothly between 290^0 to 320^0, again negative value of C_t approximately constant between $\alpha = 320^0$ to 0^0. The maximum value of tangential drag coefficient C_t occurs at $\alpha = 290^0$. The minimum value of tangential drag coefficient C_t occurs at $\alpha = 0^0$.

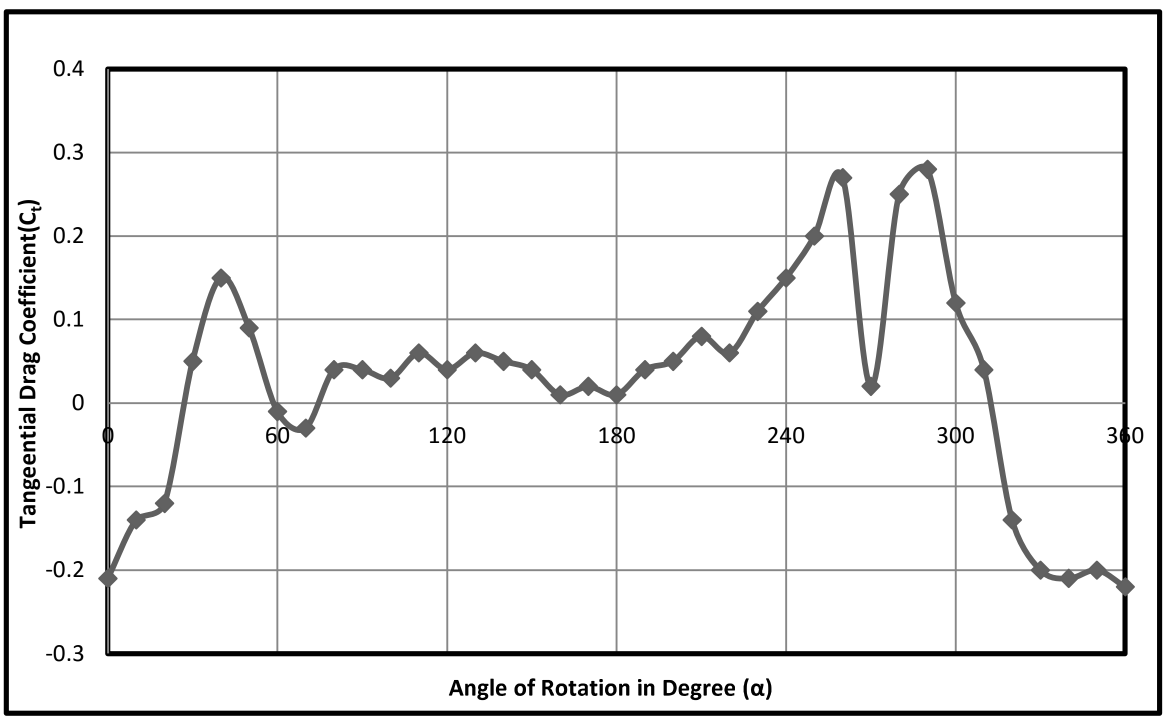

Fig 5.38 Variation of tangential drag coefficient, C_t with rotor angle (α)

5.2.3 Torque Coefficient

The torque coefficient C_q of an individual blade of five bladed S-shaped rotor is shown in Figure 5.39. As torque coefficient is a function of normal drag coefficient and distance of normal direction from the center of rotor. So the nature of torque coefficient vs. rotor angle graph as the normal drag coefficient curve.

When rotor angle $\alpha = 0^0$ to 40^0 increases, value of positive torque coefficient C_q increases and maximum positive torque coefficient C_q occurs at $\alpha = 40^0$. The value of C_q decreases smoothly between 40^0 to 120^0, but positive value of C_q between 40^0 to 110^0, negative value exist of Cq between110^0 to 120^0. The value of C_q increases from negative to positive smoothly between 120^0 to 140^0. After that value of C_q remain constant up to 210^0. Again the positive value of C_q increases smoothly between 210^0 to 240^0. The value of C_q decreases smoothly between 240^0 to 310^0, but positive value of C_q between 240^0 to 260^0, negative value exist of C_q between 260^0 to 310^0. The minimum value of C_q occurs at $\alpha = 310^0$. The value of C_q increases from negative to positive smoothly between 310^0 to 0^0.

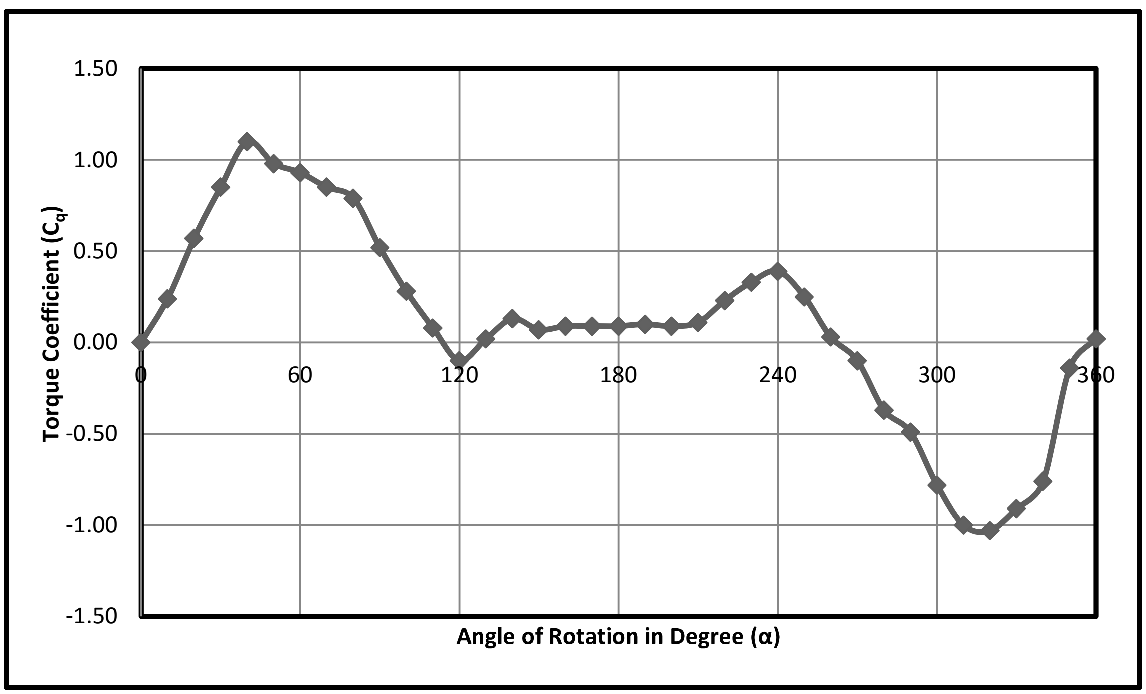

Fig 5.39 Variation of torque coefficient, C_q with rotor angle (α)

Comparisons of torque coefficient, C_q vs. angle of rotation (α) for four and five bladed S-shaped rotor is shown here in Figure 5.40

From the graphs, it is evident that with the increase of the number of blade there is no significant change in the value of torque coefficient, C_q vs. angle of rotation (α). In consideration for the torque coefficient, the graph for five bladed S-shaped Savonius rotor is of same nature as the four bladed S-shaped Savonius rotor.

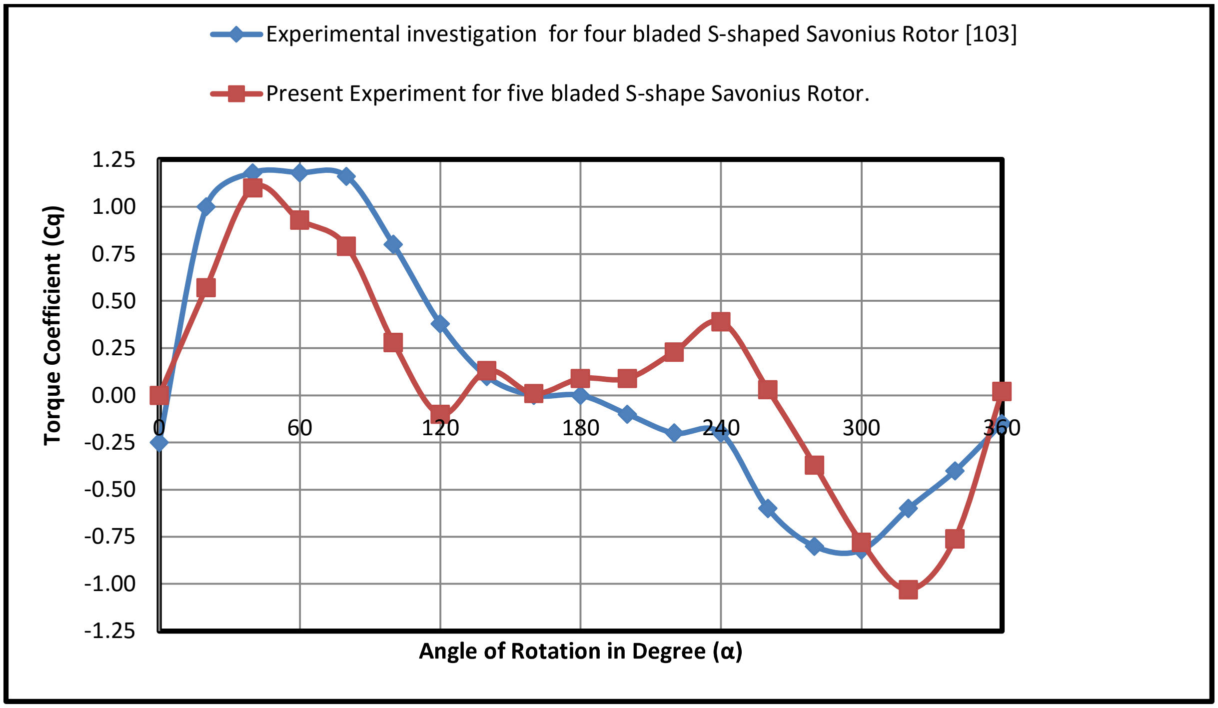

Fig 5.40 Comparisons of torque coefficient C_q vs. angle of rotation (α)

CHAPTER-6

CONCLUSIONS AND RECOMMENDATIONS

CHAPTER 6

CONCLUSIONS AND RECOMMENDATIONS

6.1 Introduction

This chapter presents the conclusions drawn from the experimental investigation of flow over the five bladed S-shaped Savonius rotor. The scope of extension and development of the present study are also included in this chapter.

6.2 Conclusions

The present study concerns the pressure distribution over the five bladed S-shaped Savonius rotor on both the convex and concave surfaces at different angle of rotations. Forces experienced by the rotor blades, drag coefficients and torque coefficients were calculated by using the raw data of pressure from the experiment. From the study, analysis and results of this research work, the following conclusions are drawn.

1. The pressure distribution over the surface of the blade of the five bladed S-shaped Savonius rotor have been measured at every 10° interval of rotor angle between $0° \leq \alpha \leq 360°$. The pressure distributions both on the concave and convex surface of the blade at different angle of rotation are presented graphically. At rotor angle $\alpha = 40^0$, difference of pressure coefficient on convex surface C_{px} and concave surface C_{pe} is maximum and value of C_{px} is greater than C_{pe}. At rotor angle $\alpha = 310^0$, difference of pressure coefficient on convex surface C_{px} and concave surface C_{pe} is minimum and value of C_{pe} is greater than C_{px}.

2. The five bladed S-shaped Savonius rotor, pressure difference is obtained from the concave and convex surface, which in turn gives drag coefficients. The drag coefficient may be resolved along the normal and tangential directions of the rotor chord.

3. For the five bladed S-shaped Savonius rotor, the normal drag is responsible for the torque production.

4. The drag and hence torque of each blade varies with rotor angle.

5. In consideration for the torque coefficient, the nature of the graph is exactly similar to that of the normal drag coefficient.

6. For the case of torque coefficient, the effect of the five bladed S-shaped Savonius rotor more efficient in the case of torque production which is very much necessary for a vertical axis wind turbine.

6.3 Recommendations

1. The same experiment can be done with different shapes and number of blades in the S-shaped Savonius Rotor.

2. The same experiment can be done with flow visualization technique to get a better understanding about the pressure distribution, drag coefficient and torque coefficient.

3. Further research is needed for studying the effects on the performance of an S-shaped Savonius rotor by placing guide vane around the rotor.

4. The effects of the shape and the number of guide vanes may also be studied.

REFERENCES

References

[1] Lysen, E.H., Bos, H.G. and Cordes, E.H. (1978), "Savonius Rotors for Water Pumping", SWD Publication, Amersfoort, The Netherlands.

[2] Islam A.K.M.S, Islam, M.Q., Razzaque, M.M. and Ashraf, R (1995), "Static Torque and Drag Characteristics of an S-shaped Savonius Rotor and Prediction of Dynamic Characterstatics", Wind Engineering Vol. 19 No.6.

[3] Gavalda, J., Massons, J. and Diaz, F. (1991), "Drag and Lift coefficient of the Savonius Wind Machine", Wind Engineering, Vol. 15, pp. 240-246.

[4] Sivasegaram, S. (1977), "Design Parameters Affectiing the Performance of Resistance Type Rotors", Wind Engineering Vol. 1, pp. 207-217.

[5] Newman, B.G (1974) , "Measurements on a Savonius Rotor with a Variable Gap", Proc. Symposium on Wind Energy: Achievements and Potential, Sherbrooke, Canada.

[6] Lysen E.H., "Introduction to Wind Energy", Steering Committee of Wind Energy for Developing Countries, P.O. BoX 85, Amesrfoort, the Netherlands.

[7] Wilson, R.E. and S.N Walker (1981), "Performance Analysis Program for Propeller Type Wind Turbines", Oregon State University, March U.S.A

[8] Ogawa, T. and H. Yoshida (1986) "The Effects of a Deflecting Plate and Rotor Plates", Bull. JSME, Vol 1.29, pp. 2115-2121.

[9] Price, Trevor J (3 May 2005), "James Blyth – Britain's First Modern Wind Power Engineer", Wind Engineering 29 (3): 191–200.

[10] Shackleton, Jonatha,. "World First for Scotland Gives Engineering Student a History Lesson", The Robert Gordon University. Retrieved 20 November 2008.

[11] Anon. Mr. Brush's Windmill Dynamo, Scientific American, Vol. 63 No. 25, 20 December 1890, p. 54.

[12] Cutler J. Cleveland, "History of Wind Energy", Encyclopedia of Energy Vol.6, Elsevier, ISBN 978-1-60119-433-6, 2007, pp. 421–422.

[13] Gipe, Paul (1993, "The Wind Industry's Experience with Aesthetic Criticism", Leonardo 26 (3): 243–248.

[14] Rasmussen, Jesper Norskov, "New record for wind turbines in 2014", Energinet.dk, 6 January 2015. Accessed: 6 January 2015. Archived on 6 January 2015.

[15] http://online.wsj.com/articles/denmarks-wind-power-output-rises-to-record-in-first-half-1409750563.

[16] REN21 (2011), “Renewables 2011: Global Status Report”.

[17] “GWEC Global Wind Statistics 2014”, GWEC. 10 February 2015.

[18] The World Wind Energy Association (2014), 2014 Half-year Report, WWEA. pp. 1–8.

[19] Watts, Jonathan & Huang, Cecily, “Winds Of Change Blow through China As Spending On Renewable Energy Soars, The Guardian”, 19 March 2012, revised on 20 March 2012. Retrieved 4 January 2012.

[20] Xinhua: Jiuquan Wind Power Base Completes First Stage, Xinhua News Agency, 4 November 2010. Retrieved from ChinaDaily.com.cn website 3 January 2013.

[21] Terra-Gen Press Release, 17 April 2012

[22] Started in August 2001, the Jaisalmer based facility crossed 1,000 MW capacity to achieve this milestone.

[23] Mills, Erin (12 July 2009), “Shepherds Flat farm lifts off”, East Oregonian. Retrieved 11 December 2009.

[24] E.ON Delivers 335-MW of Wind in Texas.

[25] Drilling Down: What Projects Made 2008 Such a Banner Year for Wind Power?

[26] AWEA: U.S. Wind Energy Projects – Texas Archived 29 December 2007 at the Wayback Machine 32. CEZ Group: The Largest Wind Farm in Europe Goes Into Trial Operation.

[27] AWEA: U.S. Wind Energy Projects – Indiana

[28] Whitelee Windfarm.

[29] Hulazan, Ned (16 February 2011), “Offshore wind power Advantages and disadvantages”, Renewable Energy Articles. Retrieved 9 April 2012.

[30] Millborrow, David (6 August 2010), "Cutting the cost of offshore wind energy". Wind Power Monthly.

[31] Charles F. Brush, “A Wind Energy Pioneer”, Danish Wind Industry Association. Accessed 2 May 2007.

[32] “Worldwide Electricity Production From Renewable Energy Sources: Stats and Figures Series: Fifteenth Inventory – Edition 2013”, (Electricity Production from Wind Sources: Main Wind Power Producing Countries – 2012 (text & table): Observer Retrieved 14 May 2014.

[33] Rick Tidball and others, “Cost and Performance Assumptions for Modeling Electricity

Generation Technologies", US National Renewable Energy Laboratory, November 2010, p.63.

[34] "Spain becomes the first European wind energy producer after overcoming Germany for the first time", Eolic Energy News. 31 December 2010. Retrieved 14 May 2011.

[35] "Committee on Climate Change (May 2011) Costs of low-carbon generation technologies".

[36] "Global wind capacity increases by 22% in 2010 – Asia leads growth", Global Wind Energy Council. 2 February 2011, Archived from the original on 18 March 2012. Retrieved 14 May 2011.

[37] "Continuing boom in wind energy – 20 GW of new capacity in 2007", Gwec.net. Retrieved 29 August 2010.

[38] "China's on-grid wind power capacity grows", China Daily. 16 August 2012. Retrieved 31 October 2012.

[39] "BTM Forecasts 340-GW of Wind Energy by 2013", Renewableenergyworld.com. 27 March 2009. Retrieved 29 August 2010.

[40] BTM Consult (2009) International Wind Energy Development World Market Update 2009.

[41] "Tackling Climate Change in the U.S.", American Solar Energy Society. January 2007. Archived from the original (PDF) on 26 November 2008. Retrieved 5 September 2007.

[42] "National Grid's response to the House of Lords Economic Affairs Select Committee investigating the economics of renewable energy", National Grid. 2008. Archived from the original on 25 March 2009.

[43] "Final Report – 2006 Minnesota Wind Integration Study", The Minnesota Public Utilities Commission. 30 November 2006. Archived from the original on 1 December 2007. Retrieved 15 January 2008.

[44] "Impact of Wind Power Generation in Ireland on the Operation of Conventional Plant and the Economic Implications", ESB National Grid. February 2004. p. 36. Archived from the original (PDF) on 29 March 2009. Retrieved 23 July 2008.

[45] Sinclair Merz Growth Scenarios for UK Renewables Generation and Implications for Future Developments and Operation of Electricity Networks BERR Publication URN 08/1021 June 2008.

[46] "Renewable energy now cheaper than new fossil fuels in Australia", Bloomberg New Energy Finance (Sydney: Bloomberg Finance). 7 February 2013.

[47] Terry Macalister, "Onshore wind farms cheapest form of UK electricity, report shows", the

Guardian.

[48] "Wind and solar boost cost-competitiveness versus fossil fuels", Bloomberg New Energy Finance.

[49] Center for National Policy, Washington DC, 11 June 2012, "What States Can Do: The Clean Revolution".

[50] "Onshore wind to reach grid parity by 2016", Business Green, 14 November 2011.

[51] Lantz, E., Hand, M. and Wiser, R. (13–17 May 2012), "The Past and Future Cost of Wind Energy", National Renewable Energy Laboratory conference paper no. 6A20-54526.

[52] Dolf Gielen, "Renewable Energy Technologies: Cost Analysis Series: Wind Power", International Renewable Energy Agency, June 2012. Accessed: 19 October 2013.

[53] Helming, Troy (2004), "Uncle Sam's New Year's Resolution", ArizonaEnergy.org

[54] "LBNL/NREL Analysis Predicts Record Low LCOE for Wind Energy in 2012–2013", US Department of Energy Wind Program Newsletter. Retrieved 10 March 2012.

[55] Salerno, E., AWEA Director of Industry and Data Analysis, as quoted in Shahan, Z. (2011) Cost of Wind Power – Kicks Coal's Butt, Better than Natural Gas (& Could Power Your EV for $0.70/gallon), CleanTechnica.com .

[56] "BWEA report on onshore wind costs", Archived from the original on 11 March 2012.

[57] "International Energy Outlook", Energy Information Administration. 2006. p. 66.

[58] Nicola Armaroli, Vincenzo Balzani, towards an electricity-powered world. In: Energy and Environmental Science 4, (2011), 3193–3222, p. 3217, doi:10.1039/c1ee01249e.

[59] "The Merit-Order Effect: A Detailed Analysis of the Price Effect of Renewable Electricity Generation on Spot Market Prices in Germany", Archived from the original on 29 August 2010. Retrieved 29 August 2010.

[60] "Solar & Wind Reach a Big Renewables Turning Point: BNEF", Bloomberg.com. 6 October 2015.

[61] "Subsidies and costs of EU energy. Project number: DESNL14583", Pages: iv, vii, 36. EcoFys, 10 October 2014. Accessed: 20 October 2014.

[62] Danielson, David (14 August 2012), "A Banner Year for the U.S. Wind Industry".

[63] Diane Cardwell (20 March 2014), "Wind Industry's New Technologies Are Helping It Compete on Price".

[64] "Offshore Wind Accelerator", The Carbon Trust. Retrieved 20 January 2015.

[65] "Global wind expert says offshore wind will be one of the cheapest UK energy sources by

2025", The Carbon Trust. 23 September 2014. Retrieved 20 January 2015.

[66] Stiesdal, Henrik, "The future of Wind Power", Engineering, 13 September 2015. American Wind Energy Association (2009) Annual Wind Industry Report, Year Ending 2008 p. 11.

[67] "IPCC Working Group III – Mitigation of Climate Change, Annex II I: Technology – specific cost and performance parameters", IPCC. 2014. p. 10. Retrieved 1 August 2014.

[68] "IPCC Working Group III – Mitigation of Climate Change, Annex II Metrics and Methodology. pg 37 to 40,41".

[69] Begona Guezuraga, Rudolf Zauner, Werner Pölz, Life cycle assessment of two different 2 MW class wind turbines, Renewable Energy 37 (2012) 37–44, p 37.

[70] "Why Australia needs wind power", Retrieved 7 January 2012.

[71] "Wind energy Frequently Asked Questions", British Wind Energy Association. Retrieved 21 April 2006.

[72] Eilperin, Juliet; Steven Mufson (16 April 2009), "Renewable Energy's Environmental Paradox", The Washington Post. Retrieved 17 April 2009.

[73] "Wind farms", Royal Society for the Protection of Birds. 14 September 2005. Retrieved 7 September 2008.

[74] Lindsay, Richard (October 2004), WIND FARMS AND BLANKET PEAT The Bog Slide of 16 October 2003 at Derrybrien, Co. Galway, Ireland, The Derrybrien Development Cooperatve Ltd. Retrieved 20 May 2009.

[75] Paul Gipe, "Wind Energy Comes of Age" .

[76] Gohlke JM et al. Environmental Health Perspectives (2008), "Health, Economy, and Environment: Sustainable Energy Choices for a Nation", Environmental Health Perspectives 116 (6): A236–A237.

[77] Professor Simon Chapman, "Summary of main conclusions reached in 25 reviews of the research literature on wind farms and health", Sydney University School of Public Health, April 2015.

[78] Hamilton, Tyler (15 December 2009), "Wind Gets Clean Bill of Health", Toronto Star (Toronto). pp. B1–B2. Retrieved 16 December 2009.

[79] W. David Colby, Robert Dobie, Geoff Leventhall, David M. Lipscomb, Robert J. McCunney, Michael T. Seilo, Bo Søndergaard, "Wind Turbine Sound and Health Effects: An Expert Panel Review", Canadian Wind Energy Association, December 2009.

[80] Thomas Kirchhoff (2014): Energy systems and landscape aesthetics. Objectify aesthetic

reviews of turbines by reference to three intersubjective landscape ideals, in: Nature Conservation and Landscape Planning 46 (1), 10-16.

[81] Energy Resources Wind power.htm.

[82] S. K. Nandi, M. N. Hoque, H. R. Ghosh, and S. K. Roy, "Potential of Wind and Solar Electricity Generation in Bangladesh".

[83] Huda, M.D., Selim, M.A., Islam A.K.M.S and Islam, M.Q. (1992), "The Performance of an S-shaped Savonius Rotor with a Deflecting Plate", RERIC Int. Energy Journal, Vol.14, No. 1, pp. 35-32.

[84] Rahman, F.M., "Torque and Drag Characteristics of a Three Bladed Savonius Rotor", M.Sc. Engg. Thesis (1999), Dept. of Mech. Engg., BUET.

[85] Kamal, F.M., "Aerodynamic Characteristics of a Vertical Axis Vane Type Wind Turbine ", M.Sc. Engg. Thesis (2008), Dept. of Mech. Engg., BUET.

[86] Nahar,S. "Torque and Drag Characteristics of a Six Bladed Savonius Rotor", M.Sc. Engg. Thesis (2008), Dept. of Mech. Engg., BUET.

[87] Bowden, G. J. and McAleese, S. A. (1984), "The Properties of Isolated and Coupled Savonius Rotors", Wind Engineering, vol. 8, no. 4, pp. 271-288.

[88] Templin, R. J. (1974), "Aerodynamic Performance Theory for the NRC Vertical Axis Wind Turbine", National Research Council of Canada, Report LTR-LA-160.

[89] Noll, R. B. and Ham, N. D. (1980), " Analytical Evaluation of the Aerodynamic Performance of a Hig-Reliability Vertical Axis Wind Turbine", Proceedings of AWEA National Conference.

[90] Wilson, R. E. and Lissman, P. B. S. (1974), "Applied Aerodynamics of Wind Power Machines", Oregon State University.

[91] Strickland, J. H. (1975), "The Darrieus Turbine: A Performance Prediction Model Using Multiple Streamtubes, Sandia Laboratories Report", SAND75-0431.

[92] Currie, I. G. (1974), "Fundamental Mechanics of Fluids", McGraw Hill.

[83] Paraschivoiu, I. and Delelaux, F. (1983), "Double Multiple Streamtubes Model with Recent Improvements", Journal of Energy, vol. 7, no. 3, pp. 250-255.

[94] Paraschivoiu, I., Fraunie, P. and Beguier, C.(1985), "Streamtube Expansion Effects on the Darrieus Wind Turbine", Journal of Propulsion, vol. 1, no. 2, pp. 150-155.

[95] Fanucci, J. B. and Watters, R. E. (1976), "Innovative Wind Machines: the Theoretical Performance of a Vertical Axis Wind Turbine", Proceedings of the Vertical Axis

Wind Turbine Technology Workshop, Sandia laboratories, SAND76- 5586, pp. III-61-95.
[96] Holme, O. (1976), "A Contribution to the Aerodynamic Theory of the Vertical Axis Wind Turbine", Proceedings of the International Symposium on Wind Energy Systems, Cambridge, pp. C4-55-72.
[97] Wilson, R. E. (1978), "Vortex Sheet Analysis of the Giromill", ASME Journal of Fluids Engineering, vol. 100, no. 3, pp. 340-342.
[98] Sawada T., Nakamura, M. and Kamada, S. (1986), "Blade Force Measurements and Flow Visualization of Savonius Rotors", Bull. JSME, vol. 29, pp. 2095-2100.
[99] Aldoss, T. K. and Obeidat, K. M. (1987), "Performance Analysis Two Savonius Rotors Running Side by Side Using the Discrete Vortex Method", Wind Engineering, vol. 11, no. 5.
[100] Jones C. N., Littler, R. D. and Manser, B. L. (1979), "The Savonius Rotor Performance and Flow", 1st BWEA Workshop.
[101] Sivasgaram, S. and Siveplan, S.(1983), "Augmentation of Power in Slow Running Vertical-Axis Wind Rotors Using Multiple Vanes", Wind Engineering, Vol. 7, No.1.
[102] Islam, A. K. M. S., Islam M. Q., Mandal A. C. and Razzaque, M. M. (1993), "Aerodynamic Characteristics of a Stationary Savonius Rotor", RERIC Int. Energy Journal, vol. 15, no. 2, pp. 125-135.
[103] Islam, M. N. Hossain and S. Saha, "Experimental investigation of aerodynamic characteristics of two, three and four bladed S-shaped starionary Savonius rotor", ICME05-FL-23.

Uncertainty:

SampleData:

22.23, 22.57, 21.71, 20.84, 23.27, 23.44, 21.71, 23.44, 21.71, 20.49, 21.27, 19.10, 21.2 mm of H_2O, convex surface at 120^0

If our measurement result denoted by X,

Then,

$X=\overline{X}\pm \Delta X$ (1)

Or, $X=\overline{x}\pm \delta$

Where, $\overline{x}$= Average value

ΔX=Uncertainty= δ=Standard deviation

Again, from Equation (1), $X= \overline{x}\ (1\pm \Delta X/X)$ (2)

Here, $\Delta X/\ \overline{x}$=Fractional Uncertainty

Percent Uncertainty= Fractional UncertaintyX100

$$\overline{x}=\frac{\sum_{i=0}^{N} Xi}{N}$$

$$=\frac{X1+X2+X3+X4+X5+-----------+XN}{N} \quad (3)$$

$$=\frac{X1+X2+X3+X4+X5+X6+X7+X8+X9+X10+X11+X12}{12}$$

$$=\frac{22.23+22.57+21.71+20.84+23.27+23.44+21.71+23.44+21.71+20.49+21.27+19.10+21.27}{12}$$

=21.56

$$\delta = \sqrt{\frac{\sum_{i=0}^{n}(Xi-\bar{x})^2}{N-1}}=$$

$$=\sqrt{\frac{\sum_{i=1}^{12}(X1-\bar{x})^2+(X2-\bar{x})^2+-----------+(X12-\bar{x})^2}{11}}$$

=1.22

$\Delta X/\ \overline{x}$=Fractional Uncertainty=1.22/21.56=0.057

Percent of Uncertainty= 0.057X100=5.7%

Tapping points	Intial reading (mm of H20)	α= 0^0 (mm of H20) Convex surface		Intial reading (mm of H20)	α= 0^0 (mm of H20) Concave surface		Pressure dif. DP (mm of H20)
1	20.84	11.11	9.72	20.66	19.10	1.56	8.16
2	20.66	11.46	9.20	20.23	18.23	2.00	7.21
3	19.97	15.63	4.34	19.97	18.23	1.74	2.60
4	19.97	18.23	1.74	19.80	18.23	1.56	0.17
5	19.27	17.80	1.48	19.10	17.36	1.74	-0.26
6	20.84	19.54	1.30	20.84	19.10	1.74	-0.43
7	21.88	20.84	1.04	21.88	17.36	4.51	-3.47
8	19.97	19.27	0.69	19.97	16.50	3.47	-2.78
9	19.27	18.23	1.04	19.27	16.50	2.78	-1.74
10	20.14	18.23	1.91	20.66	17.36	3.30	-1.39
11	19.10	17.36	1.74	19.19	16.50	2.69	-0.96
12	19.10	17.36	1.74	19.10	15.63	3.47	-1.74

Tapping points	Intial reading (mm of H20)	α= 10^0 (mm of H20) Convex surface		Intial reading (mm of H20)	α= 10^0 (mm of H20) Concave surface		Pressure dif. DP (mm of H20)
1	20.84	13.20	7.64	20.66	17.36	3.30	4.34
2	20.66	16.50	4.17	20.23	17.80	2.43	1.74
3	19.97	19.10	0.87	19.97	16.50	3.47	-2.60
4	19.97	18.23	1.74	19.80	16.93	2.87	-1.13
5	19.27	18.67	0.61	19.27	16.15	3.13	-2.52
6	20.84	20.84	0.00	20.84	17.36	3.47	-3.47
7	21.88	21.88	0.00	21.88	17.36	4.51	-4.51
8	19.97	21.01	-1.04	19.97	15.19	4.78	-5.82
9	19.27	19.27	0.00	19.27	14.76	4.51	-4.51
10	20.14	19.10	1.04	20.66	15.63	5.04	-3.99
11	19.10	17.19	1.91	19.19	14.33	4.86	-2.95
12	19.10	17.54	1.56	19.10	14.76	4.34	-2.78

Tapping points	Intial reading (mm of H20)	α= 20⁰ (mm of H20) Convex surface		Intial reading (mm of H20)	α= 20⁰ (mm of H20) Concave surface		Pressure dif. DP (mm of H20)
1	20.84	18.23	2.60	20.66	15.63	5.04	-2.43
2	20.66	20.14	0.52	20.23	16.93	3.30	-2.78
3	19.97	21.71	-1.74	19.97	14.33	5.64	-7.38
4	19.97	19.54	0.43	19.80	14.33	5.47	-5.04
5	19.27	19.71	-0.43	19.27	14.33	4.95	-5.38
6	20.84	21.71	-0.87	20.84	14.76	6.08	-6.95
7	21.88	22.57	-0.69	21.88	14.76	7.12	-7.81
8	19.97	22.14	-2.17	19.97	13.02	6.95	-9.12
9	19.27	20.84	-1.56	19.27	12.16	7.12	-8.68
10	20.14	19.54	0.61	20.66	13.02	7.64	-7.03
11	19.10	18.84	0.26	19.19	11.29	7.90	-7.64
12	19.10	19.80	-0.69	19.10	12.16	6.95	-7.64

Tapping points	Intial reading (mm of H20)	α= 30⁰ (mm of H20) Convex surface		Intial reading (mm of H20)	α= 30⁰ (mm of H20) Concave surface		Pressure dif. DP (mm of H20)
1	20.84	28.22	-7.38	20.66	13.46	7.21	-14.59
2	20.66	22.57	-1.91	20.23	13.89	6.34	-8.25
3	19.97	24.31	-4.34	19.97	12.16	7.81	-12.16
4	19.97	21.71	-1.74	19.80	13.02	6.77	-8.51
5	19.27	20.84	-1.56	19.27	12.16	7.12	-8.68
6	20.84	22.57	-1.74	20.84	13.02	7.81	-9.55
7	21.88	23.44	-1.56	21.88	13.02	8.86	-10.42
8	19.97	22.57	-2.60	19.97	11.29	8.68	-11.29
9	19.27	20.32	-1.04	19.27	9.98	9.29	-10.33
10	20.14	19.97	0.17	20.66	10.85	9.81	-9.64
11	19.10	19.10	0.00	19.19	9.55	9.64	-9.64
12	19.10	19.97	-0.87	19.10	12.16	6.95	-7.81

Tapping points	Intial reading (mm of H20)	α= 20^0 (mm of H20) Convex surface		Intial reading (mm of H20)	α= 20^0 (mm of H20) Concave surface		Pressure dif. DP (mm of H20)
1	20.84	18.23	2.60	20.66	15.63	5.04	-2.43
2	20.66	20.14	0.52	20.23	16.93	3.30	-2.78
3	19.97	21.71	-1.74	19.97	14.33	5.64	-7.38
4	19.97	19.54	0.43	19.80	14.33	5.47	-5.04
5	19.27	19.71	-0.43	19.27	14.33	4.95	-5.38
6	20.84	21.71	-0.87	20.84	14.76	6.08	-6.95
7	21.88	22.57	-0.69	21.88	14.76	7.12	-7.81
8	19.97	22.14	-2.17	19.97	13.02	6.95	-9.12
9	19.27	20.84	-1.56	19.27	12.16	7.12	-8.68
10	20.14	19.54	0.61	20.66	13.02	7.64	-7.03
11	19.10	18.84	0.26	19.19	11.29	7.90	-7.64
12	19.10	19.80	-0.69	19.10	12.16	6.95	-7.64

Tapping points	Intial reading (mm of H20)	α= 30^0 (mm of H20) Convex surface		Intial reading (mm of H20)	α= 30^0 (mm of H20) Concave surface		Pressure dif. DP (mm of H20)
1	20.84	28.22	-7.38	20.66	13.46	7.21	-14.59
2	20.66	22.57	-1.91	20.23	13.89	6.34	-8.25
3	19.97	24.31	-4.34	19.97	12.16	7.81	-12.16
4	19.97	21.71	-1.74	19.80	13.02	6.77	-8.51
5	19.27	20.84	-1.56	19.27	12.16	7.12	-8.68
6	20.84	22.57	-1.74	20.84	13.02	7.81	-9.55
7	21.88	23.44	-1.56	21.88	13.02	8.86	-10.42
8	19.97	22.57	-2.60	19.97	11.29	8.68	-11.29
9	19.27	20.32	-1.04	19.27	9.98	9.29	-10.33
10	20.14	19.97	0.17	20.66	10.85	9.81	-9.64
11	19.10	19.10	0.00	19.19	9.55	9.64	-9.64
12	19.10	19.97	-0.87	19.10	12.16	6.95	-7.81

Tapping points	Intial reading (mm of H20)	α= 40^0 (mm of H20) Convex surface		Intial reading (mm of H20)	α= 40^0 (mm of H20) Concave surface		Pressure dif. DP (mm of H20)
1	20.84	30.56	-9.72	20.66	13.89	6.77	-16.50
2	20.66	26.92	-6.25	20.23	13.02	7.21	-13.46
3	19.97	25.18	-5.21	19.97	10.85	9.12	-14.33
4	19.97	22.57	-2.60	19.80	10.42	9.38	-11.98
5	19.27	24.31	-5.04	19.27	11.29	7.99	-13.02
6	20.84	24.31	-3.47	20.84	11.29	9.55	-13.02
7	21.88	23.88	-2.00	21.88	11.29	10.59	-12.59
8	19.97	20.84	-0.87	19.97	9.55	10.42	-11.29
9	19.27	21.01	-1.74	19.27	8.68	10.59	-12.33
10	20.14	19.97	0.17	20.66	10.42	10.25	-10.07
11	19.10	19.10	0.00	19.19	9.98	9.20	-9.20
12	19.10	19.97	-0.87	19.10	12.16	6.95	-7.81

Tapping points	Intial reading (mm of H20)	α= 50^0 (mm of H20) Convex surface		Intial reading (mm of H20)	α= 50^0 (mm of H20) Concave surface		Pressure dif. DP (mm of H20)
1	20.84	23.88	-3.04	20.66	13.02	7.64	-10.68
2	20.66	23.79	-3.13	20.23	12.16	8.07	-11.20
3	19.97	22.57	-2.60	19.97	12.16	7.81	-10.42
4	19.97	21.71	-1.74	19.80	12.16	7.64	-9.38
5	19.27	20.84	-1.56	19.27	10.42	8.86	-10.42
6	20.84	23.88	-3.04	20.84	11.29	9.55	-12.59
7	21.88	23.96	-2.08	21.88	11.72	10.16	-12.24
8	19.97	23.01	-3.04	19.97	9.55	10.42	-13.46
9	19.27	20.84	-1.56	19.27	9.55	9.72	-11.29
10	20.14	20.84	-0.69	20.66	10.85	9.81	-10.51
11	19.10	20.40	-1.30	19.19	10.42	8.77	-10.07
12	19.10	21.27	-2.17	19.10	13.02	6.08	-8.25

Tapping points	Intial reading (mm of H20)	α= 60^0 (mm of H20) Convex surface		Intial reading (mm of H20)	α= 60^0 (mm of H20) Concave surface		Pressure dif. DP (mm of H20)
1	20.84	22.75	-1.91	20.66	13.89	6.77	-8.68
2	20.66	23.27	-2.60	20.23	12.16	8.07	-10.68
3	19.97	21.71	-1.74	19.97	11.29	8.68	-10.42
4	19.97	21.19	-1.22	19.80	11.29	8.51	-9.72
5	19.27	20.84	-1.56	19.27	11.29	7.99	-9.55
6	20.84	23.44	-2.60	20.84	12.16	8.68	-11.29
7	21.88	23.62	-1.74	21.88	12.16	9.72	-11.46
8	19.97	22.75	-2.78	19.97	10.42	9.55	-12.33
9	19.27	20.84	-1.56	19.27	9.98	9.29	-10.85
10	20.14	21.27	-1.13	20.66	11.29	9.38	-10.51
11	19.10	20.66	-1.56	19.19	11.29	7.90	-9.46
12	19.10	21.71	-2.60	19.10	13.02	6.08	-8.68

Tapping points	Intial reading (mm of H20)	α= 70^0 (mm of H20) Convex surface		Intial reading (mm of H20)	α= 70^0 (mm of H20) Concave surface		Pressure dif. DP (mm of H20)
1	20.84	23.62	-2.78	20.66	14.76	5.90	-8.68
2	20.66	23.44	-2.78	20.23	13.02	7.21	-9.98
3	19.97	21.88	-1.91	19.97	13.02	6.95	-8.86
4	19.97	20.84	-0.87	19.80	13.02	6.77	-7.64
5	19.27	20.84	-1.56	19.27	12.16	7.12	-8.68
6	20.84	23.44	-2.60	20.84	12.59	8.25	-10.85
7	21.88	23.79	-1.91	21.88	13.02	8.86	-10.77
8	19.97	22.57	-2.60	19.97	11.29	8.68	-11.29
9	19.27	20.84	-1.56	19.27	10.42	8.86	-10.42
10	20.14	21.71	-1.56	20.66	12.16	8.51	-10.07
11	19.10	20.84	-1.74	19.19	11.29	7.90	-9.64
12	19.10	21.88	-2.78	19.10	13.02	6.08	-8.86

Tapping points	Intial reading (mm of H20)	α= 80⁰ (mm of H20) Convex surface		Intial reading (mm of H20)	α= 80⁰ (mm of H20) Concave surface		Pressure dif. DP (mm of H20)
1	20.84	23.62	-2.78	20.66	15.63	5.04	-7.81
2	20.66	23.44	-2.78	20.23	13.02	7.21	-9.98
3	19.97	21.71	-1.74	19.97	13.02	6.95	-8.68
4	19.97	20.84	-0.87	19.80	13.02	6.77	-7.64
5	19.27	20.84	-1.56	19.27	12.16	7.12	-8.68
6	20.84	23.44	-2.60	20.84	12.59	8.25	-10.85
7	21.88	23.44	-1.56	21.88	13.02	8.86	-10.42
8	19.97	21.71	-1.74	19.97	13.46	6.51	-8.25
9	19.27	20.40	-1.13	19.27	11.72	7.55	-8.68
10	20.14	21.27	-1.13	20.66	13.02	7.64	-8.77
11	19.10	20.40	-1.30	19.19	13.02	6.16	-7.47
12	19.10	21.27	-2.17	19.10	15.63	3.47	-5.64

Tapping points	Intial reading (mm of H20)	α= 90⁰ (mm of H20) Convex surface		Intial reading (mm of H20)	α= 90⁰ (mm of H20) Concave surface		Pressure dif. DP (mm of H20)
1	20.84	22.57	-1.74	20.66	18.23	2.43	-4.17
2	20.66	22.57	-1.91	20.23	15.63	4.60	-6.51
3	19.97	22.05	-2.08	19.97	16.50	3.47	-5.56
4	19.97	21.53	-1.56	19.80	16.06	3.73	-5.30
5	19.27	20.40	-1.13	19.27	14.76	4.51	-5.64
6	20.84	22.57	-1.74	20.84	15.63	5.21	-6.95
7	21.88	22.92	-1.04	21.88	16.50	5.38	-6.42
8	19.97	21.71	-1.74	19.97	14.76	5.21	-6.95
9	19.27	20.66	-1.39	19.27	14.76	4.51	-5.90
10	20.14	21.53	-1.39	20.66	16.50	4.17	-5.56
11	19.10	19.97	-0.87	19.19	17.36	1.82	-2.69
12	19.10	20.84	-1.74	19.10	18.23	0.87	-2.60

Tapping points	Intial reading (mm of H20)	α= 100^0 (mm of H20) Convex surface		Intial reading (mm of H20)	α= 100^0 (mm of H20) Concave surface		Pressure dif. DP (mm of H20)
1	20.84	22.57	-1.74	20.66	19.97	0.69	-2.43
2	20.66	22.23	-1.56	20.23	16.93	3.30	-4.86
3	19.97	20.84	-0.87	19.97	18.23	1.74	-2.60
4	19.97	19.97	0.00	19.80	17.36	2.43	-2.43
5	19.27	20.14	-0.87	19.27	16.06	3.21	-4.08
6	20.84	22.57	-1.74	20.84	18.67	2.17	-3.91
7	21.88	22.57	-0.69	21.88	19.54	2.34	-3.04
8	19.97	20.84	-0.87	19.97	18.23	1.74	-2.60
9	19.27	21.19	-1.91	19.27	18.23	1.04	-2.95
10	20.14	21.36	-1.22	20.66	19.10	1.56	-2.78
11	19.10	19.97	-0.87	19.19	19.10	0.09	-0.96
12	19.10	20.84	-1.74	19.10	19.10	0.00	-1.74

Tapping points	Intial reading (mm of H20)	α= 110^0 (mm of H20) Convex surface		Intial reading (mm of H20)	α= 110^0 (mm of H20) Concave surface		Pressure dif. DP (mm of H20)
1	20.84	22.57	-1.74	20.66	21.27	-0.61	-1.13
2	20.66	22.23	-1.56	20.23	19.10	1.13	-2.69
3	19.97	20.84	-0.87	19.97	19.97	0.00	-0.87
4	19.97	20.14	-0.17	19.80	19.10	0.69	-0.87
5	19.27	19.97	-0.69	19.27	17.80	1.48	-2.17
6	20.84	22.57	-1.74	20.84	20.84	0.00	-1.74
7	21.88	22.75	-0.87	21.88	22.57	-0.69	-0.17
8	19.97	21.71	-1.74	19.97	21.71	-1.74	0.00
9	19.27	20.40	-1.13	19.27	21.71	-2.43	1.30
10	20.14	21.27	-1.13	20.66	21.71	-1.04	-0.09
11	19.10	19.62	-0.52	19.19	19.97	-0.78	0.26
12	19.10	20.84	-1.74	19.10	20.84	-1.74	0.00

Tapping points	Intial reading (mm of H20)	α= 120^0 (mm of H20) Convex surface		Intial reading (mm of H20)	α= 120^0 (mm of H20) Concave surface		Pressure dif. DP (mm of H20)
1	20.84	22.23	-1.39	20.66	22.57	-1.91	0.52
2	20.66	22.57	-1.91	20.23	21.27	-1.04	-0.87
3	19.97	21.71	-1.74	19.97	21.71	-1.74	0.00
4	19.97	20.84	-0.87	19.80	21.27	-1.48	0.61
5	19.27	20.84	-1.56	19.27	20.84	-1.56	0.00
6	20.84	23.27	-2.43	20.84	23.36	-2.52	0.09
7	21.88	23.44	-1.56	21.88	25.18	-3.30	1.74
8	19.97	21.71	-1.74	19.97	22.57	-2.60	0.87
9	19.27	20.49	-1.22	19.27	22.57	-3.30	2.08
10	20.14	21.27	-1.13	20.66	22.57	-1.91	0.78
11	19.10	19.10	0.00	19.19	20.84	-1.65	1.65
12	19.10	21.27	-2.17	19.10	21.27	-2.17	0.00

Tapping points	Intial reading (mm of H20)	α= 130^0 (mm of H20) Convex surface		Intial reading (mm of H20)	α= 130^0 (mm of H20) Concave surface		Pressure dif. DP (mm of H20)
1	20.84	23.62	-2.78	20.66	22.57	-1.91	-0.87
2	20.66	23.44	-2.78	20.23	22.57	-2.34	-0.43
3	19.97	22.57	-2.60	19.97	22.14	-2.17	-0.43
4	19.97	21.71	-1.74	19.80	21.71	-1.91	0.17
5	19.27	22.31	-3.04	19.27	21.71	-2.43	-0.61
6	20.84	25.18	-4.34	20.84	23.44	-2.60	-1.74
7	21.88	25.18	-3.30	21.88	24.31	-2.43	-0.87
8	19.97	23.44	-3.47	19.97	23.44	-3.47	0.00
9	19.27	20.66	-1.39	19.27	22.57	-3.30	1.91
10	20.14	21.27	-1.13	20.66	23.01	-2.34	1.22
11	19.10	20.84	-1.74	19.19	21.71	-2.52	0.78
12	19.10	19.80	-0.69	19.10	21.71	-2.60	1.91

Tapping points	Intial reading (mm of H20)	α= 140^0 (mm of H20) Convex surface		Intial reading (mm of H20)	α= 140^0 (mm of H20) Concave surface		Pressure dif. DP (mm of H20)
1	20.84	23.44	-2.60	20.66	22.57	-1.91	-0.69
2	20.66	23.27	-2.60	20.23	22.57	-2.34	-0.26
3	19.97	22.57	-2.60	19.97	21.71	-1.74	-0.87
4	19.97	22.57	-2.60	19.80	21.71	-1.91	-0.69
5	19.27	23.44	-4.17	19.27	20.84	-1.56	-2.60
6	20.84	26.48	-5.64	20.84	23.44	-2.60	-3.04
7	21.88	26.92	-5.04	21.88	24.31	-2.43	-2.60
8	19.97	25.18	-5.21	19.97	22.57	-2.60	-2.60
9	19.27	20.84	-1.56	19.27	21.71	-2.43	0.87
10	20.14	21.36	-1.22	20.66	22.57	-1.91	0.69
11	19.10	19.54	-0.43	19.19	20.84	-1.65	1.22
12	19.10	19.27	-0.17	19.10	20.84	-1.74	1.56

Tapping points	Intial reading (mm of H20)	α= 150^0 (mm of H20) Convex surface		Intial reading (mm of H20)	α= 150^0 (mm of H20) Concave surface		Pressure dif. DP (mm of H20)
1	20.84	23.44	-2.60	20.66	22.57	-1.91	-0.69
2	20.66	23.27	-2.60	20.23	22.57	-2.34	-0.26
3	19.97	21.88	-1.91	19.97	21.71	-1.74	-0.17
4	19.97	21.71	-1.74	19.80	21.27	-1.48	-0.26
5	19.27	22.14	-2.87	19.27	20.84	-1.56	-1.30
6	20.84	25.18	-4.34	20.84	23.44	-2.60	-1.74
7	21.88	26.05	-4.17	21.88	24.31	-2.43	-1.74
8	19.97	24.74	-4.78	19.97	22.57	-2.60	-2.17
9	19.27	21.36	-2.08	19.27	21.71	-2.43	0.35
10	20.14	21.01	-0.87	20.66	22.57	-1.91	1.04
11	19.10	19.10	0.00	19.19	20.66	-1.48	1.48
12	19.10	19.80	-0.69	19.10	21.27	-2.17	1.48

Tapping points	Intial reading (mm of H20)	α= 160⁰ (mm of H20) Convex surface		Intial reading (mm of H20)	α= 160⁰ (mm of H20) Concave surface		Pressure dif. DP (mm of H20)
1	20.84	22.75	-1.91	20.66	22.14	-1.48	-0.43
2	20.66	22.57	-1.91	20.23	22.14	-1.91	0.00
3	19.97	21.88	-1.91	19.97	21.71	-1.74	-0.17
4	19.97	21.71	-1.74	19.80	20.84	-1.04	-0.69
5	19.27	21.88	-2.60	19.27	20.66	-1.39	-1.22
6	20.84	25.18	-4.34	20.84	23.01	-2.17	-2.17
7	21.88	26.05	-4.17	21.88	23.62	-1.74	-2.43
8	19.97	24.14	-4.17	19.97	21.71	-1.74	-2.43
9	19.27	20.84	-1.56	19.27	21.71	-2.43	0.87
10	20.14	21.27	-1.13	20.66	22.57	-1.91	0.78
11	19.10	19.10	0.00	19.19	20.40	-1.22	1.22
12	19.10	20.40	-1.30	19.10	21.27	-2.17	0.87

Tapping points	Intial reading (mm of H20)	α= 170⁰ (mm of H20) Convex surface		Intial reading (mm of H20)	α= 170⁰ (mm of H20) Concave surface		Pressure dif. DP (mm of H20)
1	20.84	22.75	-1.91	20.66	22.05	-1.39	-0.52
2	20.66	22.57	-1.91	20.23	21.71	-1.48	-0.43
3	19.97	21.88	-1.91	19.97	21.71	-1.74	-0.17
4	19.97	21.27	-1.30	19.80	20.84	-1.04	-0.26
5	19.27	21.53	-2.26	19.27	20.40	-1.13	-1.13
6	20.84	24.31	-3.47	20.84	22.57	-1.74	-1.74
7	21.88	26.05	-4.17	21.88	23.44	-1.56	-2.60
8	19.97	25.18	-5.21	19.97	21.71	-1.74	-3.47
9	19.27	20.84	-1.56	19.27	21.71	-2.43	0.87
10	20.14	21.27	-1.13	20.66	22.57	-1.91	0.78
11	19.10	19.27	-0.17	19.19	20.40	-1.22	1.04
12	19.10	20.40	-1.30	19.10	20.84	-1.74	0.43

\

Tapping points	Intial reading (mm of H20)	α= 180^0 (mm of H20) Convex surface		Intial reading (mm of H20)	α= 180^0 (mm of H20) Concave surface		Pressure dif. DP (mm of H20)
1	20.84	22.57	-1.74	20.66	22.14	-1.48	-0.26
2	20.66	22.57	-1.91	20.23	21.71	-1.48	-0.43
3	19.97	21.71	-1.74	19.97	21.71	-1.74	0.00
4	19.97	20.84	-0.87	19.80	20.84	-1.04	0.17
5	19.27	21.19	-1.91	19.27	20.40	-1.13	-0.78
6	20.84	23.88	-3.04	20.84	22.57	-1.74	-1.30
7	21.88	26.48	-4.60	21.88	23.88	-2.00	-2.60
8	19.97	26.05	-6.08	19.97	21.71	-1.74	-4.34
9	19.27	20.84	-1.56	19.27	21.71	-2.43	0.87
10	20.14	23.01	-2.87	20.66	22.23	-1.56	-1.30
11	19.10	18.23	0.87	19.19	19.97	-0.78	1.65
12	19.10	19.80	-0.69	19.10	20.40	-1.30	0.61

Tapping points	Intial reading (mm of H20)	α= 190^0 (mm of H20) Convex surface		Intial reading (mm of H20)	α= 190^0 (mm of H20) Concave surface		Pressure dif. DP (mm of H20)
1	20.84	22.57	-1.74	20.66	21.71	-1.04	-0.69
2	20.66	22.57	-1.91	20.23	21.71	-1.48	-0.43
3	19.97	22.14	-2.17	19.97	21.53	-1.56	-0.61
4	19.97	20.84	-0.87	19.80	20.84	-1.04	0.17
5	19.27	20.84	-1.56	19.27	20.84	-1.56	0.00
6	20.84	24.31	-3.47	20.84	22.57	-1.74	-1.74
7	21.88	26.92	-5.04	21.88	23.44	-1.56	-3.47
8	19.97	26.05	-6.08	19.97	21.71	-1.74	-4.34
9	19.27	21.71	-2.43	19.27	20.84	-1.56	-0.87
10	20.14	21.36	-1.22	20.66	21.71	-1.04	-0.17
11	19.10	17.80	1.30	19.19	19.97	-0.78	2.08
12	19.10	17.71	1.39	19.10	20.84	-1.74	3.13

Tapping points	Intial reading (mm of H20)	α= 200^0 (mm of H20) Convex surface		Intial reading (mm of H20)	α= 200^0 (mm of H20) Concave surface		Pressure dif. DP (mm of H20)
1	20.84	22.57	-1.74	20.66	22.14	-1.48	-0.26
2	20.66	22.57	-1.91	20.23	21.71	-1.48	-0.43
3	19.97	21.27	-1.30	19.97	21.71	-1.74	0.43
4	19.97	20.84	-0.87	19.80	20.84	-1.04	0.17
5	19.27	20.84	-1.56	19.27	20.32	-1.04	-0.52
6	20.84	23.88	-3.04	20.84	22.57	-1.74	-1.30
7	21.88	26.22	-4.34	21.88	23.44	-1.56	-2.78
8	19.97	26.92	-6.95	19.97	21.71	-1.74	-5.21
9	19.27	23.01	-3.73	19.27	21.71	-2.43	-1.30
10	20.14	21.71	-1.56	20.66	22.14	-1.48	-0.09
11	19.10	18.67	0.43	19.19	20.84	-1.65	2.08
12	19.10	14.76	4.34	19.10	20.84	-1.74	6.08

Tapping points	Intial reading (mm of H20)	α= 210^0 (mm of H20) Convex surface		Intial reading (mm of H20)	α= 210^0 (mm of H20) Concave surface		Pressure dif. DP (mm of H20)
1	20.84	22.57	-1.74	20.66	22.57	-1.91	0.17
2	20.66	22.57	-1.91	20.23	22.23	-2.00	0.09
3	19.97	21.71	-1.74	19.97	21.88	-1.91	0.17
4	19.97	21.01	-1.04	19.80	21.71	-1.91	0.87
5	19.27	21.71	-2.43	19.27	20.84	-1.56	-0.87
6	20.84	26.05	-5.21	20.84	23.44	-2.60	-2.60
7	21.88	28.48	-6.60	21.88	24.31	-2.43	-4.17
8	19.97	27.78	-7.81	19.97	21.71	-1.74	-6.08
9	19.27	23.01	-3.73	19.27	22.57	-3.30	-0.43
10	20.14	21.71	-1.56	20.66	23.44	-2.78	1.22
11	19.10	16.50	2.60	19.19	21.71	-2.52	5.12
12	19.10	14.76	4.34	19.10	20.84	-1.74	6.08

Tapping points	Intial reading (mm of H20)	α= 220^0 (mm of H20) Convex surface		Intial reading (mm of H20)	α= 220^0 (mm of H20) Concave surface		Pressure dif. DP (mm of H20)
1	20.84	23.44	-2.60	20.66	22.57	-1.91	-0.69
2	20.66	23.01	-2.34	20.23	22.23	-2.00	-0.35
3	19.97	22.14	-2.17	19.97	22.57	-2.60	0.43
4	19.97	22.57	-2.60	19.80	21.71	-1.91	-0.69
5	19.27	23.44	-4.17	19.27	21.27	-2.00	-2.17
6	20.84	27.78	-6.95	20.84	23.44	-2.60	-4.34
7	21.88	29.95	-8.07	21.88	24.31	-2.43	-5.64
8	19.97	29.95	-9.98	19.97	22.57	-2.60	-7.38
9	19.27	26.05	-6.77	19.27	22.57	-3.30	-3.47
10	20.14	23.44	-3.30	20.66	22.57	-1.91	-1.39
11	19.10	17.36	1.74	19.19	20.84	-1.65	3.39
12	19.10	13.89	5.21	19.10	21.71	-2.60	7.81

Tapping points	Intial reading (mm of H20)	α= 230^0 (mm of H20) Convex surface		Intial reading (mm of H20)	α= 230^0 (mm of H20) Concave surface		Pressure dif. DP (mm of H20)
1	20.84	23.88	-3.04	20.66	22.57	-1.91	-1.13
2	20.66	23.44	-2.78	20.23	22.57	-2.34	-0.43
3	19.97	22.57	-2.60	19.97	22.14	-2.17	-0.43
4	19.97	23.44	-3.47	19.80	21.71	-1.91	-1.56
5	19.27	25.18	-5.90	19.27	20.84	-1.56	-4.34
6	20.84	29.95	-9.12	20.84	23.44	-2.60	-6.51
7	21.88	32.12	-10.25	21.88	24.31	-2.43	-7.81
8	19.97	30.82	-10.85	19.97	22.57	-2.60	-8.25
9	19.27	26.92	-7.64	19.27	22.57	-3.30	-4.34
10	20.14	23.44	-3.30	20.66	22.57	-1.91	-1.39
11	19.10	15.63	3.47	19.19	20.84	-1.65	5.12
12	19.10	11.72	7.38	19.10	21.27	-2.17	9.55

Tapping points	Intial reading (mm of H20)	α= 240^0 (mm of H20) Convex surface		Intial reading (mm of H20)	α= 240^0 (mm of H20) Concave surface		Pressure dif. DP (mm of H20)
1	20.84	24.31	-3.47	20.66	22.57	-1.91	-1.56
2	20.66	23.88	-3.21	20.23	22.57	-2.34	-0.87
3	19.97	24.66	-4.69	19.97	22.14	-2.17	-2.52
4	19.97	26.05	-6.08	19.80	21.53	-1.74	-4.34
5	19.27	26.05	-6.77	19.27	20.84	-1.56	-5.21
6	20.84	28.65	-7.81	20.84	23.44	-2.60	-5.21
7	21.88	32.12	-10.25	21.88	24.31	-2.43	-7.81
8	19.97	30.39	-10.42	19.97	21.71	-1.74	-8.68
9	19.27	26.92	-7.64	19.27	21.71	-2.43	-5.21
10	20.14	23.44	-3.30	20.66	22.57	-1.91	-1.39
11	19.10	14.76	4.34	19.19	20.66	-1.48	5.82
12	19.10	11.46	7.64	19.10	21.27	-2.17	9.81

Tapping points	Intial reading (mm of H20)	α= 250^0 (mm of H20) Convex surface		Intial reading (mm of H20)	α= 250^0 (mm of H20) Concave surface		Pressure dif. DP (mm of H20)
1	20.84	24.74	-3.91	20.66	22.57	-1.91	-2.00
2	20.66	25.18	-4.51	20.23	22.57	-2.34	-2.17
3	19.97	26.92	-6.95	19.97	22.57	-2.60	-4.34
4	19.97	27.78	-7.81	19.80	22.23	-2.43	-5.38
5	19.27	24.74	-5.47	19.27	21.71	-2.43	-3.04
6	20.84	25.61	-4.78	20.84	24.31	-3.47	-1.30
7	21.88	27.78	-5.90	21.88	24.74	-2.87	-3.04
8	19.97	27.35	-7.38	19.97	23.01	-3.04	-4.34
9	19.27	26.05	-6.77	19.27	23.01	-3.73	-3.04
10	20.14	23.44	-3.30	20.66	22.57	-1.91	-1.39
11	19.10	14.33	4.78	19.19	20.84	-1.65	6.42
12	19.10	11.72	7.38	19.10	21.27	-2.17	9.55

Tapping points	Intial reading (mm of H20)	α= 260^0 (mm of H20) Convex surface		Intial reading (mm of H20)	α= 260^0 (mm of H20) Concave surface		Pressure dif. DP (mm of H20)
1	20.84	25.18	-4.34	20.66	23.01	-2.34	-2.00
2	20.66	26.48	-5.82	20.23	22.57	-2.34	-3.47
3	19.97	28.22	-8.25	19.97	22.57	-2.60	-5.64
4	19.97	28.65	-8.68	19.80	22.14	-2.34	-6.34
5	19.27	21.71	-2.43	19.27	21.71	-2.43	0.00
6	20.84	21.27	-0.43	20.84	24.31	-3.47	3.04
7	21.88	20.84	1.04	21.88	24.74	-2.87	3.91
8	19.97	21.71	-1.74	19.97	23.44	-3.47	1.74
9	19.27	20.84	-1.56	19.27	23.01	-3.73	2.17
10	20.14	21.71	-1.56	20.66	22.57	-1.91	0.35
11	19.10	16.50	2.60	19.19	20.84	-1.65	4.25
12	19.10	12.16	6.95	19.10	22.14	-3.04	9.98

Tapping points	Intial reading (mm of H20)	α= 270^0 (mm of H20) Convex surface		Intial reading (mm of H20)	α= 270^0 (mm of H20) Concave surface		Pressure dif. DP (mm of H20)
1	20.84	25.61	-4.78	20.66	23.44	-2.78	-2.00
2	20.66	26.92	-6.25	20.23	23.01	-2.78	-3.47
3	19.97	29.09	-9.12	19.97	22.57	-2.60	-6.51
4	19.97	28.65	-8.68	19.80	22.14	-2.34	-6.34
5	19.27	26.05	-6.77	19.27	21.71	-2.43	-4.34
6	20.84	13.89	6.95	20.84	24.31	-3.47	10.42
7	21.88	17.36	4.51	21.88	25.18	-3.30	7.81
8	19.97	18.23	1.74	19.97	23.44	-3.47	5.21
9	19.27	17.36	1.91	19.27	23.44	-4.17	6.08
10	20.14	18.67	1.48	20.66	23.01	-2.34	3.82
11	19.10	17.36	1.74	19.19	20.84	-1.65	3.39
12	19.10	18.23	0.87	19.10	21.71	-2.60	3.47

Tapping points	Intial reading (mm of H20)	α= 280^0 (mm of H20) Convex surface		Intial reading (mm of H20)	α= 280^0 (mm of H20) Concave surface		Pressure dif. DP (mm of H20)
1	20.84	26.92	-6.08	20.66	24.14	-3.47	-2.60
2	20.66	26.48	-5.82	20.23	23.44	-3.21	-2.60
3	19.97	28.65	-8.68	19.97	23.10	-3.13	-5.56
4	19.97	28.22	-8.25	19.80	22.57	-2.78	-5.47
5	19.27	16.06	3.21	19.27	22.14	-2.87	6.08
6	20.84	13.02	7.81	20.84	24.31	-3.47	11.29
7	21.88	12.16	9.72	21.88	25.18	-3.30	13.02
8	19.97	13.46	6.51	19.97	24.31	-4.34	10.85
9	19.27	16.06	3.21	19.27	23.44	-4.17	7.38
10	20.14	18.23	1.91	20.66	22.57	-1.91	3.82
11	19.10	18.23	0.87	19.19	21.71	-2.52	3.39
12	19.10	19.97	-0.87	19.10	22.57	-3.47	2.60

Tapping points	Intial reading (mm of H20)	α= 290^0 (mm of H20) Convex surface		Intial reading (mm of H20)	α= 290^0 (mm of H20) Concave surface		Pressure dif. DP (mm of H20)
1	20.84	27.35	-6.51	20.66	24.14	-3.47	-3.04
2	20.66	26.92	-6.25	20.23	23.44	-3.21	-3.04
3	19.97	26.05	-6.08	19.97	23.44	-3.47	-2.60
4	19.97	22.57	-2.60	19.80	23.44	-3.65	1.04
5	19.27	21.71	-2.43	19.27	23.44	-4.17	1.74
6	20.84	11.72	9.12	20.84	24.83	-3.99	13.11
7	21.88	12.16	9.72	21.88	25.18	-3.30	13.02
8	19.97	12.16	7.81	19.97	24.31	-4.34	12.16
9	19.27	13.02	6.25	19.27	24.31	-5.04	11.29
10	20.14	15.98	4.17	20.66	23.44	-2.78	6.95
11	19.10	17.71	1.39	19.19	23.01	-3.82	5.21
12	19.10	20.84	-1.74	19.10	23.01	-3.91	2.17

Tapping points	Intial reading (mm of H20)	α= 300^0 (mm of H20) Convex surface		Intial reading (mm of H20)	α= 300^0 (mm of H20) Concave surface		Pressure dif. DP (mm of H20)
1	20.84	26.48	-5.64	20.66	25.18	-4.51	-1.13
2	20.66	25.61	-4.95	20.23	24.31	-4.08	-0.87
3	19.97	23.88	-3.91	19.97	24.31	-4.34	0.43
4	19.97	19.10	0.87	19.80	24.31	-4.51	5.38
5	19.27	11.81	7.47	19.27	23.88	-4.60	12.07
6	20.84	11.29	9.55	20.84	26.05	-5.21	14.76
7	21.88	12.16	9.72	21.88	26.05	-4.17	13.89
8	19.97	11.72	8.25	19.97	25.61	-5.64	13.89
9	19.27	11.72	7.55	19.27	24.14	-4.86	12.42
10	20.14	14.76	5.38	20.66	23.44	-2.78	8.16
11	19.10	17.36	1.74	19.19	22.57	-3.39	5.12
12	19.10	21.01	-1.91	19.10	24.66	-5.56	3.65

Tapping points	Intial reading (mm of H20)	α= 310^0 (mm of H20) Convex surface		Intial reading (mm of H20)	α= 310^0 (mm of H20) Concave surface		Pressure dif. DP (mm of H20)
1	20.84	24.48	-3.65	20.66	26.05	-5.38	1.74
2	20.66	21.71	-1.04	20.23	24.48	-4.25	3.21
3	19.97	18.23	1.74	19.97	25.61	-5.64	7.38
4	19.97	13.89	6.08	19.80	25.61	-5.82	11.89
5	19.27	10.42	8.86	19.27	25.18	-5.90	14.76
6	20.84	11.29	9.55	20.84	26.92	-6.08	15.63
7	21.88	13.46	8.42	21.88	27.35	-5.47	13.89
8	19.97	12.59	7.38	19.97	26.57	-6.60	13.98
9	19.27	12.59	6.69	19.27	24.31	-5.04	11.72
10	20.14	14.76	5.38	20.66	23.44	-2.78	8.16
11	19.10	18.23	0.87	19.19	23.44	-4.25	5.12
12	19.10	21.71	-2.60	19.10	26.05	-6.95	4.34

Tapping points	Intial reading (mm of H20)	α= 320^0 (mm of H20) Convex surface		Intial reading (mm of H20)	α= 320^0 (mm of H20) Concave surface		Pressure dif. DP (mm of H20)
1	20.84	20.84	0.00	20.66	26.48	-5.82	5.82
2	20.66	16.50	4.17	20.23	25.87	-5.64	9.81
3	19.97	13.02	6.95	19.97	26.05	-6.08	13.02
4	19.97	10.94	9.03	19.80	25.61	-5.82	14.85
5	19.27	11.29	7.99	19.27	25.18	-5.90	13.89
6	20.84	13.89	6.95	20.84	26.92	-6.08	13.02
7	21.88	16.06	5.82	21.88	27.35	-5.47	11.29
8	19.97	14.76	5.21	19.97	26.92	-6.95	12.16
9	19.27	14.76	4.51	19.27	24.31	-5.04	9.55
10	20.14	16.93	3.21	20.66	23.88	-3.21	6.42
11	19.10	18.67	0.43	19.19	23.44	-4.25	4.69
12	19.10	21.71	-2.60	19.10	26.05	-6.95	4.34

Tapping points	Intial reading (mm of H20)	α= 330^0 (mm of H20) Convex surface		Intial reading (mm of H20)	α= 330^0 (mm of H20) Concave surface		Pressure dif. DP (mm of H20)
1	20.84	17.36	3.47	20.66	25.18	-4.51	7.99
2	20.66	13.02	7.64	20.23	25.61	-5.38	13.02
3	19.97	10.42	9.55	19.97	25.18	-5.21	14.76
4	19.97	11.29	8.68	19.80	25.18	-5.38	14.07
5	19.27	13.89	5.38	19.27	24.83	-5.56	10.94
6	20.84	16.93	3.91	20.84	26.05	-5.21	9.12
7	21.88	19.10	2.78	21.88	26.92	-5.04	7.81
8	19.97	16.50	3.47	19.97	26.05	-6.08	9.55
9	19.27	15.63	3.65	19.27	24.31	-5.04	8.68
10	20.14	17.80	2.34	20.66	23.88	-3.21	5.56
11	19.10	18.67	0.43	19.19	23.44	-4.25	4.69
12	19.10	20.40	-1.30	19.10	25.18	-6.08	4.78

Tapping points	Intial reading (mm of H20)	α= 340^0 (mm of H20) Convex surface		Intial reading (mm of H20)	α= 340^0 (mm of H20) Concave surface		Pressure dif. DP (mm of H20)
1	20.84	14.59	6.25	20.66	24.74	-4.08	10.33
2	20.66	10.59	10.07	20.23	25.18	-4.95	15.02
3	19.97	10.59	9.38	19.97	24.74	-4.78	14.15
4	19.97	14.76	5.21	19.80	24.74	-4.95	10.16
5	19.27	17.36	1.91	19.27	24.31	-5.04	6.95
6	20.84	19.97	0.87	20.84	26.05	-5.21	6.08
7	21.88	20.40	1.48	21.88	26.48	-4.60	6.08
8	19.97	17.36	2.60	19.97	25.18	-5.21	7.81
9	19.27	16.06	3.21	19.27	24.31	-5.04	8.25
10	20.14	17.36	2.78	20.66	23.88	-3.21	5.99
11	19.10	17.80	1.30	19.19	23.44	-4.25	5.56
12	19.10	17.36	1.74	19.10	24.74	-5.64	7.38

Tapping points	Intial reading (mm of H20)	α= 350^0 (mm of H20) Convex surface		Intial reading (mm of H20)	α= 350^0 (mm of H20) Concave surface		Pressure dif. DP (mm of H20)
1	20.84	12.59	8.25	20.66	23.27	-2.60	10.85
2	20.66	10.42	10.25	20.23	24.31	-4.08	14.33
3	19.97	13.46	6.51	19.97	22.57	-2.60	9.12
4	19.97	18.67	1.30	19.80	22.57	-2.78	4.08
5	19.27	19.10	0.17	19.27	21.71	-2.43	2.60
6	20.84	20.40	0.43	20.84	23.88	-3.04	3.47
7	21.88	20.84	1.04	21.88	24.74	-2.87	3.91
8	19.97	17.36	2.60	19.97	22.57	-2.60	5.21
9	19.27	17.36	1.91	19.27	23.44	-4.17	6.08
10	20.14	16.50	3.65	20.66	21.71	-1.04	4.69
11	19.10	16.50	2.60	19.19	17.80	1.39	1.22
12	19.10	16.06	3.04	19.10	17.80	1.30	1.74